Ministero dell'Universitá e
della Ricerca

Universitá degli Studi
di Palermo

Dipartimento di Fisica

Dottorato di Ricerca in Fisica
XXIII Ciclo

Tracking hemoglobin structural dynamics: from dilute solutions to intact cells

PhD Thesis

(S.S.D. Fis/07)

Palermo, Febbraio 2012

Dr. Alessandro Spilotros

Tutor Prof. Antonio Cupane

Coordinatore Prof. Antonio Cupane

Contents

Introduction

Schröedinger in his "What is life?" (1944) called bio-molecules "aperiodic crystals". Structural biology was born in 1958 with John Kendrew's atomic structure of myoglobin and in the following decade the field grew rapidly. Kendrew's structure of myoglobin [1] revealed the folding of protein chains for the first time, as well as showing how protein chains interact with prosthetic groups and with ligands. Max Perutz's structure of hemoglobin [2] was the first solved structure of a multi-subunit protein and showed how four similar chains can associate and regulate the binding of ligands through small changes in structure. By the early 1970's, there were a dozen atomic structures of proteins: the X-ray structures obtained on protein crystals seemed to confirm the Schröedinger's view in which each atom is in its proper place as a part of a complex but well defined three-dimensional structure without a periodic repetition [3, 4]. The knowledge of the three-dimensional structure is the starting point to understand how the proteins work.
Nevertheless the information emerging from crystal structures is not sufficient to describe completely the mechanism underlying protein function. In fact, in physiologic conditions, proteins exhibit a complex energy landscape where multiple minima can be explored. It was transient absorption spectroscopy on geminate recombination in myoglobin that led Hans Frauenfelder to his picture of protein's hierarchical energy landscape [6]. Even before that, in 1973, J. Lakowicz and G. Weberused studying the quenching of tryptophan fluorescence by oxygen diffusing to protein regions not accessible for the solvent concluded that "proteins, in general, undergo rapid structural fluctuations on the nanosecond time scale" [7].
As a result of such complex energy landscape, proteins carry out their biological functions by altering their structures with motions ranging from subangstroms to tens of angstroms and covering a broad range of time scales (from sub-picoseconds to seconds).
The crucial role of protein motion for proper functioning can be illustrated on some rather general examples:
- Some proteins play the role of "gates" in trans-membrane channels, i.e.

they open and close selectively the channel to permit or deny access to the cell to a variety of molecules [8].
- In the case of electron/proton transferring proteins, the observed transfer rate is related to protein dynamics rapidly sampling the conformational space: the transfer rate is often determined by the configurations with optimal geometries [9, 10, 11].
- In enzymatic allosteric regulation the binding of a substrate on one place triggers a reaction on a different site within the protein. This phenomenon is related to the presence of two different minima in the free energy surface, corresponding to two different conformational substates. The inactive conformation is preferred by the free enzyme while the minimum of active conformation is preferred by the enzyme-substrate complex [11].
A paradigmatic example of the allosteric control of enzyme function is given by the "honorary enzyme" hemoglobin (Hb) [12]. The main physiological role of Hb in human body is to act as oxygen carrier from the lungs to the tissues; in order to optimize its function, the four active sites of Hb react with oxygen in a cooperative way [13] and the protein matrix mediates the interaction between them. The seminal crystallographic work of Perutz and the conceptual framework introduced by the Monod-Wyman-Changeux model [14] unraveled the "secret" of Hb cooperativity: this molecule is able to adopt at least two different quaternary structures in solution: a "relaxed" (R) structure stabilized by the presence of ligands, and a "tense" (T) structure that is stable when the protein is unligated [15, 16]. The ligated-to-unligated transition in Hb involves both conformational changes within the subunits (tertiary structure transition) and changes in the relative disposition of the subunits (quaternary structure transition). As a result, the ligand affinity of the R quaternary conformation is greatly increased with respect to that of the T quaternary conformation. The R-T transition is often used as a paradigm of structure-mediated cooperativity in molecular biology and because of its general relevance it was chosen as the main subject of this work of thesis.
For a deep understanding of the quaternary transition mechanism in Hb, a complete description of equilibrium conformational substates and of the kinetic pathway connecting them is needed. In the first chapter of this thesis a brief introduction to the quaternary transition in Hb is presented together to a brief resume of the enormous literature regarding this subject. The second chapter is focused on the experimental approach used to investigate quaternary transition in Hb. In 2008 a new experimental technique, Time resolved wide angle X-ray scattering (TR-WAXS), has become available [17]: the TR-WAXS technique allows to collect X-ray scattering patterns from macromolecules in solution as a function of time. Using the pump and probe

approach, the scattering patterns can be collected at different time delays in respect with an excitation signal used as a trigger for protein conformational changes. The pump and probe scheme ensures the high time resolution needed to track the kinetics of protein structural changes. Moreover, sampling the wide angle range of the scattering pattern (corresponding to a scattering vector between 0.1-2 $\mathring{A}^{-1}$) it is possible to investigate tertiary and secondary structure of proteins as well as the relative position of subunits [18, 19]. To obtain a good signal to noise ratio this technique requires the use of synchrotron radiation. Being directly sensitive to the position of all atoms in the protein as a function of time, TR-WAXS is complementary to the spectroscopic techniques that in contrast are sensitive to the properties of specific chromophores.
TR-WAXS allows the study of large protein structural changes directly in solution. Because large amplitude motions are unaccessible in crystals TR-WAXS is complementary to time resolved crystallography [20, 21, 22]. Moreover TR-WAXS ensures a time resolution higher than other structural technique such as NMR (limited to ms) and without the need of properly labeled samples [23]. This technique has been already applied successfully to probe the laser induced conformational changes in carboxy-myoglobin after photolysis of the ligand, to the study of the folding of cytochrome c and light induced conformational changes such as the simple light-driven proton pump bacteriorhodopsin as well as the superoxide scavenger superoxide reductase [24]. TR-WAXS was applied also to the study of quaternary transition in human Hb [17, 25] tracking quaternary conformational changes induced by laser photolysis on carboxy-hemoglobin (HbCO) (figure 1). The most remarkable result of these experiments is that a global structural relaxation compatible with the relative rotation of $\alpha\beta$ Hb dimers occurs at $\sim$2 μs, i.e. ten times faster than expected from spectroscopic measurements [26, 27, 28, 29, 30] (the reader can find further details in chapter 1).

These results have contributed to the scientific debate about quaternary transition in Hb giving new insights about the structural events leading the protein from a quaternary state to the other: the main quaternary rearrangement (mainly the dimer rotation) takes place with a time constant of 2 μs while the relaxation revealed at 20 μs by time resolved spectroscopy could be related to a tertiary local structural rearrangement.
The TR-WAXS experiments presented in the chapter 3 of this thesis are the extension of previous ones on native hemoglobin: the time resolution was improved (up to 3 ns) to investigate early events after photolysis and the effect of an heterogeneous distribution of initial ligation states was checked: in our conditions the R_1 and R_2 (where the subscript refers to the number of bound ligands) forms of Hb are significantly populated after photolysis.

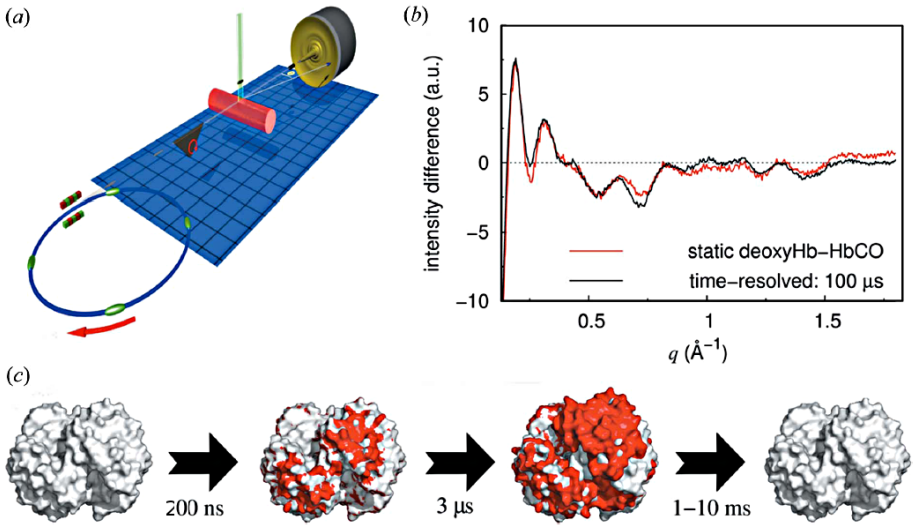

Figure 1: Time-resolved wide-angle X-ray scattering of carboxy-hemoglobin. a) Sketch of the experimental set-up at the dedicated time-resolved beamline at the European Synchrotron Radiation Facility ID09b. Polychromatic X-ray pulses are generated in an undulator and a rotating chopper (black triangle) is used to isolate a chosen pulse train. Protein samples are sealed within a glass capillary (red) and are excited by laser pulses (green) incident perpendicular to the X-ray beam. X-ray scattering images are collected on a charge-couple device (CCD) detector. b) The azimuthal integration leads to one-dimensional scattering patterns I(q) and the subtraction of "laser off" images from "laser on" images gives difference scattering curves, which are the fingerprint of the structural rearrangements in the protein. Difference scattering recorded from hemoglobin in complex with carbon monoxide 100 μs after photoexcitation (red) are compared with "static" differences between haemoglobin with carbon monoxide bound and deoxy-hemoglobin (black). c) Representation of the expected structural changes in hemoglobin. Regions of the proteins that are involved in the changes are coloured red. The figure is taken from Nature Methods (Cammarata et al., 2008) [17]

Moreover, the technique was extended to a functional relevant class of Hb mutants called Hb$\alpha\beta$YQ, HbαYQ, HbβYQ, to test the effect of point mutations on the quaternary transition kinetics.
Finally in chapter 4 a first application of the TR-WAXS to a cellular system is presented.
Protein dynamics and stability are predominantly investigated in vitro and usually the results are extrapolated to explain function in the living cells.
In-vivo, the energy landscape is modulated by a myriad of interactions. The dynamics and stability of a protein crowded in high concentration conditions (up to 400 mg of macromolecules per milliliter) can differ substantially from the dynamics of the isolated protein [31, 32]. Furthermore, crowding modifies the properties of cellular water which in turn is coupled to the dynamics of biomolecules [33]. Membranes and other large-scale structures in the cell can also crowd or confine biomolecules, as can the interaction with cellular transport machinery or chaperones [34, 35]. For all these reasons, investigating proteins "at work" directly inside the cell is a major goal in molecular biology and to this purpose both high temporal and spatial resolution are required. A successful approach to the study of protein dynamics in the heterogeneous and crowded cell system requires a technique able to isolate the protein structural signal and to avoid cell disruption during the measurements. Protein structural changes in cell have so far been characterized with different methods, yielding different types of information. Coherent anti-Stokes Raman scattering microscopy have been used to detect small-molecule distributions inside living cells [36]. FlAsH dye-labeling can reveal slow unfolding of proteins in bacterial cells induced by urea[37]. Fluorescence resonance energy transfer (FRET) coupled with fluorescence microscopy can be used not only to localize proteins but also to monitor protein-protein interactions[38]. Protein structure in cell has been recently investigated by nuclear magnetic resonance (NMR) [41, 42]. However NMR works best for small and properly labeled proteins, and its time resolution is inherently limited to milliseconds. The spectroscopic techniques mainly give signals that are only indirectly related to three-dimensional structures of the proteins. In-cell TR-WAXS, could provide both high spatial and time resolution as well as a direct sensitivity to protein structure completing the ensemble of available experimental techniques to study in-vivo protein dynamics. The extension of the TR-WAXS experiments on a cell system is reported, as anticipated above, in chapter 4: structural changes at tertiary and quaternary level after photolysis of carboxy-hemoglobin were tracked in intact human erythrocytes with nanosecond time resolution. This study is the follow-through of the in-vitro time-resolved experiments reported in chapter 3 and, apart from giving interesting insights about hemoglobin dynamics in vivo, could be more gen-

erally a first promising step towards the in-cell studies on other interesting protein systems.

Chapter 1

Quaternary transition of Hemoglobin

This chapter gives a brief description of the hemoglobin structure and function. It is mainly focused on the quaternary transition, i.e. the change in the relative position of subunits that Hb undergoes in order to regulate the affinity for ligands. The chapter is meant as a short introduction to the topic and the interested reader can refer to the bibliography for a complete presentation of the subject [13, 43].

Hb is a tetramer composed of two different chains designated α and β, organized in two dimers $\alpha_1\beta_1$ and $\alpha_2\beta_2$. The four subunits of hemoglobin sit roughly at the corners of a tetrahedron facing each other across the center of the molecule (figure 1.1). Each of the subunits contains a heme prosthetic group. Each individual heme molecule contains one Fe^{2+} atom able to bind the oxygen molecule and other ligands such as carbon monoxide and nitrogen monoxide. The active site of the protein, the heme group, is bound to the rest of the protein matrix by the His F8 in proximal position. Without oxygen bound, Fe is out of heme plane and when oxygen binds the Fe is pushed into the heme plane. Fe pulls its His F8 ligand along with it and then the F helix moves when oxygen binds (figure 1.2). Ligands such as O_2 are directly bound to Fe^{2+} but a number of different interactions (hydrogen bonds, electrostatic etc.) with residues in the distal side of the heme (the "heme pocket") are possible. In the heme pocket, a number of residues have a role in ligand binding modulation.

The main physiological role of Hb is to act as oxygen carrier from the lungs to the tissues and, in order to perform its task efficiently, Hb reacts with oxygen in a cooperative way [13]. In general the word cooperativity is used when a substrate binds to one enzymatic subunit and the rest of the subunits are stimulated and become active. In the case of Hb, one oxygen molecule

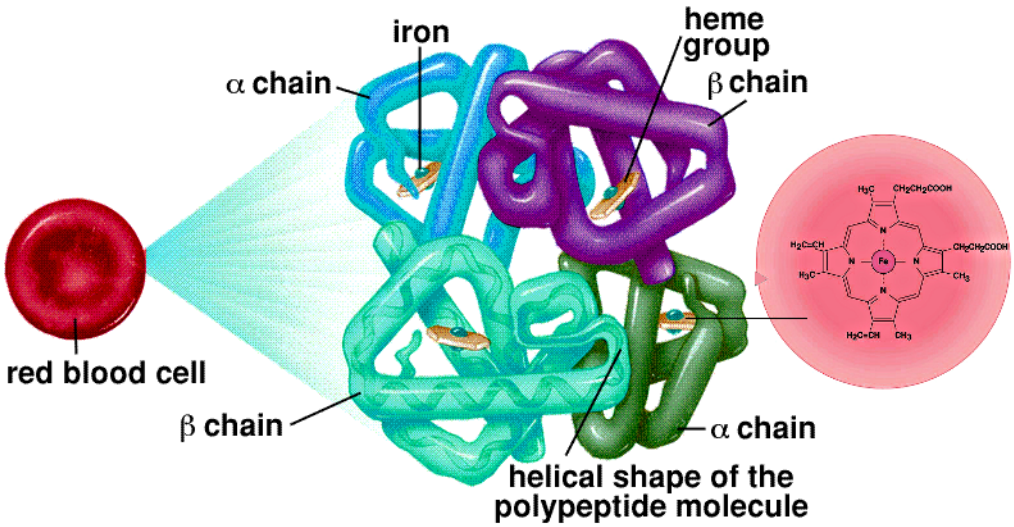

Figure 1.1: In human body hemoglobin is carried in red blood cells in high concentration (up to 5 mM in tetramer). The schematic structure of Hb is reported in figure where secondary α-helix structure is represented as coloured tubes. The four subunits are represented with different colours and each one hosts the heme group. The structure of heme group is reported on the left.

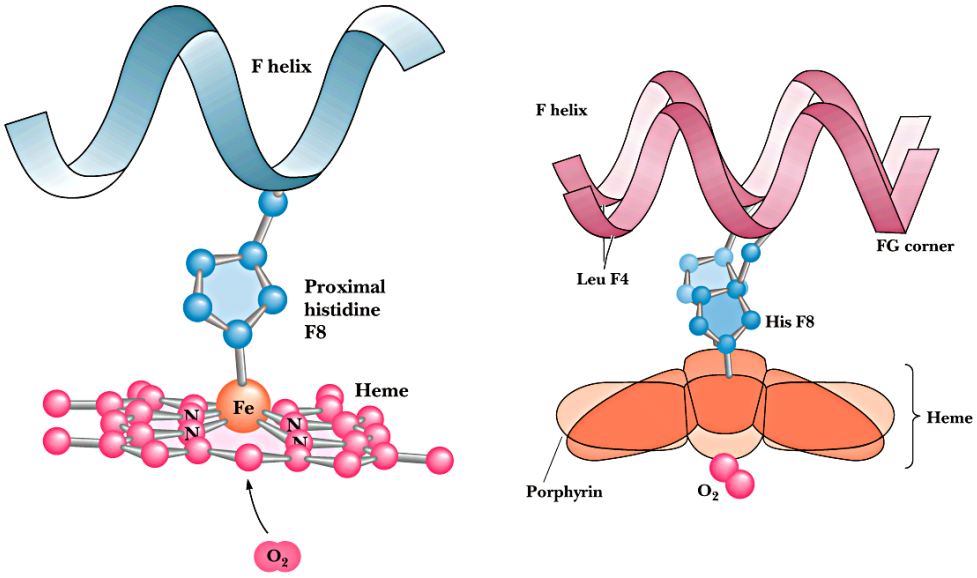

Figure 1.2: Left: schematic representation of heme group and residue His F8 that anchors the heme to the rest of the protein. Right: structural change occurring after oxygen binding. The figure is taken from Garret & Grisham 2008 [44]

can bind to the ferrous iron of a heme molecule in each of the four subunits. Deoxy-hemoglobin has a relatively low affinity for oxygen, but when one molecule binds to a single heme, the oxygen affinity increases, allowing the second molecule to bind more easily, and the third and fourth even more easily. This behavior leads the affinity curve of hemoglobin to be sigmoidal, rather than hyperbolic as with the monomeric myoglobin (figure 1.3). Because of what is happening to one of the active sites influences the affinity of the others, Hb is often presented as a paradigm of allostery in biology.

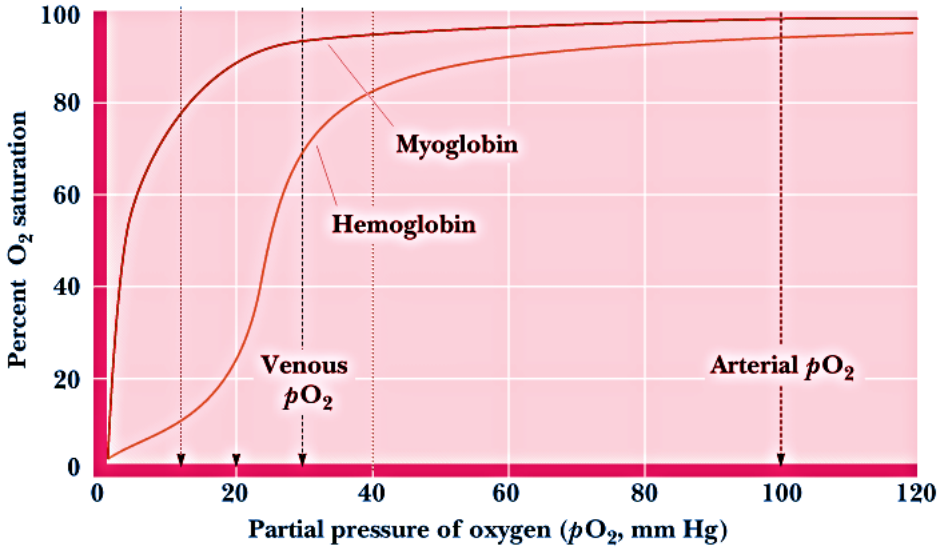

Figure 1.3: The sigmoidal shape of hemoglobin oxygen-dissociation curve results from cooperative binding of oxygen to hemoglobin. For comparison myoglobin oxygen-dissociation curve is reported showing how in contrast hemoglobin is able to switch from a low oxygen affinity at the tissues level to an high affinity at lungs oxygen pressure. The figure is taken from Garret & Gisham 2008 [44].

The hypothesis that a conformational change in the protein mediates such allosteric interactions between active sites was proposed in 1965. The mechanism that controls this conformational change remains a central question of biophysics: understanding the Hb allostery can give a model to understand the function regulation of other allosteric proteins. For this reasons the subject has enormous importance for the design of drugs.
It was in 1965 that Monod Wyman and Changeux proposed a model (denoted MWC) for cooperative ligand binding in native enzymes (extended in 1966 by Rubin and Changeux) postulating a small number of discrete

conformational states independent of ligand occupancy [14, 45]. The Monod-Wyman-Changeux model provided a simple explanation of cooperative ligand binding and its regulation. Following this model, regulatory proteins have a quaternary structure with identical subunits symmetrically organized into oligomers; oligomers undergo reversible transitions between a small number of discrete conformations. The conformations referred by the model have distinct quaternary organization preserving the symmetry and are accessible in the absence of ligand. The ligands stabilize the state to which they preferentially bind and then trigger the conformational change. According to the Monod-Wyman-Changeux model, two conformational states are in equilibrium in absence of ligand T_0 and R_0 (where the subscript stands for the number of ligands bound): T_0 is favored in the absence of ligand and then the equilibrium constant $L_0 = [T0]/[R0]$ is > 1. Since the R state has a higher affinity for ligands, as ligand is bound, the population of protein molecules in the R state grows up.
The binding of a ligand modify the energy landscape of the species involved in allosteric transitions in the sense shown in figure 1.4.
For hemoglobin a linear free energy relation between equilibrium difference energy ΔG^0 and activation barriers ΔG^* has been proposed [46] that implies equally spaced energies for each transition state (TS) characterized by a parameter that fixes the spacing (this concept is explained extensively in the last section of chapter 3 where it is applied to the analysis of the experimental results). The consequence of the constant TS spacing is that for conformational states with increasing numbers of ligands bound the $R \rightarrow T$ rates decrease by a constant factor. Thanks to the seminal work of Perutz a first direct access to the two quaternary structures of Hb was possible. Perutz and his colleagues [2] elucidated the X-ray structures of oxy-hemoglobin and deoxy-hemoglobin and interpreted the data in terms of an equilibrium between a tense structure (T) with low oxygen affinity constrained by salt bridges between the C-termini of the four subunits, and a relaxed structure (R) with high oxygen affinity and lacking the salt bridges.
The crystallographic structures of the R and T conformations give some useful hints on the pathway connecting them:
-Transition from the T structure to the R structure is triggered by the changes occurring at the hemes. In deoxy-hemoglobin the Fe is out-of-plane, five-coordinated, and high-spin while it is in-plane, six-coordinated and low-spin in oxy-hemoglobin. The position of the iron atoms into the porphyrin plane it is required for oxygen binding and it is regulated by the tension exercised by the salt bridges in the T-structure that is in turn transmitted to the heme-linked histidines.
-In deoxy-hemoglobin, the iron atom is about 0.6 angstroms out of the heme

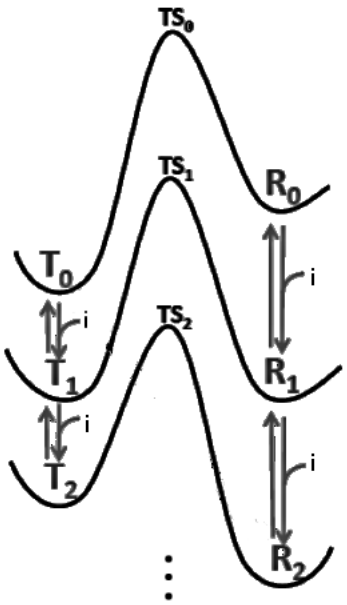

Figure 1.4: T and R states are presented on a vertical free energy scale and include the transition state (TS) kinetic barriers for their interconversion, according to linear free energy relationship [46]. Subscripts correspond to the number of ligand molecules (i) bound. The T-R possible transitions for hemoglobin are of course five ($T_i \rightarrow R_i$ with i=0,..,4) while in the graph just the first three are represented.

plane because of steric repulsion between the proximal histidine and the nitrogen atoms of the porphyrin. The heme group and proximal histidine are in contact with different side chains and so the structures of the F helix, the EF corner, and the FG corner change on oxygenation. These changes are then transmitted to the subunit interfaces leading to the rupture of inter-chain salt bridges. Consequently, the equilibrium between the two quaternary structures is shifted to the R form on oxygenation.

- From the quaternary structure point of view, the R-T transition involves a $\sim$15 degrees rotation of one $\alpha\beta$ dimer with respect to the other in which inter-dimer interfaces are rearranged (whereas intra-dimer interfaces remain largely unchanged). For this reason the interface $\alpha1\beta2$ has been successively addressed by different experimental approaches to study R-T transition. This interface contains residues of helix C and the FG corner of both chains. Different residues establish interactions across the αFG-βC and the αC-βFG contacts (see figure 1.5). The αFG-βC contact, presenting a network of weak bonds, is largely unaltered in the allosteric transition, while the amino acid residues at the αC-βFG contact region of the $\alpha1\beta2$ interface undergo an important reorganization. Baldwin and Chothia in 1979 [48], studying $\alpha1\beta2$ interface, defined the αFG-βC contact region as a "flexible joint" and the αC-βFG as a "switch" to suggest the role they play in quaternary transition.

Detailed kinetic measurements on Hb solutions, mainly using fast spectroscopic techniques such as laser flash photolysis of the CO adduct of Hb (HbCO), placed the rate of the conformational transition in the range of tens of μs and were interpreted in the MWC framework. In a typical flash photolysis experiment, a laser pulse is used to break the bound Fe-CO monitoring a physical property of Hb as a function of time. Once the Fe-CO bond is broken the ligand can re-bind to Fe before having the time to diffuse into the solvent (geminate rebinding)[50] or after diffusing into the solvent (bimolecular rebinding). In standard conditions (room temperature, dilute solutions), the first process takes place in hundreds of nanoseconds and it does not depend on the ligand concentration, while the second has longer time scales depending on the free ligand concentration after photolysis. Sawicki and Gibson, in 1976, using time-resolved optical absorption spectroscopy, studied the Soret region (absorption band characteristic of heme-proteins in blue wavelength region [51] see figure 1.6)of HbCO absorption spectrum as a function of time to probe the conversion from R to T state. The authors detected the formation of a fast product of the photolysis (called Hb*) and interpreted it as a deoxy-hemoglobin in R state. Moreover they probed the relaxation from this Hb* to T state measuring the absorbance value at 425 nm as a function of time (isosbestic point of deoxy-hemoglobin and carboxy-hemoglobin spectra; see figure 1.7). In the 1980's, substantial improvements in the time reso-

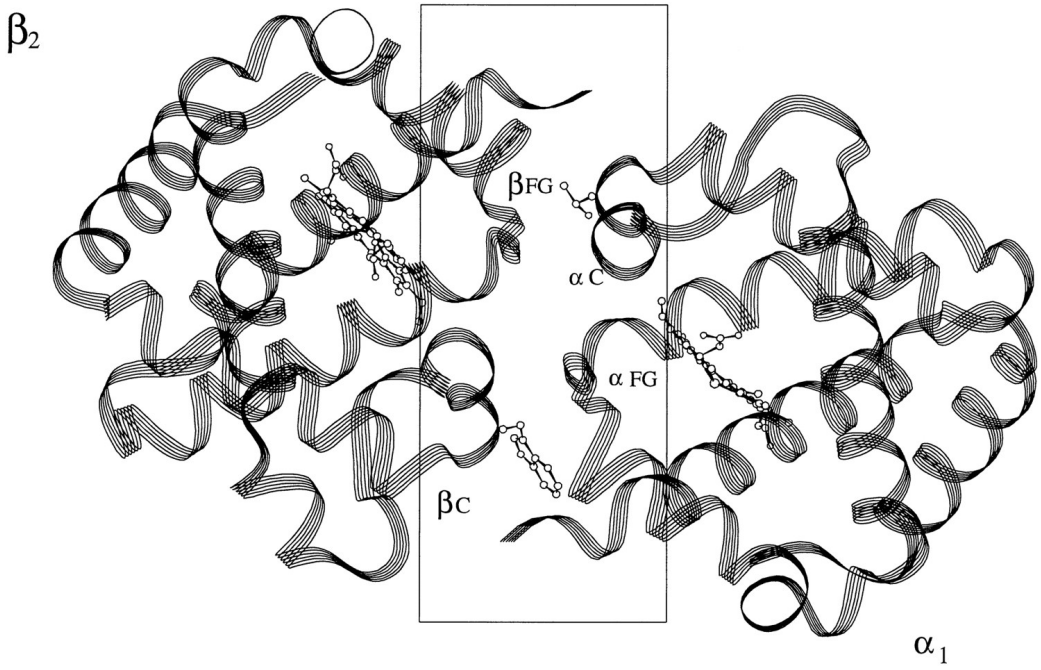

Figure 1.5: Schematic structure of the $\alpha 1 \beta 2$ interface of HbA. The contact regions are indicated by the black square, and the residues represented as balls and sticks are Thr $\alpha 38$ (C3) and Trp $\beta 37$ (C3). The figure is taken from Vallone et al. 1996 [49]

lution and data analysis were made and allowed the identification of much finer details, including geminate recombination and further spectral relaxations [27, 28, 29, 30]. According to these studies protein tertiary relaxation takes place in the sub-microsecond timescale while the quaternary R-T transition occurs at ~ 20 μs after photolysis (at room temperature and neutral pH).

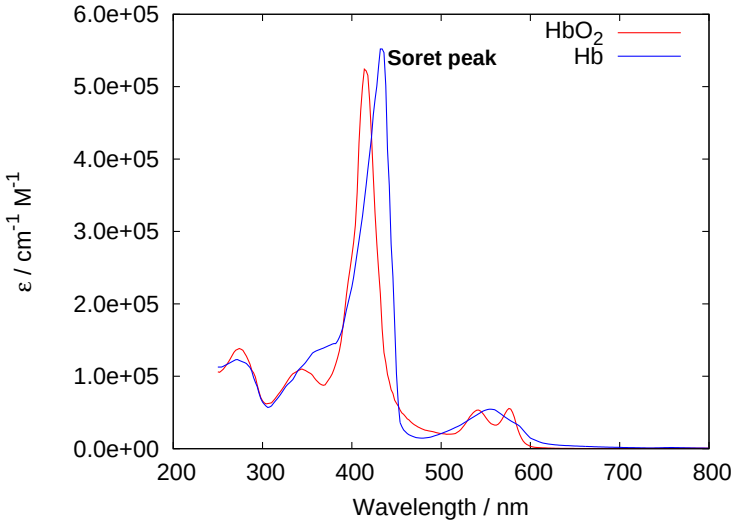

Figure 1.6: Molar extinction coefficient fon Hb and HbO_2: the blue shift of the Soret peak ($\pi \rightarrow \pi*$) is due to the addition of the sixth ligand to Fe (it is observed also in the case of HbCO). These values for the molar extinction coefficient ϵ in [cm^{-1} M^{-1}] were compiled by Scott Prahl (prahl@ece.ogi.edu) using data from W. B. Gratzer, Med. Res. Council Labs, Holly Hill, London and N. Kollias, Wellman Laboratories, Harvard Medical School, Boston.

Time-resolved resonance Raman studies, following the heme resonance Raman spectrum, assigned the observed 20-30 μs relaxation to a tertiary structure relaxation close to the hemes and interpreted it as the signal of completion of the quaternary transition [52, 53]. Other time resolved techniques such as time-resolved UV resonance Raman (TR-UVRR), time-resolved circular dichroism (UV-TRCD), and time-resolved magnetic circular dichroism have been used to complement optical absorption and resonance Raman data [54, 55, 56]. Because the allosteric transition of hemoglobin involves an extensive reorganization of the $\alpha 1 \beta 2$ interface, as emerging from the analysis of crystallographic structures, these techniques where used to probe the properties of this surface as a function of time. In particular, the UV-TRCD indicates that the $\alpha 1 \beta 2$ interface shifts from an R toward a T-like interface

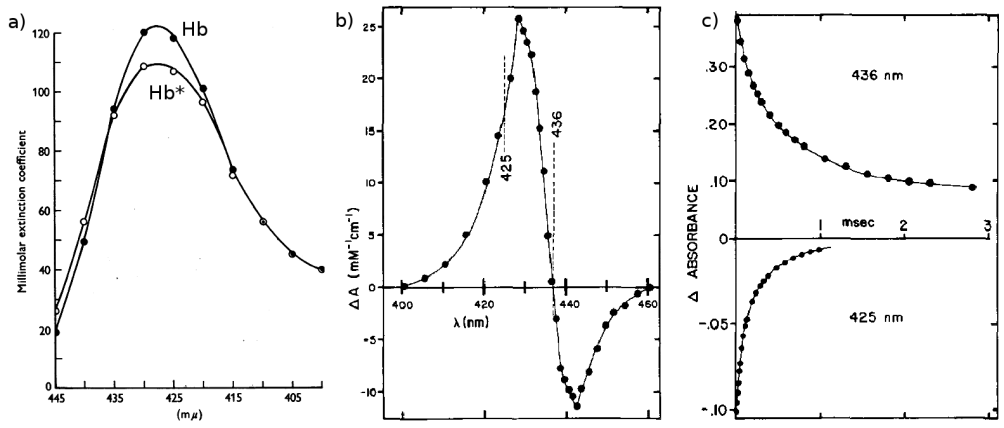

Figure 1.7: Panel a): Absorption spectra of normal (black circles) and fast reacting (white circles) hemoglobin. The figure is taken from Q. H. Gibson, 1958 [47]. Panel b)Soret absorbance difference between deoxy-hemoglobin and Hb* (according to C. Sawicki and Q. H. Gibson, 1976 [26] it represents deoxyhemoglobin in R state). Kinetics experiments were performed at the 425 and 436 nm isosbestic points (marked by dashed vertical lines) of deoxy-hemoglobin and carboxy-hemoglobin spectra, and deoxy-hemoglobin and Hb* spectra respectively. The spectrum was obtained by measuring the absorbance difference between fully photolyzed carboxy-hemoglobin and an equal concentration of deoxy-hemoglobin. Experimental conditions were 1-mm cells with 50 μM hemoglobin at 20 ℃in 0.05 M sodium borate buffer (pH 9.2). Panel c) time dependence of 425 nm and 436 nm absorption values after photolysis used by Sawicki and Gibson to monitor the quaternary relaxation from Hb* to deoxy-hemoglobin (425 nm) and CO rebinding (436 nm). In the rebinding of CO a slow and a fast phase can be identified: the authors assigned them to bimolecular rebinding to T and R state. Panels b and c are taken from C. Sawicki and Q. H. Gibson 1976 [26].

within several hundred nanoseconds after photolysis of carboxy-hemoglobin. This modification of the $\alpha 1\beta 2$ interface appears tens of microseconds before the CD signal associated to the deoxy-hemoglobin. TR-UVVR identified the E F helices clamshell rotation in sub-microsecond range [57] as well as breaking-formation of inter-helical hydrogen bonds; moreover a fast relaxation at 2 μs followed by a slower one in 20-50 μs were assigned to the formation of H-bonds at the "flexible joint" region (Trpb37-Aspa94 H-bond) in $\alpha 1\beta 2$ interface and to formation of contacts in the "switch" region (Tyra42-Aspb99 H-bond) respectively. These results suggest that the dimer rotation can be completed at 2 μs, in contrast with the interpretation of time-resolved absorption spectroscopy, time-resolved circular dichroism,and time-resolved magnetic circular dichroism.

How it is clear from this brief reconstruction an unifying picture emerging from these studies was missing. Note that, while the phenomenon under study is a global and concerted motion of thousands of atoms, the experimental approaches used probe a few specific sites. The need for a complementary structural technique, directly sensitive to changes in tertiary and quaternary structures, was evident.

In 2008 Cammarata et al. [17] used TR-WAXS to to accurately probe structural changes of HbCO after photolysis from 200 ns to millisecond time range. This first application of TR-WAXS to human Hb demonstrated that the main quaternary change related to the R-T transition (dimers rotation) takes place in $\sim$2 μs i.e., about 1 order of magnitude faster than estimated with time-resolved optical spectroscopy. In this experiment a laser pulse of 527 nm wavelength was used to photolyze HbCO and trigger the R-T transition, while wide angle X-ray scattering images at fixed time delays from photolysis were collected. The use of X-rays scattering presents different advantages: X-ray scattering is a probe sensitive to the position of all atoms in the molecule and thanks to the pulsed temporal structure of synchrotron radiation used, time resolved experiments with high time resolution (in principle up to 100 ps i.e. the duration of a single X-pulse) are possible (the reader can find further details on the experimental technique in chapter 2). The laser pulse duration of $\sim$200 ns was chosen in order to improve the efficiency of photolysis limiting the effect of geminate rebinding: after photolysis a fraction of about 45% of the photolized CO recombines to the heme before having the time to diffuse into the solvent. This phenomenon takes place in hundreds of ns. Then a laser pulse of $\sim$200 ns duration competes by multiple photolysis with geminate rebinding maximizing the number of Hb undergoing the R-T transition.

In 2010 the authors extended the previous study performing the experiments under conditions as close as possible to those used in most spectroscopic

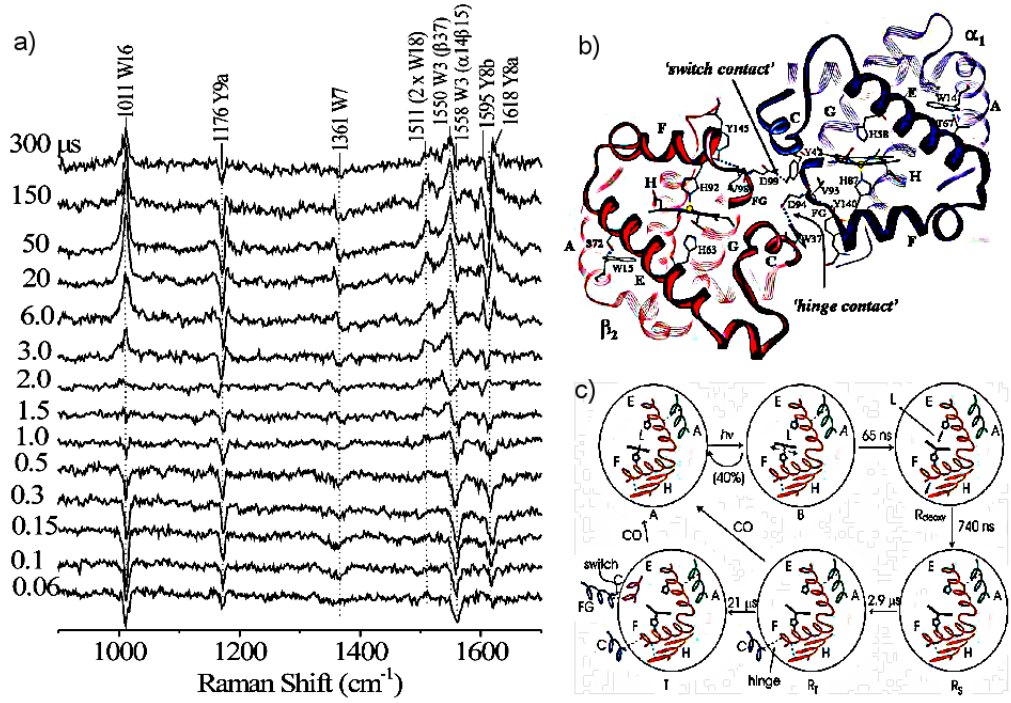

Figure 1.8: Panel a) Time-resolved UVRR difference spectra at the indicated times following the photolysis of HbCO; band positions and assignments are marked at the top. Panel b) The $\alpha 1\beta 2$ subunits in deoxy Hb, showing the "flexible joint" and "switch" quaternary H-bonds, as well as the interhelical tertiary H-bonds monitored by UVRR spectroscopy. Panel c) Model for the allosteric transition. Photolysis of HbCO (A) produces the geminate state, (B), in which forces are stored at the heme. After rotation of the E and F helices takes place, which break inter-helical H-bonds in the Rdeoxy intermediate. These H-bonds are restored in RS intermediate, followed by hinge contact formation, in RT. The switch contact complete the transition to the T state. The figure is taken from Balakrishnan et al. 2004 [57].

studies and examined the dependence of the observed kinetics on experimental parameters such as protein concentration, laser energy density, pH, and buffer composition.
Their results showed that an early transition signal is already fully developed at 200 ns, and corresponds to a tertiary relaxation (clamshell motion as suggested by authors). This signal is followed by a main quaternary relaxation involving the dimers relative rotation and translation occurring in a concerted way at about 2 μs. The 20 μs step observed with time-resolved optical spectroscopy would then correspond to a smaller and localized structural change.

Simulations based on the method of conjugate peak refinement are consistent with such a two-step quaternary transition [58]. In the R to T direction the full quaternary transition presents two steps: an early large quaternary change (characterized by a 3 degrees rotation of each α-subunit relative to the $\beta 1\beta 2$-dimer), with a lower energy barrier (postulated to correspond to the 2 μs step), and a successive smaller quaternary change (6 degrees rotation of the $\alpha 1\beta 1$ and the $\alpha 2\beta 2$ dimers) with a higher energy barrier (postulated to correspond to the 20 μs step). The picture that emerges from the experimental theoretical and simulative work suggests that R-T transition is at least a two-step process and, for its general relevance, deserves other experimental investigations.

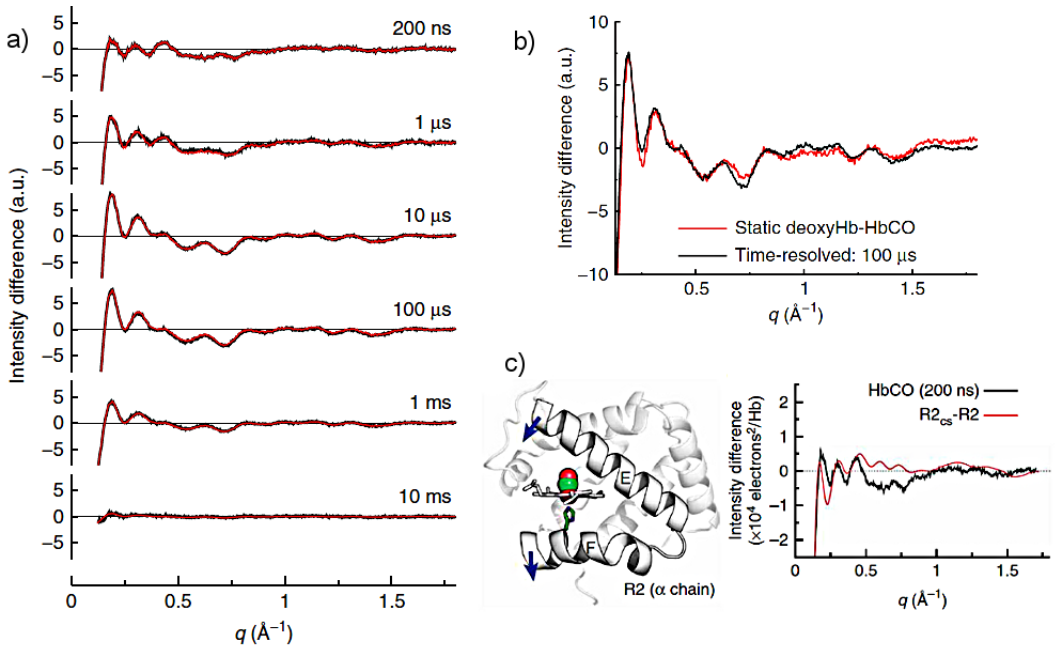

Figure 1.9: Panel a) Time resolved X-ray scattering patterns obtained on HbCO sample after photolysis (black) and reconstruction of the data-set as a linear combination of 200 ns and 100 μs patterns (red). Panel b) Time resolved data at 100 μs after photolysis compared with the static equilibrium scattering difference between a deoxy-Hb equilibrium sample and an HbCO sample. Panel c) Snapshot of the CO-bound alpha subunit. The E and F helices form the "clamshell" that holds the heme in place. The blue arrows indicate the direction of the E and F motion during the "clamshell relaxation". Comparison of the 200 ns time-resolved data with the difference pattern calculated from the R2 crystal structure and its modified unligated version mimicking the effect of the clamshell relaxation. The figure is taken from Cammarata et al. 2008 [17].

Chapter 2

Time Resolved X-Ray Scattering on protein solutions

In this chapter a brief overview of the basic principles of X-ray scattering is given, to clarify how it is possible obtain direct structural information on molecules in solution. The principles of the pump and probe technique and data collection strategy are then presented: the temporal structure of X-ray pulses at the synchrotron (European Synchrotron Radiation Facility in Grenoble-France), where the experiments presented in this thesis have been performed, naturally bring to the possibility of time-resolved experiments using the pump and probe approach. In the case of time resolved X-ray scattering the triggering pump is a laser pulse while the probe are X-ray pulses produced by the synchrotron. The specific experimental set-up on beamline ID09B at the ESRF, where the experiments presented in this thesis have been performed, is also described.

2.1 X-Ray scattering: from free electrons to proteins

2.1.1 X-Ray scattering from a free electron

When an X-ray beam impinges on an atom the beam may be scattered or absorbed with the ejection of electrons. This section is focused on the scattering process, considering that at the X-ray energy (18 keV) used during the experiments described in the next chapters the absorption of the sample is negligible. To start, the scattering process can be treated in terms of classical theory and the primary beam is an electromagnetic plane wave. Let's consider the case of a single electron as scatterer.

The electric field exerts forces on the electron producing an acceleration. According to classical electromagnetic theory, once the electron has been accelerated radiates. In the case of elastic scattering this radiation spreads out in all directions from the electron and has the same frequency as the primary beam. In a quantum mechanical description the incident X-ray photon has an energy $\hbar\ \omega$ and a momentum $\hbar$ K. Energy may be transferred to the electron and as a consequence the frequency of the scattered photon is lower than the incident one. This process is called Compton scattering and because of its incoherent nature it does not give rise to an interference pattern. As far as diffraction experiments are concerned it gives rise to a smoothly varying background which sometimes need to be subtracted from data (its contribution is significant when the energy of the incoming photon is comparable with the rest mass energy of the electron $mc^2 = 511keV$). However the elastic scattering of X-rays is the main process that is exploited in investigation of the structure materials, and in this case it is mostly sufficient to adopt a classical description. Of course also in the elastic case a momentum is transferred to the electron and this leads to the definition of the scattering vector **q**

$$\hbar\mathbf{q} = \hbar\mathbf{k} - \hbar\mathbf{k'} \tag{2.1}$$

where $\hbar$ **k** and $\hbar$ **k'** are the initial and final momenta of the photon respectively and **q** is the scattering vector usually expressed in units of $\mathring{A}^{-1}$.

The field emitted by the electron in the far-filed limit is [59]:

$$E_{rad}(R,t) = -\frac{-e}{4\pi\epsilon_0 c^2 R} a_X(t') \tag{2.2}$$

where R is the distance between the observer and the electron and $a_X(t')$ is the acceleration seen by the observer at X and at the time $t' = t - R/c$.

The acceleration calculated as the force divided by mass is:

$$a_X(t') = -\frac{-e}{m} E_{in} e^{i\omega(\frac{R}{c})} cos\psi \tag{2.3}$$

where E_{in} is the incident electric field.

Combining the 2.2 and the 2.3 the ratio of scattered and incident field can be written as:

$$\frac{E_{rad}(R,t)}{E_{in}} = -\left(\frac{e^2}{4\pi\epsilon_0 mc^2}\right)\frac{e^{ikR}}{R} cos\psi \tag{2.4}$$

By convention the prefactor in parentheses is denoted by r_0 and it is called Thompson scattering length. Usually in a scattering experiment intensity is

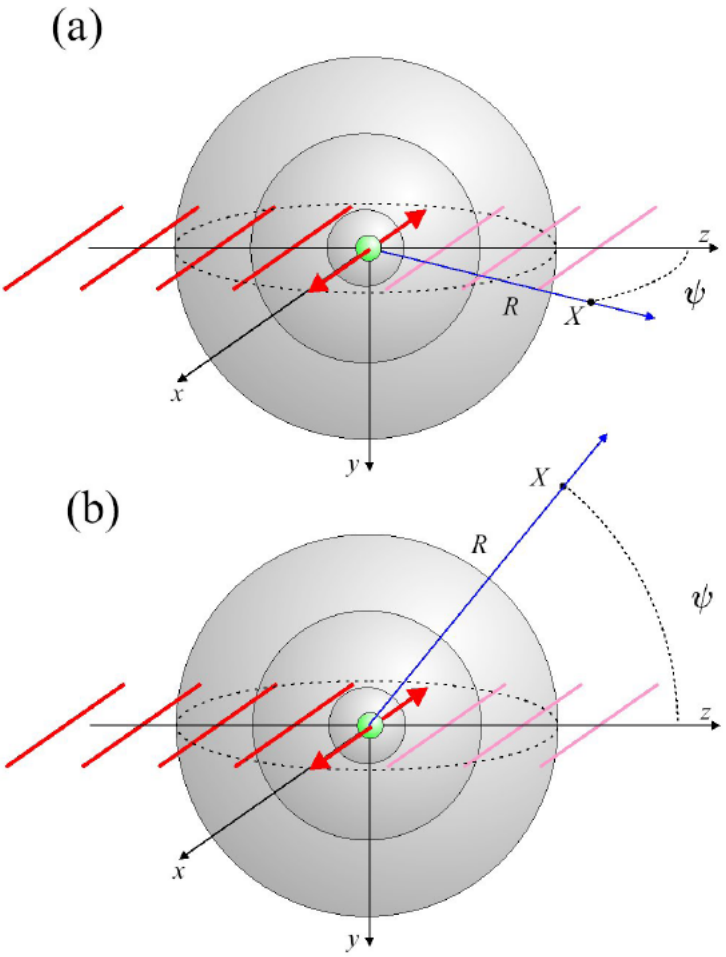

Figure 2.1: The classical description of the scattering of an X-ray by an electron. The incident wave propagates along the z axis and it is polarised along x. The radiated field can be calculated depending on the observation point X: (a) the point X is in the same plane as the polarisation of the incident wave, and the observed acceleration has to be multiplied by a factor cosψ; (b) the observation point X is in the plane normal to the incident polarisation and the full acceleration of the electron is seen at all scattering angles. The figure is taken from the reference [59].

recorded by X-ray detectors in a solid angle $\Delta\Omega$ subtended by the detector. If I_0 is the incident beam intensity with a cross-sectional area A_0 and $R^2\Delta\Omega$ is the cross-sectional area of the scattered beam, the ratio of scattered and incident intensity is easily calculated as:

$$\frac{I_{sc}}{I_0} = \frac{|E_{rad}|^2 R^2 \Delta\Omega}{|E_{in}|^2 A_0} \tag{2.5}$$

Normalizing the scattered intensity by the incident flux I_0/A_0 and the solid angle of the detector differential cross section for Thompson scattering is obtained.

$$\left(\frac{d\sigma}{d\omega}\right) = \frac{I_{sc}}{(I_0/A_0)\Delta\Omega} = \frac{|E_{rad}|^2 R^2}{|E_{in}|^2} = r_0^2 cos^2\psi \tag{2.6}$$

The factor $cos\psi$ arises from the projection of the acceleration on the sight direction assuming that the incident wave and the observer are on the same plane [60]. If the polarization of the incident wave is orthogonal to the plane of observation the factor $cos\psi$ has to be replaced by 1. More in general and referring to the case of synchrotron source then

$$\left(\frac{d\sigma}{d\omega}\right) = r_0^2 P \tag{2.7}$$

$P = 1$ Synchrotron: vertical scattering plane
$P = cos^2\psi$ Synchrotron: horizontal scattering plane
$P = \frac{1}{2}(1 + cos^2\psi)$ Unpolarized source

The fact that in a synchrotron the electrons orbit in the horizontal plane explains the presence of a polarization factor for a synchrotron source: the acceleration of the electrons is then in the same plane and the resulting X-ray emitted are linearly polarized in the horizontal plane [61].

2.1.2 X-Ray scattering from atoms and molecules

In this paragraph the scattering from atoms and molecules is considered, starting from the elementary concepts introduced in the case of a single electron. Adopting a classical description, the atomic electron clouds can be described by an electron density ρ ($\mathbf{r}$). The scattered field is then a superposition of the different contributions arising from different volume elements of this charge distribution. To evaluate this superposition it is necessary to consider the phase difference between the incident wave interacting with a volume element at the origin and one located at $\mathbf{r}$: the phase difference is

2π multiplied by the ratio of **r** projected onto the incident direction and the wavelength, i.e. the scalar product between **k** (wave vector) and **r**. In the vicinity of the observation point the scattered wave is locally a plane wave with wave vector **k'**. The phase difference between the scattered wave from a volume element around the origin and one centered at **r** is $-\mathbf{k'} \cdot \mathbf{r}$. The resulting phase difference is then:

$$\Delta\phi(\mathbf{r}) = (\mathbf{k}\text{-}\mathbf{k'}) \cdot \mathbf{r} = \mathbf{q} \cdot \mathbf{r} \tag{2.8}$$

where **q** is the scattering vector. The scattering considered is elastic then $|\mathbf{k}| = |\mathbf{k'}|$ and $|\mathbf{q}| = 2|\mathbf{k}|sin\theta = (4\pi/\lambda)sin\theta$ (see figure 2.2). Considering that a volume element d**r** at **r** contributes an amount $-r_0\rho(\mathbf{r}d\mathbf{r})$ to the scattered field with a phase factor $e^{i\mathbf{q}\cdot\mathbf{r}}$, the total scattering contribution of an atom is:

$$-r_0 f(\mathbf{q}) = -r_0 \int \rho(\mathbf{r}) e^{i\mathbf{q}\cdot\mathbf{r}} d\mathbf{r} \tag{2.9}$$

where f(**q**) is the atomic form factor. Of course at q=0 all the different volume elements scatter in phase and so that $f(0) = Z$ where Z is the number of electrons in the atom. In a scattering experiment the measured quantity is the number of photons scattered per unit of solid angle:

$$S(\mathbf{q}) \equiv \frac{\delta I_{sc}(\mathbf{q})}{\delta\Omega} = I_0 r_0^2 P f^*(\mathbf{q}) f(\mathbf{q}) \tag{2.10}$$

where P is the already mentioned polarization factor and the symbol * indicates the complex conjugate.
When a molecule made of N atoms is considered the expression reported above has to be modified considering the contributions arising from the different atoms in the molecule. Assuming the electrons localized within the atoms, the form factor for a molecule is:

$$f^{mol}(\mathbf{q}) = \sum_{\mathbf{r}_j} f_j(\mathbf{q}) e^{i\mathbf{q}\cdot\mathbf{r}} \tag{2.11}$$

The above equation can be simplified in the approximation of *spherical* atoms: in that case it is possible to consider the atomic form factor isotropic and substitute **q** with its module.

2.1.3 X-ray scattering from an ensemble of isotropically oriented molecules: Debye formula

Having summarized the formulas describing the intensity of the scattered X-ray beam from an ensemble of atoms, in this section the attention is focused on the scattering from an ensemble of independent molecules [59]. The

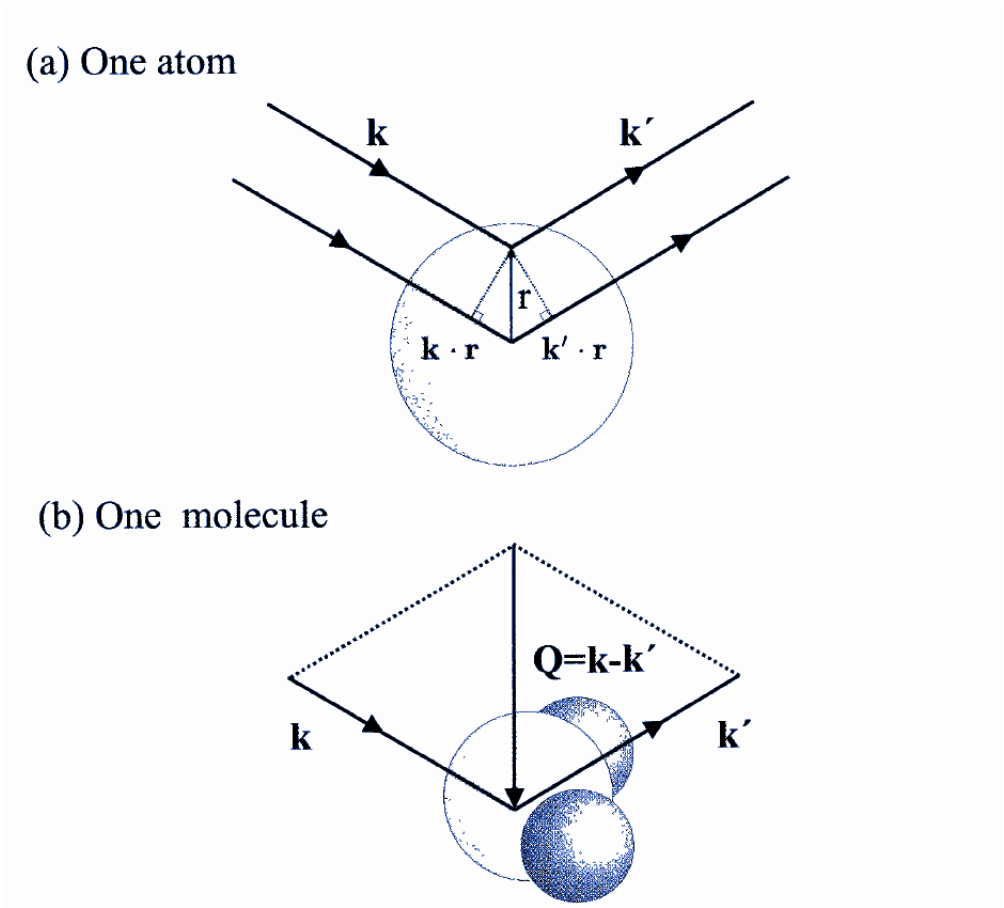

Figure 2.2: (a) Scattering from an atom. **k** and **k'** are the initial and final wave vector of incident and scattered wave respectively: assuming the scattering elastic $|\mathbf{k}| = |\mathbf{k'}|$; (b) Scattering form a molecule. The figure is taken from the reference [59].

scattering from independent molecules is (considering 2.11 and the approximation of spherical atoms):

$$S(q) = \sum_{i.j} f_i(q) f_j^*(q) e^{i\mathbf{q}\cdot\mathbf{r}_{i,j}} \tag{2.12}$$

being $r_{i,j} = |\mathbf{r}_i - \mathbf{r}_j|$.
Given the isotropy of the molecular orientations, this equation can be integrated over all the possible directions giving:

$$S(q) = \sum_{i.j} f_i(q) f_j^*(q) \frac{sinqr_{i,j}}{qr_{i,j}} \tag{2.13}$$

The isotropic condition required by Debye formula does not mean that the system has to be necessarily isotropic in the microscopic sense, but only that the illuminated volume is made of a statistical ensemble of sub-system randomly oriented.

2.1.4 Protein solution scattering

In this section a brief discussion of scattering from protein solution is presented and the interested reader can find a deeper discussion of (protein) solution scattering in [62] and references therein. The Debye formula can be successfully applied to the case of dilute solutions of proteins and it is the starting point for analysis of data collected by solution scattering techniques (Small Angle X-ray Scattering or Wide Angle X-ray Scattering). Usually, because of the isotropic condition of Debye formula, intensity recorded by bi-dimensional X-ray detectors is azimuthally averaged (the intensity is integrated over annular regions corresponding to a certain scattering angle and then to a certain scattering vector) resulting in unidimensional I(q) scattering pattern. Calling D the maximum protein linear dimension, for scattering vector $q \leq 1/D$ most of the scattered intensity is found. Because proteins are usually dissolved in relatively low concentration ($0.01 - 1\%$ volume fraction) solution, for many years the low q region defined above has been the only one experimentally accessible. Recently thanks to advances in x-ray sources, most notably synchrotron based ones, the higher q region has been studied. At higher q only short distance correlations contribute to the scattering intensity (see equation 2.13) giving high resolution informations on the protein structure. In particular the scattering pattern of a protein can be schematically divided into different regions as illustrated by 2.3. It can be shown that going from low to high q different contributions are predominant going from overall shape to inter-domain correlations (regions A and B in the figure),

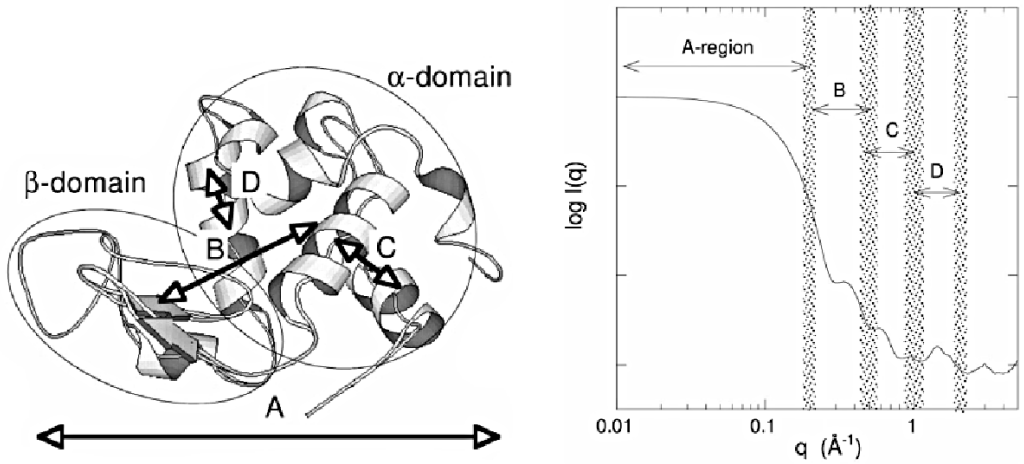

Figure 2.3: left panel: protein structure; right panel: corresponding scattering pattern; the figure has been taken from Hirai et al. 2002 [63].

and from inter-helices to intra-helices correlations (regions C and D). It is interesting that even if it is not possible to directly reconstruct the structure of a protein from the solution scattering pattern, the comparison between models and experimental data is in principle straightforward. In fact if the location of the atoms in the protein structure is known, the Debye formula allows to calculate the scattering pattern associated. Comparison between experimental X-ray solution scattering curves and those evaluated from crystallographic structures have been widely used to validate theoretical models and to predict quaternary structures [66] [67].
The main problem in evaluating the solution scattering from atomic coordinates is to take into account the solvent scattering: in particular in the case of proteins the contribution to the scattering from hydration shell is not negligible even at low q values ([64] and references therein). In a standard solution X-ray scattering experiment, the contribution of the buffer solution and of the capillary is measured to be subtracted from the experimental data. Nevertheless, this procedure does not cancel out the contribution to the scattering of the solvation shell of the proteins that has an electronic density higher than the bulk solvent. This contribution has to be taken into account when comparing experimental data with models or crystallographic structures. To overcome this problem different softwares like CRYSOL [65] are now available. This program uses multipole expansion for fast calculation of the spherically averaged scattering pattern and takes into account the

hydration shell using two free parameter, the average displaced volume per atomic group and the contrast (in terms of electronic density) of the hydration layer. For details the interested reader can refer to [65]. To show some examples of scattering curves that are usually obtained in protein scattering experiments and to introduce some of important features in the typical scattering curve of a protein, the scattering calculated from crystallographic structures of Hemoglobin (R and T quaternary states) are reported in 2.4. From the figure it is clear how collecting data at high values of scattering vector allows to get structural information on the protein studied. Considering the main subject of this thesis, it is particularly interesting to note that differences between the two quaternary conformations of Hemoglobin are significant in the wide angle region. Wide angle scattering technique allows then to track conformational changes of proteins if an adequate time-resolved set-up is available. The description of the experimental strategy to collect time resolved wide angle scattering data on protein solutions is the argument of next paragraphs.

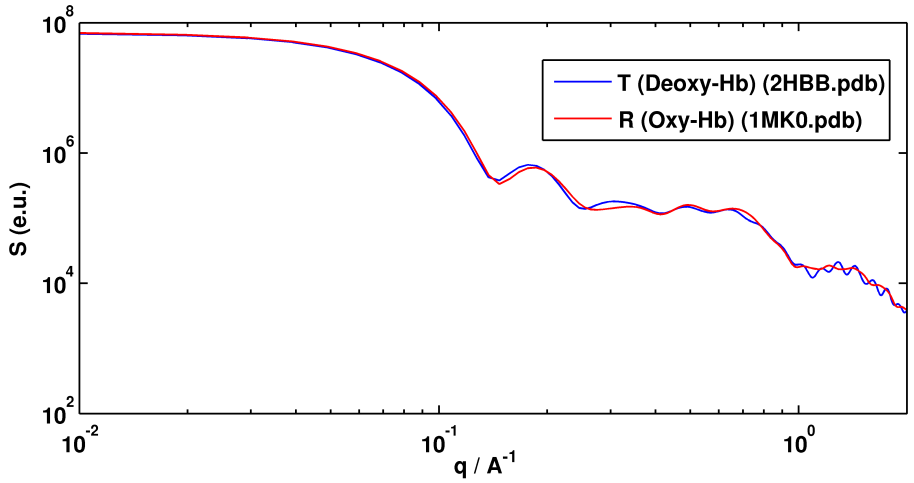

Figure 2.4: Scattering pattern calculated by CRYSOL from pdb files of Hb in T state and R state

2.2 The Pump and Probe Technique at ID09B beamline

In a time-resolved scattering experiment the scattering pattern is probed in a definite interval of time. In principle a fast detector could record the

time-dependency of the signal, while it has to satisfy several requirements:

- High spatial resolution to resolve the oscillations of the S(q) pattern.
- Especially for protein solution scattering, it is important to collect a large q range in the same measurement.
- Because the efficiency of the scattering process is weak (1 photon in 10^6 incident photons for protein solution at millimolar concentration [68]) it is crucial in many experiments have a large angular acceptance to increase statistic of the radial average.

All these requirements can be achieved by two dimensional detectors with large area and high number of pixels but, with all possible compromises, detectors faster than $\sim$ 1ms are not available yet. Another strategy is suggested by optical pump and probe experiments, where transient phenomena are triggered by an external event, as for example a laser pulse. In this paragraph the experimental approach of pump and probe technique applied to X-ray scattering is presented. The aim is to track photo-induced atomic motions of proteins in solution during a conformational change (like quaternary transition in hemoglobin). Scattering intensity of the system has then to be collected as a function of q and as a function of the time after having optically triggered the reaction. This is done using a stroboscopic pump and probe approach which is described below.
Let's start from the schematic drawing (figure 2.5) of the experimental set-up to understand how the data are collected in a typical TR-WAXS experiment. The specifics of the most important components are discussed in more detail in the next section. A laser pulse is used to excite a subset of solutes in the solution which is sealed in a capillary (or a specific sample cell in the case of the red blood cells experiment). The laser triggers the chemical reaction we are interested in: in the case of hemoglobin the ligated form with CO (HbCO, in the quaternary R-state) is photodissociated by a 532 nm laser pulse and the dissociation causes a fraction of the total concentration going into the T state (the most stable when Hb is unligated). The whole process is called quaternary transition of Hb. A delayed 100ps long X-ray pulse probes the structure of the excited system (for long time delay a longer X-ray pulse can be used). The scattering pattern, which is averaged over the duration of X-ray pulse, the time it takes for the pulse to cross a quasi stationary molecule, is detected by a 2-D Frelon detector [72], which is centred on the incoming beam. The intensity is measured as a function of the scattering vector q and the time delay between the laser and the X-ray pulses. In the case of protein solutions the scattered intensity is azimuthally averaged due

to the isotropy of the sample and differences can be calculated between the patterns S(q) recorded before and after the laser initiates the reaction. How it is commented in the next paragraphs the calculation of difference patterns has different advantages.

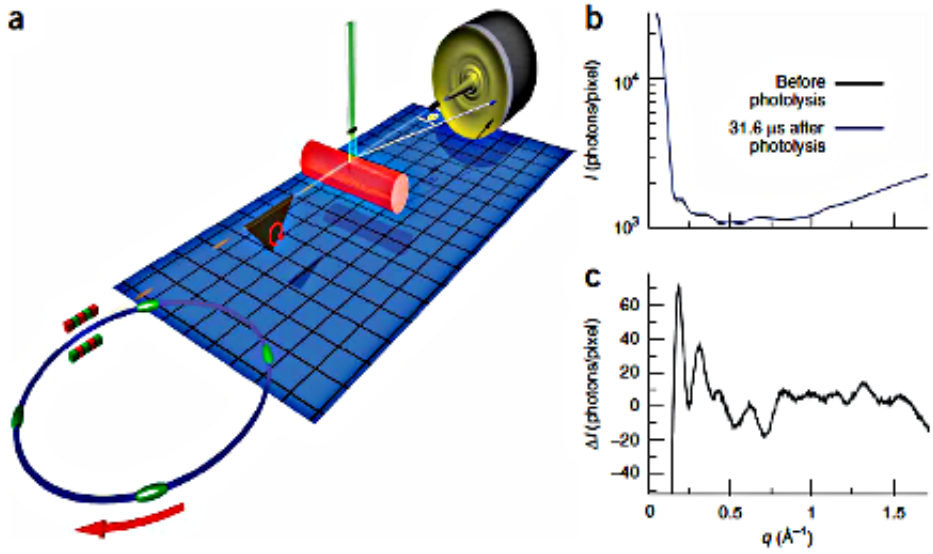

Figure 2.5: Schematic drawing of the experimental set-up for TR-WAXS at ID09b (ESRF). a) A short laser pulse can be used to break the protein-ligand bond without altering/disrupting the protein. Transient structures are then followed by delayed X-ray pulses. Structural changes occurring in the sample leave their "fingerprints" in the differences (c) between the signals measured before and after (b) the laser initiates the reaction ("laser on" - "laser off") and can be monitored as a function of time. Using difference signals systematic errors cancel out.

2.2.1 Synchrotron Radiation of ESRF: the probe

Synchrotron radiation (SR) is emitted by electrons (or other charged particles) moving at relativistic speed and following curved trajectories under the forces exerted by electric or magnetic fields. The radiation is emitted in a narrow cone in the direction of the motion and, in particle accelerators, is extremely intense and extends over a broad energy range from the infrared into the soft and hard X-ray regions of the electromagnetic spectrum. Due to these and other characteristics, SR has become a fundamental tool to

study several different aspects of the structure of matter at the atomic and molecular level. The circular accelerator (storage ring) used to produce SR affects the main properties of the radiation produced: the most important parameters are the high intensity, high collimation as well as the pulsed time structure ideal for time resolved studies.
The properties of SR can be calculated by applying the methods of classical electrodynamics to the motion of relativistic charged particles and are the subject of different books [59] [69]. The interested reader can refer to these books for a complete account of the properties of synchrotron radiation. Here only the characteristics of European Synchrotron Radiation Facility are reported. Pulsed time structure is also commented in some detail because it is what makes X-rays a particularly suitable probe for the present study.
ESRF is the most powerful third generation synchrotron in Europe and it can produce hard X-rays above 10 keV with high brilliance. In a typical synchrotron the electrons are emitted by an electron gun and then accelerated in a linear accelerator (linac). Subsequently the electrons are transmitted to a circular accelerator (booster), where they are accelerated to 6 GeV. These high-energy electrons are then injected into a large storage ring (844 meters in circumference) where they circulate in a vacuum chamber, at a constant energy which is maintained by a radio frequency (RF) field. The electrons in the storage ring are distributed between different bunches whose number depends on the filling mode and having a duration of 100ps each. According to the lifetime of the beam a new injection is done each 60 or 10 hours, depending on the operating mode.
The storage ring is made up of straight and curved sections. As they travel around the ring the electrons are manipulated in order to produce the X-ray radiation by two types of devices, bending magnets and undulators, depending on the characteristics required. When the electrons pass through bending magnets, they are deflected from their straight path by 11.25 degrees emitting a weak incoherent radiation. Bending magnets are used both as a source of X-ray and as a device to force the electrons into a circular orbit. When passing through the insertion devices or undulators, the electrons undergo undulations forced by an array of magnets with alternating polarity. The beams of radiation emitted from the different bends interfere with each other to generate a bright and partially coherent beam which is up to 1000 times more intense than the one generated by bending magnets. Moreover the radiation produced by undulators has a narrow energy distribution around a principal peak and it is called for this reason quasi-monochromatic ($\Delta E/E \sim 3\%$). In order to focus the electron beam and to keep it stable focusing magnets are placed in the straight sections of the storage ring. Depending on the number of bunches injected in the storage ring different timing modes are defined as

shown in figure 2.6. The rate at which a single bunch circulates in the ring is a sub-harmonic of the RF frequency. At the ESRF the RF frequency is 352.2 MHz, which allows having up to 992 bunches, separated in time by 2.84 ns, around the 844.1 m long ring.

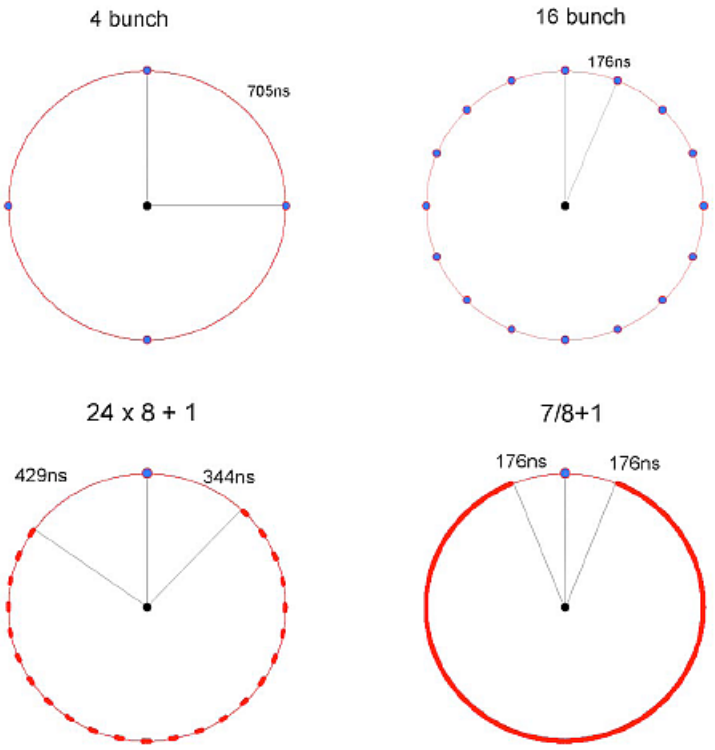

Figure 2.6: Filling patterns suitable for single-pulse pump-probe experiments at the ESRF: 4-bunch mode (40 mA), 16-bunch mode (90 mA), hybrid mode 24/8+1 (200 mA), and 7/8 mode (200 mA) [74].

The electrons loose, during each turn, part of their energy to synchrotron radiation, while the energy lost is compensated passing through the radio frequency cavities. In a RF cavity a longitudinal electric field is generated in order to accelerate the electrons. The RF fields have their proper frequency and only synchronous electrons, i.e. electrons entering the cavity in phase with the oscillation of the electric field, will be in a stable condition. In this case they will continue their motion along the ring returning in the RF again in time to regain the exact amount of energy lost in the circular path. Slower or faster electrons with respect to the synchronous ones would need higher or lower energy to compensate their energy loss and therefore they will be lost. In fact all the electrons passing through the cavity out of

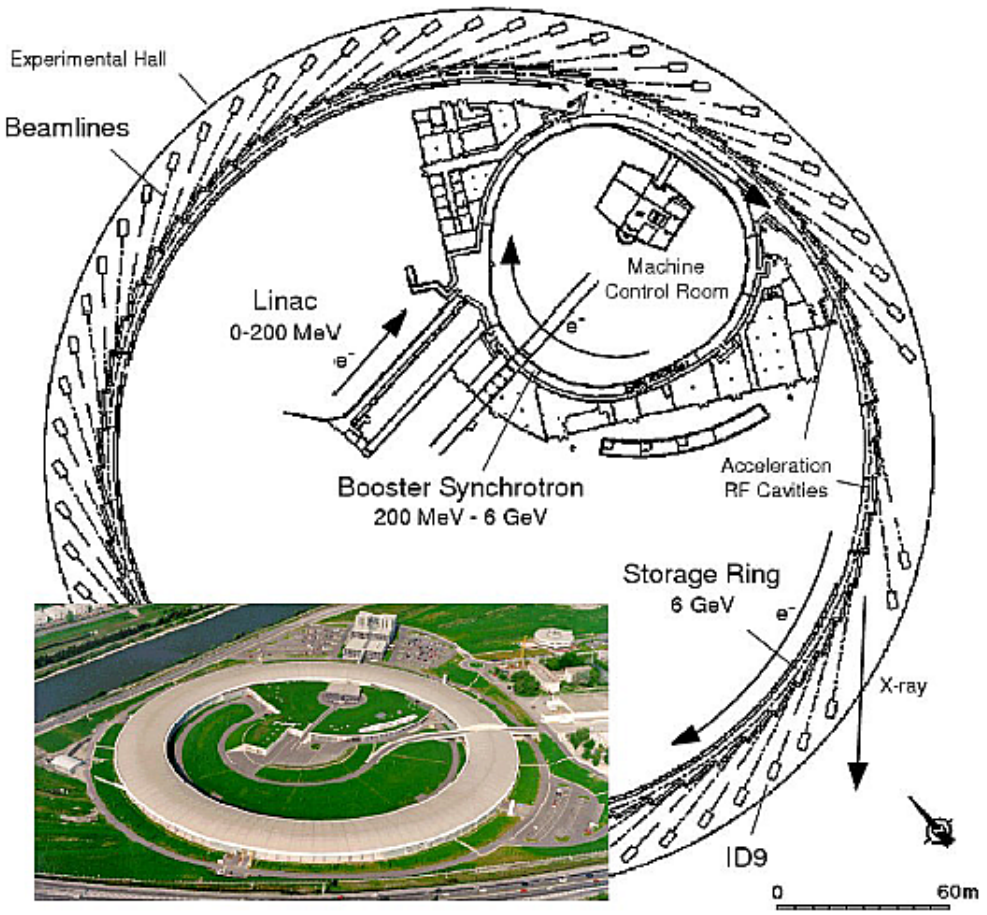

Figure 2.7: Sketch of the different parts of the ESRF

phase will not follow the ideal orbit of the ring and are therefore lost. As a consequence the electrons in the storage ring are grouped in bunches with a time length which is typically $5\% - 10\%$ of the RF period. As a consequence the emitted synchrotron radiation appears in pulses with the same duration which determines the highest achievable time resolution in our experiment. At the ESRF the temporal pulse length of an X-ray pulse is 100 ps (fwhm).

2.2.2 ID09 Beamline

The ID09 beamline (the prefix ID stands for insertion device) has been built with the characteristic of being able to have a white beam focused on the sample; white beam means that the total emission of the insertion device is used without going through a monochromator. This, together with tailored ID, allows very high flux (x 1000 times higher than in the standard monochromatic beam). ID09 is working for about 50% of the time for high pressure studies (ID09a) and for half of the time to time resolved studies (ID09b). The ID09b beamline starts within the storage ring where the ID is present and it is divided into two sections the "optics hutch" where the heat load chopper and focusing X-ray optics are hosted and the "experimental hutch" where the high speed chopper detectors and the laser system are hosted. The X-ray source at ID09B is a narrow band in-vacuum undulator, the U17, named after its 17 mm magnetic period, which determines the characteristics of the X-ray radiation produced on ID09. The X-ray beam needs then to be aligned and focused onto the sample using X-ray optics, the X-ray optical devices in the optics hutch. In order to perform time resolved experiments, a single X-ray pulse can be selected from the train of pulses from the undulator. This is done just before the sample, in the experimental hutch by the "high speed" chopper. In this section some details of the most important X-ray devices are presented as well as the laser and the synchronization between the pump and the probe. The latter controls the time delay at which the structure of the sample during the reaction is probed [70] [71].

2.2.3 The undulator U17

Undulator U17 is the first element of the beamline and produces X-ray pulses with up to 10^{10} photons per pulse. It has 236 magnetic poles with 17mm period. The magnets are placed inside the vacuum vessel for the electron beam and it is possible to move the magnets very close to the electron beam increasing the field and deflection. The energy of the X-ray can be varied from 15 to 20 keV changing the gap. The spectrum produced is dominated by a single peak with a sharp energy cut-off at 18 keV at 9 mm gap, with

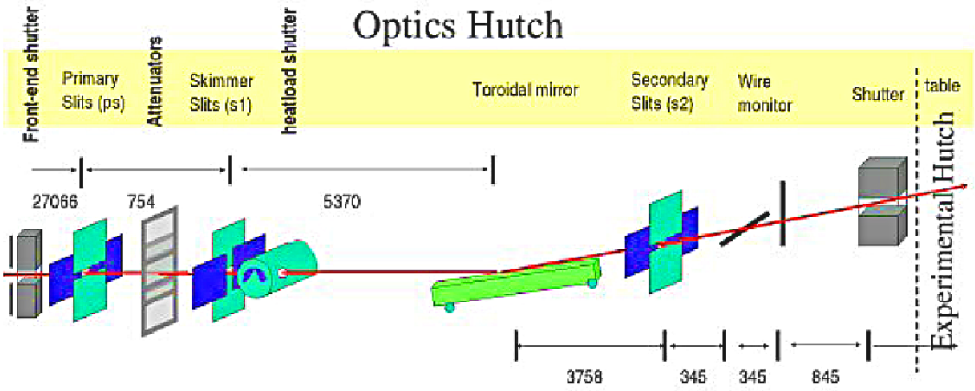

Figure 2.8: Schematic drawing of the optics hutch in the layout used for the experiment described in the this thesis; upstream the mirror there is a Si(111) monochromator; the distances are in mm.

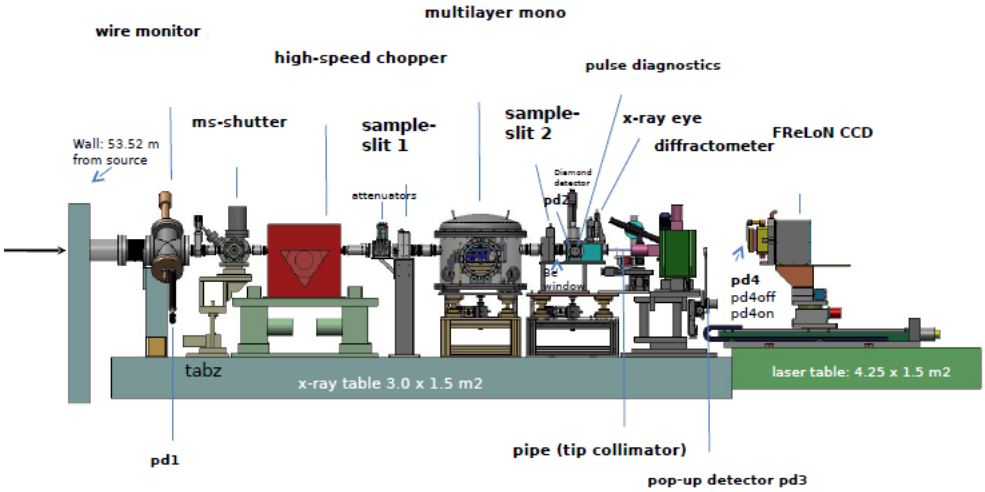

Figure 2.9: Schematic drawing of the experimental hutch in the layout used for the experiment described in the this thesis

a bandwidth $\Delta E/E = 3\%$, followed by a broad second harmonic. The 3% bandwidth of the undulator represents a good compromise between energy resolution and intensity for most diffraction experiments in liquids. In fact, because of the definition of the scattering vector q depends on the incident wavelength λ, the bandwidth of the source limits the resolution in q space of the patterns recorded. At the same time, extremely intense X-rays are needed to discern the photo-signal from the solvent background with reasonably short exposure time (10s) [17]. In using the natural line width of the undulator we can gain up to two orders of magnitude in flux as compared to a monochromatic beam from a Si(111) monochromator [71] while preserving the resolution of the scattering patterns.

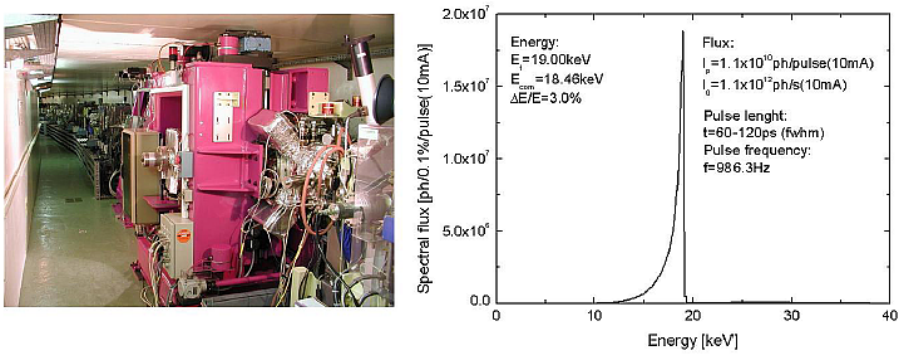

Figure 2.10: The in-vacuum U17 undulator on ID09B beamline and its spectral intensity [73].

2.2.4 The heatload chopper

To reduce the heating on X-ray optics and the high speed chopper, a water cooled heatload chopper was installed upstream the monochromator and mirror in the optics hutch. The heatload chopper is a Cu disk that rotates in vacuum about a horizontal axis perpendicular to the beam. The radius of the disk is 75 mm and the disk has five tunnels (figure 2.11). The tunnels are 4 mm high, 8 mm wide, and 150 mm long. Normally the disk rotates at 98.63 Hz at the 3600 subharmonic of the orbit frequency, i.e. ten times slower than the high-speed chopper. As the five tunnels open ten times per revolution, the heatload chopper produces pulses at 986.3 Hz in phase with the high-speed chopper. For a typical white beam in 16-bunch mode at 90 mA, the heatload chopper reduces the power from 62 to 4.8 W [74].

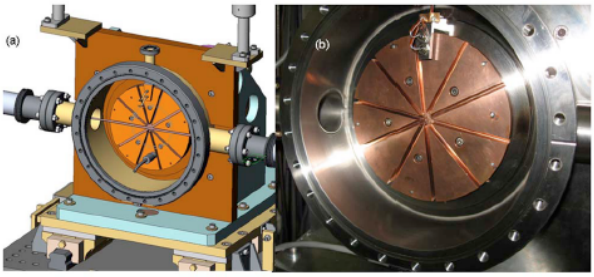

Figure 2.11: The heatload chopper, figure from [74]:(a) Drawing of chopper rotor in its vacuum vessel. The position of the chopper relative to the x-ray beam is optimized by motorized translation in the vertical and horizontal directions. (b) Photo of the five-tunnel rotor in its vacuum vessel. The rotor position is sensed by a coil located near the top of the photo. This coil generates a current pulse when the pickup magnets pass by (seen as gray dots near the periphery of the rotor).

2.2.5 The focusing mirror

An X-ray mirror refocuses the diverging beam in the horizontal and vertical to the sample position, 55.3 m from the source. The mirror is polished to a cylindrical shape with 64.5 mm radius. It is supported close to its ends and bends under its own weight to a toroid Its body is made out of sintered graphite with a 200 μm coating of silicon carbide as a hard substrate for the polishing process. A 500 $\mathring{A}$ thick layer of platinum is deposited on to the polished silicon carbide via an intermediate binding layer. X-ray mirrors work in grazing incidence. All materials have a refractive index slightly smaller than 1 for X-rays. So at very shallow incidence angles, total external reflection occurs.

2.2.6 The single pulse selection: chopper and shutter system

The task of the chopper represented in figure 2.14 is to select one out of the train of pulses produced by the synchrotron; it is made by a titanium triangular shaped object; the radius is about 97 mm and the revolution frequency is 986.3 Hz that is the 360th sub-harmonic of the storage-ring frequency [71]. In one of the three sides, a tunnel is present; the cross section is shown in figure 2.13. For such a system it can be shown that the opening window has a baseline of $h/l\pi f$ where h is the tunnel height, l is the length of the side and f the revolution frequency. In 16 bunches filling mode the

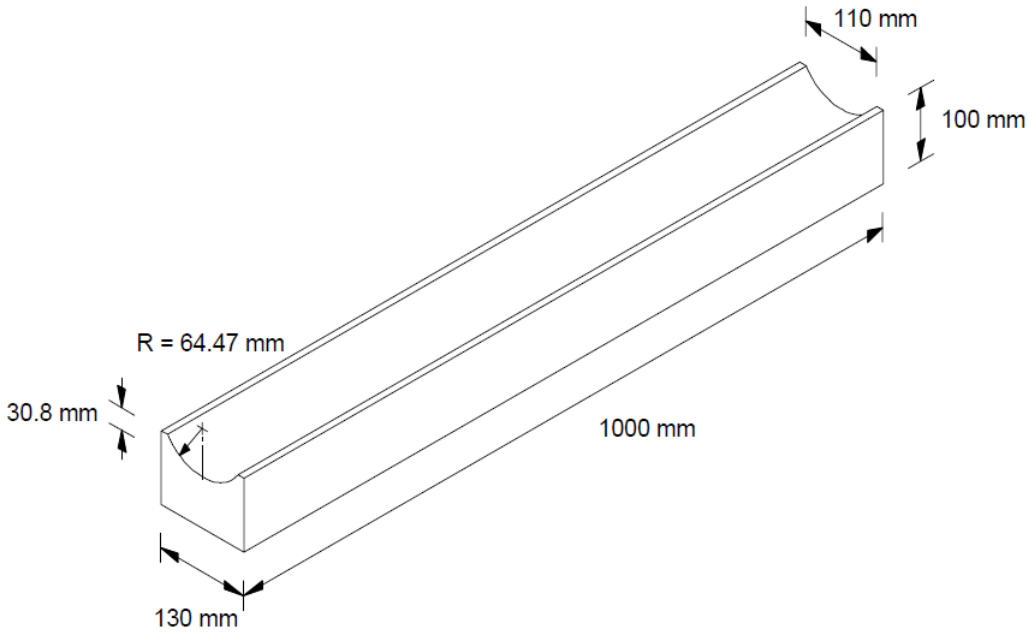

Figure 2.12: Focusing X-ray mirror. The mirror is polished as a cylindrical mirror and bends into toroidal shape in its support; material: graphite; coating: platinum.

bunch spacing is 176 ns; the opening time has to be smaller than twice this number; as shown in the right panel of figure 2.13 a tunnel of about 100 μm is required. For this reason the X-ray beam has to be focus to smaller dimension than the tunnel height and the position has to be extremely stable. The chopper has also the possibility to be used in a tunnel-less configuration allowing a continuous (single pulse to several μs) opening time.

Because the revolution frequency of the high speed chopper is almost 1 kHz, downstream an X-ray pulse would in principle impinge on the sample each millisecond (probe rate 1 kHz). For time resolved experiments on protein solutions it is often required to reduce the rate to 10-1 Hz range. In order to get a pulse each 0.1-1 s a fast mechanical shutter, represented in figure 2.15 and called millisecond shutter because its opening time is 1 ms, it is used to select a sub-train of the pulses getting out from the high speed chopper. A complete scheme resuming the role of different choppers and ms-shutter used for single pulse selection is represented in figure 2.16.

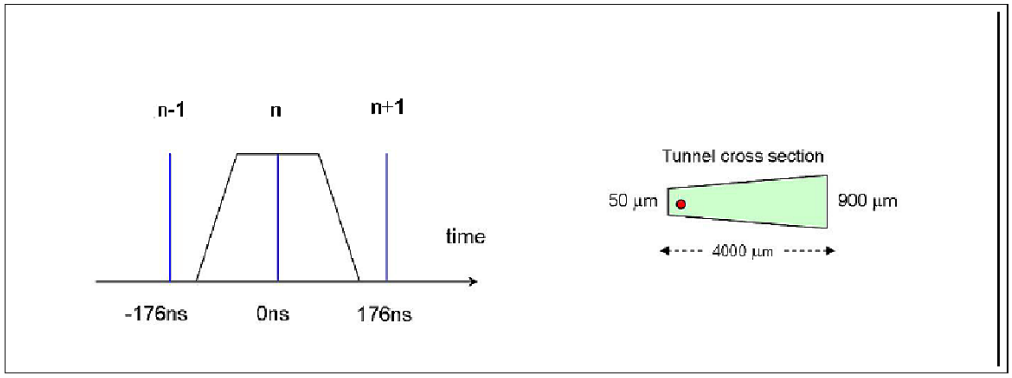

Figure 2.13: The temporal acceptance window for single pulse selection in 16 bunch mode is shown on the left. On the right panel it is shown the trapezoidal shape of the chopper tunnel.

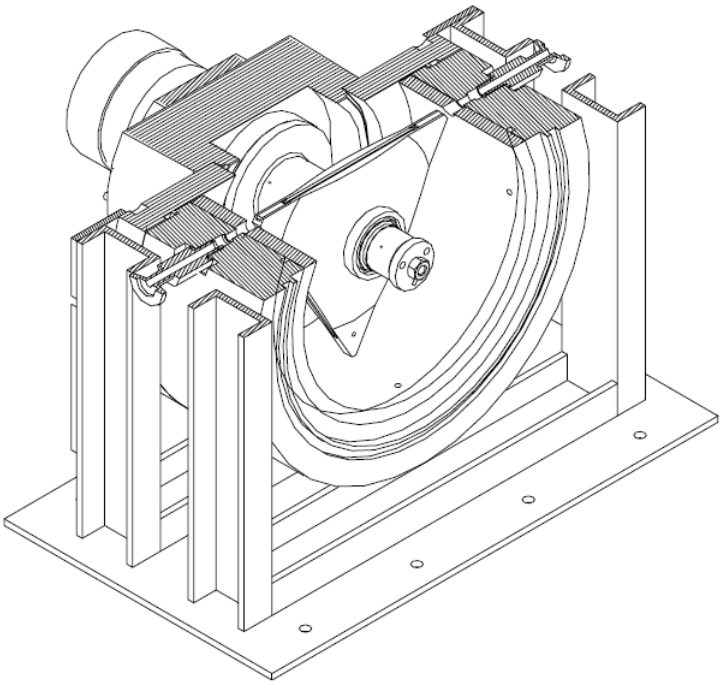

Figure 2.14: X-ray chopper (bunch selector) by Forschungszentrum Jülich.

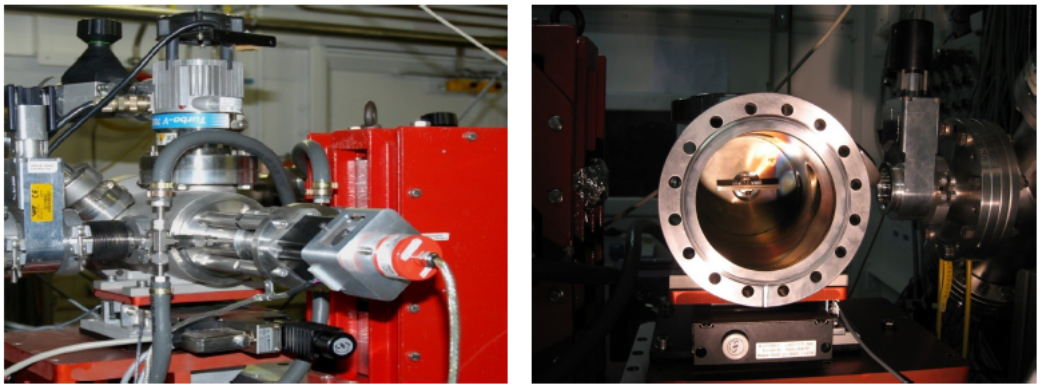

Figure 2.15: X-ray millisecond shutter: the fast mechanical shutter has the shape of a tunnel and it can pass from *open position* (tunnel parallel to X-ray incoming direction) to *closed* in about 1 ms

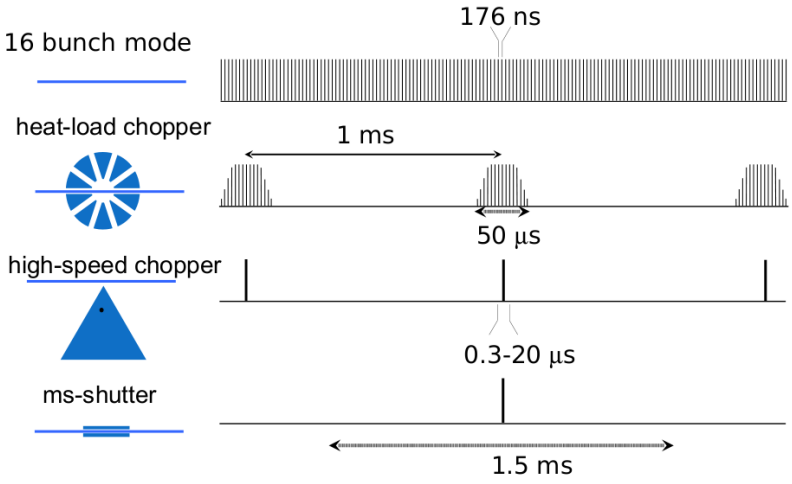

Figure 2.16: When operated in 16-bunch mode, the ESRF produces a train of about 100 ps x-ray pulses separated by 176 ns. This pulse train is first chopped by the heatload chopper into 50 μs (FWHM) macrobunches at 1 kHz, thereby reducing by a factor of 20 the transmitted average power striking the x-ray focusing mirror and other downstream components. The millisecond shutter opens on demand to isolate one heatload chopper macrobunch from the 1 kHz train of bunches. The high-speed chopper isolates a single pulse from the center of the transmitted macrobunch.

2.2.7 X-ray detectors

Several kinds of detectors are used on the beamline as diagnostic tools for the X-ray alignment, for the determination of the absolute time delay between the X-ray pulse and the laser pulse and to collect diffracted intensities. The main characteristics of the different detectors used are presented in this section. The alignment procedure to bring the beam from the undulator to the sample position requires the use of three pindiode and two wire detectors to check both position and intensity of the beam in the optics and experimental hutches. A very fast detector (rising time $\sim$ 20 ps), sensitive to both X-ray and laser radiation allows to measure the time delay between the pump and probe. It consists of a GaAs photoconductor that is operated with a bias voltage of +400V. On a fast digital oscilloscope (Tekronix TDS 694C, 3GHz) the time-trace of the signal can be recorded with a jitter of less than 10ps. The resolution of the laser/X-ray time delay for the detector and oscilloscope has a time resolution of 10-20ps when the mid-point of the rising edges are used. A Cyberstar scintillation counter, which picks up air scattering from the X-ray beam, is used both for timing and evaluating the I0 intensity that is actually impinging on the sample. This detector gives a (rising edge) time resolution of about 3ns. It is placed directly behind the sample slits, 40cm from the sample. The detector used to record scattered radiation from the sample is the FReLoN camera [72], developed by the 'Analog and Transient Electronic' ESRF group (Jean-Claude Labiche). The principle of the two-dimensional detector is a thin scintillator plate of $40\mu m$ thickness made of Gd2O2S : Tb, that is connected to a fibre optic taper. The fibres guide the scintillation light to a 2048 x 2048 pixel ATMEL 7899 chip. To minimize the dark current, the CCD chip is inserted in a vacuum chamber and a Peltier effect thermoelectric cooler maintains its temperature at -20 ℃. This allows one to reduce the dark current to a few electrons/pixel/s and allows exposures of up to a few seconds without significant excess dark noise. A thermal sensing resistance attached to the cooling block of the detector monitors its temperature. A regulated water-cooling heat exchanger removes the heat. The camera is mounted on a horizontal translation stage, that allows to vary the sample-detector distance. At ID09 the camera is equipped with a 1.6 mm thick tungsten beamstop, that is directly mounted on the beryllium entrance window to provide additional protection from the primary beam. All detectors require various corrections to convert the measured pixel intensities into absolute differential scattering cross-sections. Online data reduction routines are available to make absolute intensities available immediately during the experiment (CORIMG [73]). They include the correction of detector artifacts such as dark current, image distortion and spatial inhomogeneities, as well

as normalization of intensities to incident photon flux, sample transmission and spherical angle. Before performing any experiment the correct sample-detector distance is calibrated using the diffraction pattern from Al_2O_3 powder in a spinning capillary.

2.2.8 The pump: laser source

For the experiments reported in this thesis two laser source have been used to photoexcite the sample. The first laser source is a tunable laser (Vibrant, Opotek). It is constituted by a Q-switched Nd:YAG laser, which emits photons at 1064 nm wavelength, in pulses of 3 ns temporal halfwidth. A flash-lamp which pumps the laser media operating at a constant frequency controls the emission process. An electro-optical switch controls the emission of the laser by changing quickly the quality factor of the cavity and allowing the emission of the energy stored inside the crystal. The interested reader can find further details about the process of generation of the laser pulses with the use of cavity quality factor switching in the specific bibliography [75] [76] [77]. The repetition rate of the Q-switching process can be varied from 1 to 10 Hz matching always the incoming rate of the X-ray pulsed probe. In figure 2.17 is reported the diagram of our laser source. The photons emitted by the ND:YAG laser (labeled with number 1 in figure) are guided by two mirrors towards two different non-linear crystals: the first one (2) generates the second harmonic signal (532 nm) and the second crystal (3) produces the third harmonic obtaining photons of 355 nm wavelength. These nonlinear conversion processes depend critically on the relative orientation of the polarization axis of the incident beam with respect to the crystals axis. The process is highly efficient only when the condition of phase matching is ensured, that is when the phase velocities of the frequency-doubled and the fundamental waves are the same. To this purpose two different knobs allow to finely vary the crystal axes orientation thus tuning the non-linear conversion process and obtaining the maximum output power. The laser beam reaches another non-linear optical device (4), named Optical Parametric Oscillator (OPO). This passive device can convert a single input laser beam of frequency νp in two beams, named Signal and Idler, having lower frequencies νs and νi respectively, linked to the pump frequency νp by the relation $\nu p = \nu s + \nu i$ This conversion process takes place in a beta barium borate (BBO) crystal and requires phase-matching condition too; it is obtained with a fine tuning of the axis of the non-linear birefringent BBO via software controlling. The spectral bandwidth of the output beam varies slightly with the wavelength but it remains below 0.3 nm. Finally, we used this laser source at a constant wavelength of 532 nm (maximum energy density of $10 mJ/cm^2$ per pulse).

But the final energy density after focusing at the sample position was usually $2-2.5 mJ/mm^2$. All energy densities were measured with a pyroelectric detector inserted in the laser line before each experiments. The second laser system used during this work of thesis is the high energy laser DM50 (Photonics Industries diode pumped Nd:YLF Q-switched, 527 nm). It is normally used as a pump laser in more sophisticated laser systems. Nevertheless, because of its long pulse duration (200 ns), it has been used for specific purposes (see cap.3) attenuating its energy with filters and a polarizer.

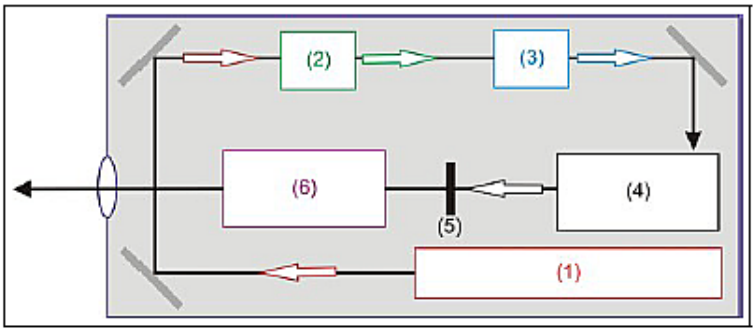

Figure 2.17: Schematic representation of the tunable laser Opotek: (1) ND:YAG laser (1064 nm), (2) non-linear crystal for second harmonic generation (532 nm), (3) non-linear crystal for third harmonic generation (355 nm), (4) optical parametric oscillator, (5) polarizer, (6) UV module.

2.2.9 Synchronization and time delay tuning

The overlap between the x-ray and laser pulses and their timing is clearly a crucial point of the beamline. The spatial profile matching of the two spots is achieved by a $20\mu m$ pinhole mounted in the axis of rotation of the goniometer which will keep the sample during the measurement. The pinhole is then aligned on the X-rays looking at the transmission profile and then rotated of the incidence angle of the laser at the end of the optics line (which also determines the focus size). A very sophisticated electronics controls the synchronisation (N354 electronic card [73]). The basic idea is to use the frequency given by the bunch clock of the synchrotron ring, 352kHz and to split and electronically multiply or divide this signal to send it as input signal for the other instruments. The frequency of the choppers is matched to a sub-frequency (360th) of the fundamental. Then a phase reference derived directly from the synchrotron first bunch (RF signal) is used to set the phase of choppers to make them open at the right time to select one single pulse.

The N354 electronic card is able to send a sub-frequency (1-10 Hz range) to trigger the laser source, the millisecond shutter and start the detector integration. Before starting an experiment the synchronization of laser and X-ray pulses is checked. The synchronization of the two pulses is obtained thanks to a fast detector sensible to both kinds of radiation. It consists of a highly irradiated GaAs photoconductor that is operated with a bias voltage. It has a rising time of 20 ps and its signal is recorded by a fast sampling oscilloscope (Tektronix). Figure 2.18 shows the appearance of two pulses in a typical oscilloscope image. Moving the time delay of the laser pulse it is possible to fix the time zero when the x-ray pulse is at the center of laser pulse. To change X-ray/laser pulses delay during the data collection then it is sufficient to shift (by N354 electronic card) the laser trigger.

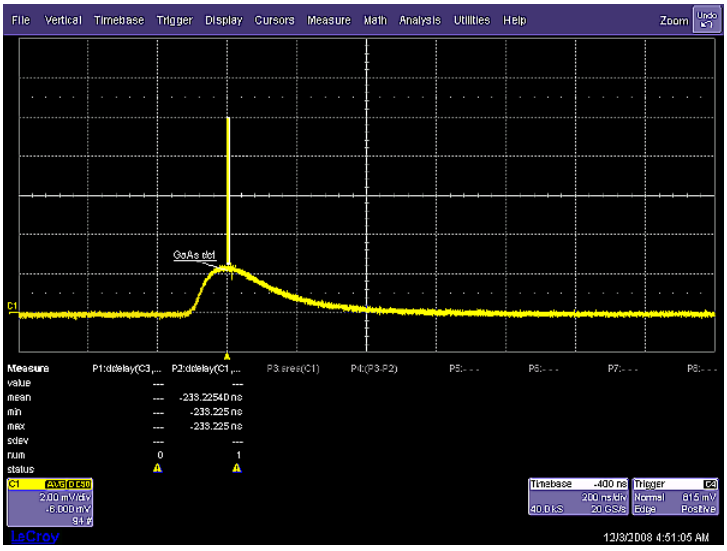

Figure 2.18: Screen-shot of a typical oscilloscope image: the small pulse represents the incoming X-ray pulse of 100 ps duration while the broad pulse corresponds to the laser pulse (200 ns in this case). The signal recorded comes from a GAs fast detector sensible to both kinds of radiation.

2.2.10 Data collection strategy

The sample is sealed in a quartz capillary or in a mylar sample holder that can be translated in a direction perpendicular to that of incoming X-ray beam in order to reduce the radiation damage. Triplets of images are collected for each time delay. Indeed the data are collected in units of laser off/laser on/laser off triplets (i.e. a scattering pattern from the nonexcited system, a scattering

pattern from the system after a given time delay and a second non-excited). The two laser off patterns are averaged to minimize the effect of slow drifts in beam position, and this is done in angular space after radially integrating the 2D images using the Corimg software [73]. Then the laser off average is subtracted from the laser on signal at every time delay which gives the difference scattering pattern $\Delta S(q)$. These difference maps contains all the information about the structural changes occurring in the sample and triggered by the laser. From the snapshots taken as time goes by the evolution of the system can be followed. It is possible to convert the scattering angle in the magnitude of the scattering vector q using the equation: $q = 4\pi sen(\theta/2)/\lambda$, where λ represents the X-ray average wavelength. Scattering patterns I(q) are recorded at different time-delays between the trigger signal (in our case a laser pulse to induce ligand photolysis of carboxy-hemoglobin (HbCO) and the X-ray pulse probing protein structural changes. Figure 2.19 shows a typical I(q) pattern scattered by a HbCO buffered solution loaded in a quartz capillary (blue curve). While the protein features are added to a flat background at $q < 1$ $\mathring{A}^{-1}$, the contributions of the buffer solution (water), of the capillary (quartz), and of other materials that X-rays cross before reaching the CCD detector (air, mylar, and beryllium) dominate the scattering pattern at $q > 1.5$ $\mathring{A}^{-1}$. To compensate for differences in the incident X-ray flux (which is not constant during an experiment), I(q) patterns should be properly scaled. Unfortunately, ID09B is not equipped with a monitor of the incident X-ray flux sufficiently accurate for these applications. Thus, we have chosen to normalize all the I(q) patterns at a given q-value. We typically use the 2-2.2 $\mathring{A}^{-1}$ region to normalized the I(q) patterns since in this q-range: 1) the protein signal is very small (we don't expect variations related to conformational changes of protein structure); 2) the solvent scattering is independent on temperature (we don't expect variations related to the energy transfer from the photolysis laser into the solvent via protein absorption) [17]. As a final step, in order to obtain a signal related to the structural changes occurring in the sample after photolysis, scattering difference patterns are calculated by subtracting the normalized I(q) pattern measured before photolysis from every normalized I(q) pattern measured after photolysis. This approach allows to subtract the parasitic scattering from air, from the capillary or the sample cell (used in RBC experiment), to subtract the contribution of Compton scattering and to compensate for systematic errors like the background of the detector. Note that the effect of the normalization procedure has to be taken into account when comparing TR-WAXS data of different samples. Differences in protein concentration are not compensated because, as already noted, the protein contribution to the scattering curve in the 2-2.2 $\mathring{A}^{-1}$ range is very small; this implies that normalized I(q) patterns

(or scattering difference patterns) obtained from samples with different protein concentrations have to be properly scaled (for the ratio of the protein concentrations) before they can be directly compared.

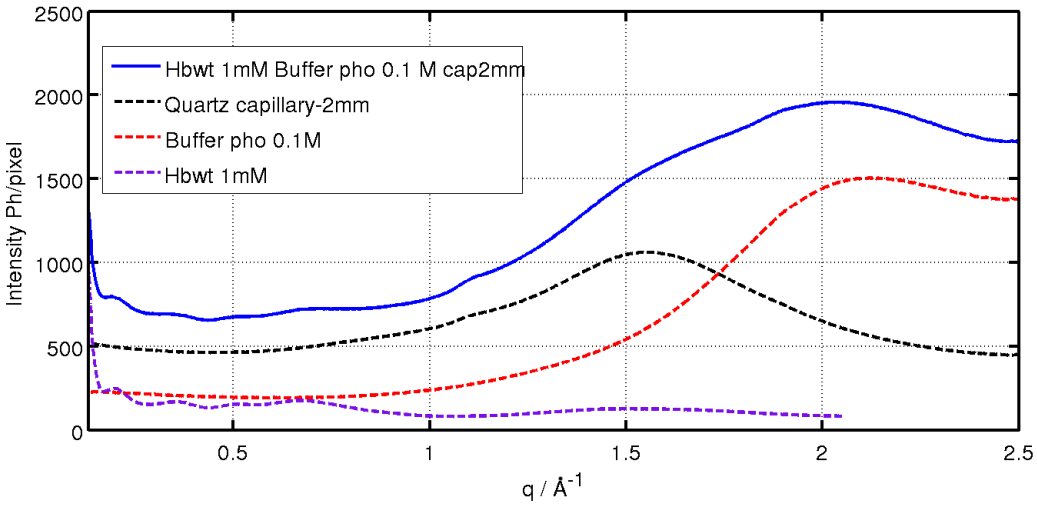

Figure 2.19: : Different contributions to a typical I(q) static pattern (before normalization) scattered by a solution of HbA (1 mM in tetramer, 0.1 M phosphate buffer at pH 7) contained in a quartz cylindrical capillary (2 mm diameter, 10 μm wall thickness). The experimental pattern recorded in SC2676 experiment (blue curve) is compared with the pattern of an empty capillary (black dashed curve), which arises from the scattering of quartz, air, mylar, etc. The buffer contribution (red dashed curve) has been obtained as the difference between the scattering pattern of the capillary filled with buffer and that of the empty capillary. The protein contribution (magenta dashed curve), which can be derived from the experimental patterns cited above, presents several characteristic peaks below 1 $\mathring{A}^{-1}$ (recognizable also in the experimental pattern) and becomes flatter at higher q-values.

Chapter 3

TR-WAXS on HbA and HbYQ mutants

Time-resolved wide-angle X-ray scattering (TR-WAXS) allows to track quaternary conformational changes induced by laser photolysis on native HbCO. From now on the native human hemoglobin will be referred as HbA. As reported in the introduction the TR-WAXS experiments on HbA quaternary transition revealed that a global structural relaxation compatible with the relative rotation of the dimers occurs at ~ 2 μs [Cammarata et al. 2008 and 2010 [17, 25]]. In the experiments reported in this chapter (Experimental report SC2676 [78]), at difference with previous experiments where a 200 ns long photolysis pulse was used to significantly reduce geminate rebinding, we decided to use a shorter laser pulse (3 ns FWHM) both to investigate early events after photolysis and to increase the population of the R1 state (singly bounded R-state Hb); indeed, using a 3 ns photolysis pulse, the R1 state is expected to be significantly populated immediately after photolysis and the dimers rotation kinetics is expected to be dominated by the R1-T1 transition rate. We have also investigated in the same experimental conditions (i.e. with ns laser excitation) Hb mutants containing the Leu B10 $\rightarrow$ Tyr, and His E7 $\rightarrow$ Gln mutations in the distal side of heme pocket. Such Hb mutants bind cooperatively ligands such O_2, CO, and NO, although with lower affinity [95]. Moreover, the mutations are able to substantially modify the extent of geminate rebinding [96]. Geminate recombination occurring after photolysis in native hemoglobin is attributed to the rebinding of the photodissociated ligand still trapped in the distal pocket (while bimolecular rebinding is attributed to the ligand diffusing inside the protein from the bulk).

TR-WAXS measurements have been performed on Hb samples with mutations in both α and β chains (Hb$\alpha\beta$YQ), α chains only (HbαYQ), or β chains

only (HbβYQ). By comparing TR-WAXS data of different samples it is possible to investigate the dependence of Hb structural dynamics on strategic point mutations in the active site.
A brief introduction to this class of Hb mutants is given in the next section emphasizing their specific features and their possible applications in biomedical field.

3.1 YQ mutants of Hemoglobin

The main function of heme-proteins such as hemoglobin (Hb) and myoglobin (Mb) in vertebrates is the binding and transport of gaseous ligands as O_2. In the active site (usually referred as the heme pocket) the prosthetic heme group is bound to the protein matrix by an His residue in position F8 on the proximal side of the heme. Different amino-acid residues on the distal side of heme are expected to interact with ligands bound to the heme via steric electrostatic or hydrogen bonds interactions, playing then a role in the ligand binding modulation. The analysis of the crystallographic structure of hemoglobin and myoglobin and experimental evidences obtained by protein engineering methods revealed that some amino-acid residues near the heme can play an important role in function and stability modulation [79, 80]. In particular, as revealed by different investigations, the side-chains at topological positions B10 and E7, affect the stabilisation of gaseous ligands, such as CO and O_2 (the interested reader can read the review of Springer et al. reported in the bibliography [81] and references therein).
As an example, in Mb (and in the α chains of HbA) the iron-bound O_2 is stabilized by a H-bond with residue His in position E7 [82, 83, 84]. A Gln residue in the same position (E7) can play the same role, as shown in the case of elephant Mb [85, 86] and by site-directed mutagenesis. Of course a higher number of residue able to form H-bond with O_2 ligand is expected to reduce the dissociation constant rate. For example Travaglini-Allocatelli et al. in 1994 [87] have shown how a simultaneous replacement of residues at positions B10 (Leu $\rightarrow$ Tyr), E7 (His $\rightarrow$ Gln), and E10 (Thr $\rightarrow$ Arg) affects O_2 stabilisation in sperm whale Mb. In fact the mutant Mb-YQR displays a reduced O_2 dissociation rate constant ($k = 1s^{-1}$ at pH 7.0 and 20 ℃) as compared to native sperm whale Mb ($k = 14s^{-1}$). The autoxidation rate is reduced threefold while the P50 for O_2 of Mb-YQR is unchanged. As reported by the authors the analysis of 3D structure of Mb-YQR revealed the formation of two H-bonds with the iron-bound ligand and suggested the presence of a steric hindrance to ligand diffusion as demonstrated by stopped and flow and laser photolysis experiments ([88, 89]).

These functional modifications were transferred to human Hb to test their use for interesting variants for the synthesis of possible blood substitutes, which first of all should yield an O_2 adduct stable to autoxidation and slowly reacting with NO ([90, 91, 92]). A blood substitute is a substance used to mimic and fulfill some functions of biological blood, usually in the oxygen-carrying sense, to provide an alternative to blood transfusion. It is well known that unmodified cell-free haemoglobin can not be used for this purpose because several limitations, such as: an oxygen affinity that is too high for effective tissue oxygenation; a tendency to undergo dissociation in dimers with resultant renal tubular damage and toxicity, and affinity for nitric oxide (abdominal pain, vasoconstrictive crises)[93, 94]. One of the possible approach is to modify haemoglobin artificially via recombinant technology. In particular Miele et al. in 1999 reported the characterisation of three new mutant human Hbs carrying two substitutions (namely Leu B10 $\rightarrow$ Tyr, and His E7 $\rightarrow$ Gln) in the distal pocket of either the α or the β-chains or both [95].
The crystallographic structure of deoxy-Hb$\alpha\beta$YQ determined by crystallography at 1.8 $\mathring{A}$ resolution was presented by the authors showing that structural differences in respect with the T form of HbA are mainly located at heme pocket level as shown by figure 3.1. These mutants display remarkable functional properties which (to a first approximation) seem to be interpretable within a two-state allosteric model [14]. The Hb carrying the two substitutions on both chains is less reactive towards ligands (CO, NO, O_2) compared to HbA, while its autoxidation rate is unchanged. Time resolved absorption measurements performed with the technique of the flash photolysis demonstrated that geminate rebinding is mainly suppressed in Hb$\alpha\beta$YQ and partially suppressed in HbαYQ and HbβYQ [96].

Hemoglobin	Hill coefficient	p50 mmHg	K_R mmHg	K_T mmHg
HbA	2.9	7.1	0.2	26.7
HbαYQ	2.1	2.6	0.5	57
HbβYQ	1.5	4	0.8	47
Hb$\alpha\beta$YQ	1.8	49	1.2	77

Table 3.1: Parameters for O_2 and CO binding to HbA and B10 & E7 mutant hemoglobins. Values from Miele et al. 1999 [95].

From this brief introduction it is evident that a comparison of tertiary and quaternary dynamics between HbA and mutants Hb$\alpha\beta$YQ, HbαYQ as well as HbβYQ can give new insights on the properties of these systems. TR-WAXS it is the most suitable technique for this purpose allowing to clarify

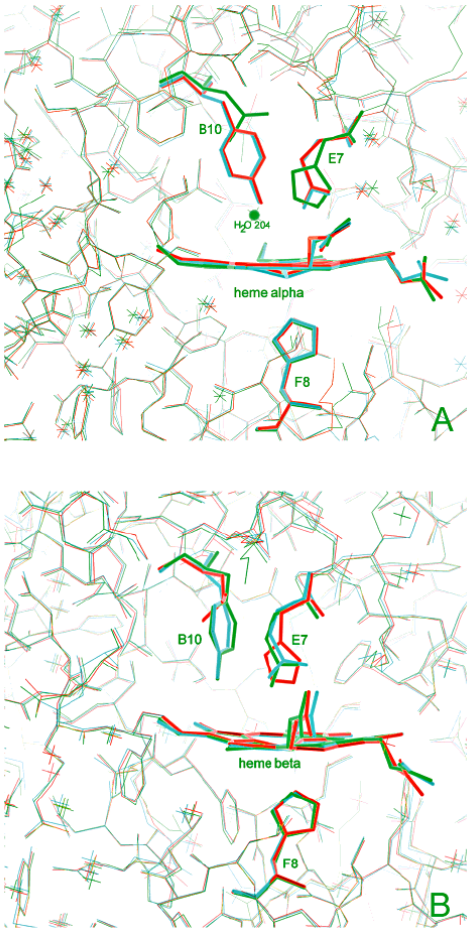

Figure 3.1: The figure shows the superposition of the deoxygenated structures of HbβYQ (green), HbαYQ (red) and Hb$\alpha\beta$YQ (blue). Residues B10, E7, F8, and the heme are presented in stick; the water molecule found in the pocket of native Hb α chain of HbβYQ is drawn as a ball. Panel A depicts α chains and panel B β chains. The figure is taken from Miele et al. 2001 [96]

the possible consequences of point site mutations at the heme pocket level on the global structural kinetics of Hb.

3.2 Hemoglobin structural dynamics probed by TR-WAXS

In this section the results obtained on native Hb and Hb mutants are presented together with an extensive explanation on the data analysis strategy.

Experimental conditions and sample preparation

HbA was purified from freshly collected human blood with standard techniques. The HbA samples used for the TR-WAXS experiments were prepared as described by Cammarata et al. 2010 [25]: erythrocytes from freshly drawn heparinized human blood were washed four or five times with 0.9% NaCl and then hemolyzed with pure peroxide-free ethyl ether. The stroma was precipitated with NaCl (10% by weight) and removed by centrifugation. The hemolysate was dialyzed overnight against 0.1 M potassium phosphate buffer (pH 7) and then stripped of organic phosphates by passage through a Sephadex G-25 (fine) column equilibrated with 0.1 M potassium phosphate. All steps were carried out at 4 ℃. The resulting Hb solution had a typical concentration of $\sim$ 12% wt/vol. Stock solutions were stored as beads in liquid nitrogen with the protein in oxygenated form.
All experiments were carried out in 0.1 M potassium phosphate buffer at pH 7 and room temperature. Organic phosphates that strongly affect the R-T equilibrium, such as 1,2-diphosphoglycerate, were stripped from Hb molecules. All reagents were of analytical grade.
Hb samples to be used for TR-WAXS experiments were equilibrated for approximately 20 min. with humidified CO. A small amount of a CO-saturated Na-dithionite solution was added anaerobically to ensure full reduction of the iron. The final Na-dithionite concentration was 8 mM in all samples. The HbA samples were 4 mM (in heme), i.e. 1.0 mM in tetramer. Approximately 100 μl of a freshly prepared CO-saturated Hb solution were loaded in a 2 mm diameter quartz capillary (Hilgenberg GmbH). Two CO bubbles were trapped on both sides of the protein solution volume. A CO-saturated glycerol drop prevented gas leakage at the open side of the capillary. All capillaries were further sealed with capillary wax (Hampton Research) and nail varnish.
The same protocol for sample preparation was used on Hb$\alpha\beta$YQ HbαYQ and HbβYQ samples. The site-directed mutants were expressed in Escherichia

coli and purified as CO derivatives (Vallone et al. 1993 [97]). The final concentration of the Hb mutants samples was: 0.50 mM for Hb$\alpha\beta$YQ, 0.55 mM for HbαYQ and 1.0 mM for HbβYQ (in tetramer).

TR-WAXS patterns were acquired at the ID09B beamline of the Euro-

Sample	C / mM	pH	time delays/decade	range
HbA	1.0 mM	7.0	6	3 ns - 100 ms
HbαYQ	0.55 mM	7.4	2	3 ns - 10 ms
HbβYQ	1.0 mM	7.4	2	3 ns - 10 ms
Hb$\alpha\beta$YQ	0.5 mM	7.4	4	3 ns - 300 ms

Table 3.2: Samples used for TR-WAXS measurements. Laser pulse 3 ns at 532 nm and energy density at the sample position of $2.5 mJ/mm^2$
. All samples were prepared in 0.1 M K-pho buffer.

pean Synchrotron Radiation Facility (Grenoble, France) while the machine was running in four-bunch mode. HbCO samples were photolyzed with 3 ns long (full width at half maximum) circularly polarized laser pulses at 532 nm (the circular polarization minimizes the phenomenon of photo-selection being the HbCO absorption band in the 400-600 nm mainly polarized along the z direction perpendicular to the heme plane). Laser pulses incident on the bottom surface of the capillary were spatially superimposed with delayed quasi-monochromatic X-ray pulses in the orthogonal direction (x) (100 ps, full width at half maximum) extracted from the synchrotron. X-ray pulses penetrated the capillary 0.2 mm above its bottom edge so that an orthogonal geometry between X-ray and photolysis pulses was realized. In order to optimize the laser X-ray superposition the laser beam was shaped to give an elliptical spot size at the sample position of about 200μm along the direction perpendicular to X-ray (y) and 1 mm along the X-ray direction (x). The photolysis energy density at the capillary surface was approximately $2.5 mJ/mm^2$. X-ray scattering patterns were acquired between 3 ns and 0.1 s (at many time delays per decade). To dilute any X-ray radiation damage over a large sample volume, the capillary was translated back and forth along its long axis over a 25 mm range, ensuring that each laser pulse excited adjacent but spatially separated samples volumes according to the laser beam shaping.

Scattered X-ray were recorded in the forward direction by a sensitive CCD Frelon camera [72]. Each image was azimuthally averaged and converted into a one-dimensional q-curve using a wavelength of 0.6896 $\mathring{A}$ corresponding to the peak of the X-ray spectrum from undulator U17 at 9 mm gap. After normalization (in the 2-2.2 $\mathring{A}^{-1}$ q-region), a reference scattering pattern

(laser-off image), which probed the unexcited sample, was subtracted from the scattering pattern at a given time delay. Difference patterns obtained at the same time delay were averaged ($\sim$ 30 averages per time delay).

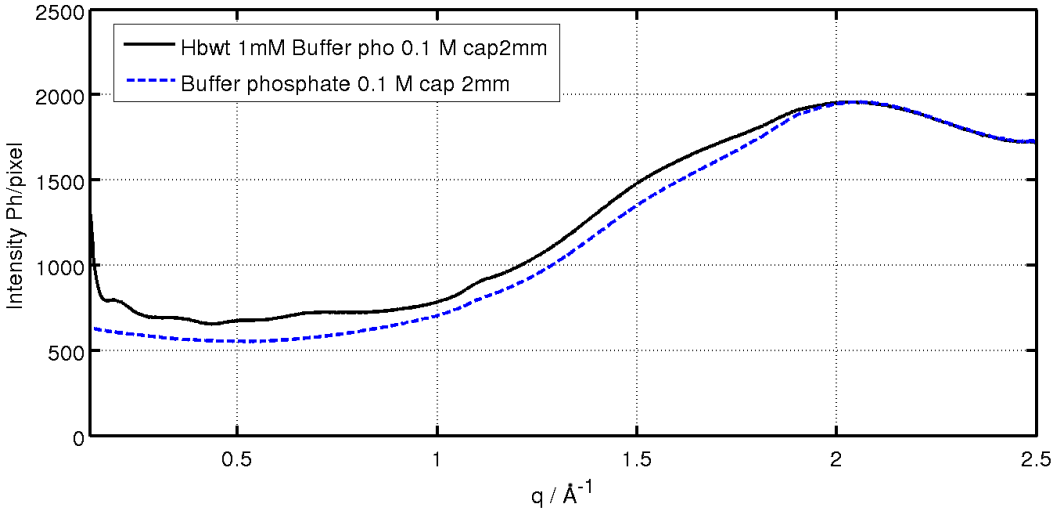

Figure 3.2: Scattering pattern of a 1 mM HbCO solution contained in a quartz capillary having a diameter of 2 mm, together with the scattering pattern of an identical quartz capillary filled with buffer.

TR-WAXS data on HbA

Figure 3.2 shows the scattering pattern of a 1 mM HbCO solution (0.1 M potassium phosphate buffer, pH 7) contained in a 2mm quartz capillary, together with the scattering pattern obtained from an analogous capillary filled with the same solvent. The protein contribution to the scattering pattern below 0.1 $\mathring{A}^{-1}$ lacks information on structural details and is essentially related only to the protein average linear dimension. At higher q values, the pattern is more structured arising from the correlations among the protein structural motifs (q $\leq$ 1.5 $\mathring{A}^{-1}$). The scattering of water dominates at higher q values ($\sim$ 2 $\mathring{A}^{-1}$). In TR-WAXS experiments, the scattering pattern measured before photo-excitation is always subtracted from the pattern measured at a given time delay after the laser pulse. In this way, the laser-induced signal is isolated from any non laser dependent component of the signal. Figure 3.4 reports TR-WAXS difference patterns measured at several time delays after photolysis of a 1 mM HbCO solution at room temperature containing 0.1 M phosphate buffer at pH 7. In the q-region where the protein signal dominates

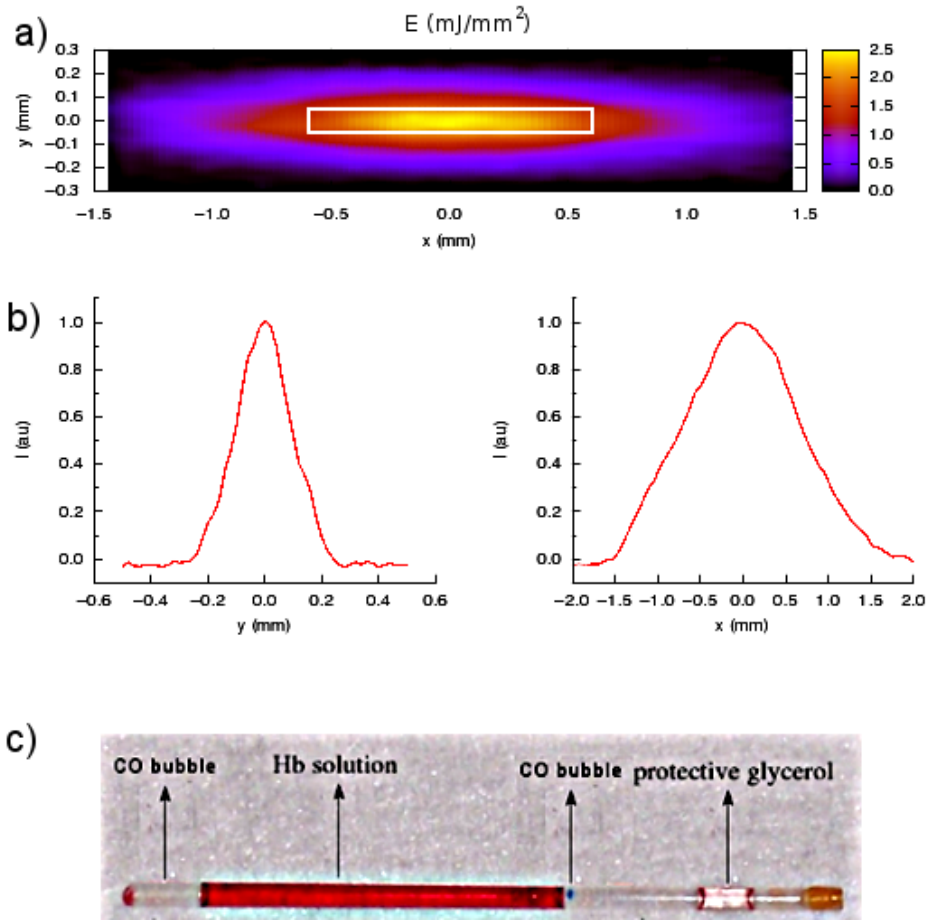

Figure 3.3: The beam shape at the focus was elliptical. Panel a) energy density at the sample position: spatial profile of the laser beam and energy density (mJ/mm2) at the sample surface; the white rectangle represents the X-ray probed region. Panel b): normalized cuts along the x and y directions. Panel c): typical sample loaded into the capillary used during TR-WAXS experiments.

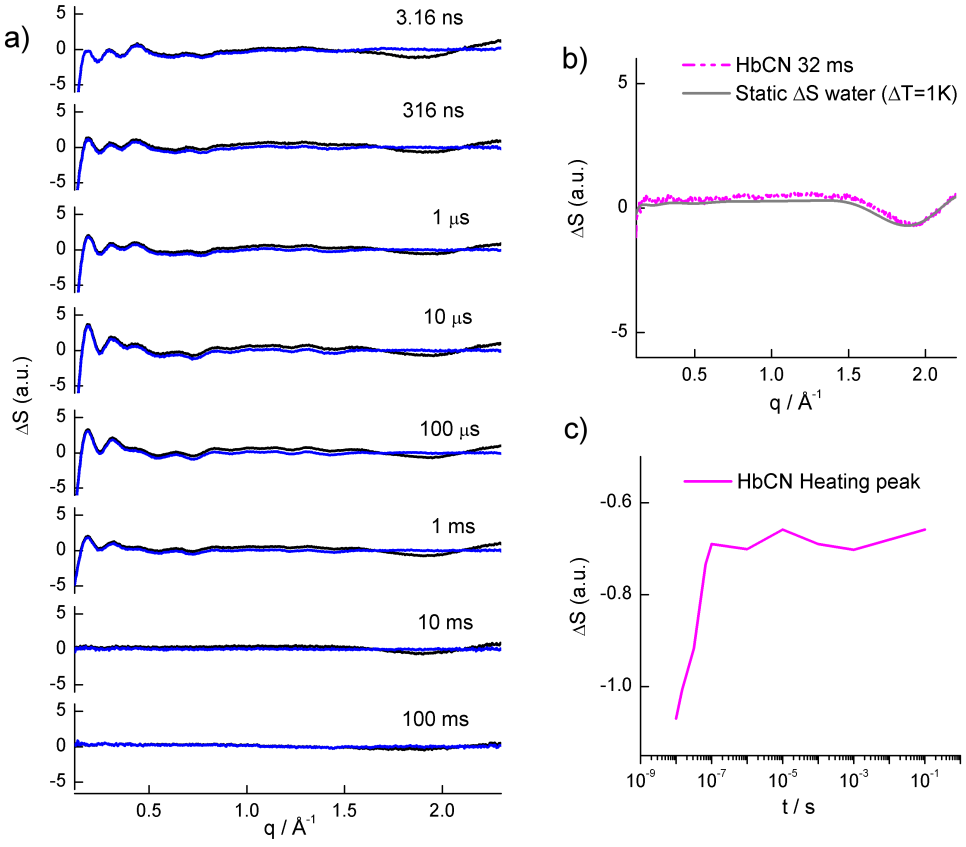

Figure 3.4: Panel a) Raw data acquired on HbA are reported as black curves, while the data after heating subtraction are shown as blue curves. Panel b) Typical heating signal measured on HbCN sample compared with the difference in WAXS patterns recorded on a water sample before and after a 1K heating obtained with a simple Peltier system (water scattering patterns are taken from M. Cammarata unpublished data). Panel c) Temporal dependence of the heating negative peak:ΔT is constant up to time delays of 10 ms when heat diffusion starts to cool down the excited region.

($q \leq 1.5\ \mathring{A}^{-1}$), the time evolution of these difference patterns indicates that the structure of Hb molecules probed by the X-rays changes as a function of time. Liquid water molecules have an average distance of about 3 $\mathring{A}$, giving rise to the peak at 2 $\mathring{A}^{-1}$ in the scattering pattern (Figure 3.2). Small changes in temperature (due to the laser energy absorbed by the protein and released to the solvent) slightly modify water distance distributions that in turn modify scattering around the water peak; this is the origin of the difference signal (heating signal) that contributes mainly to the 1.5-2.5 $\mathring{A}^{-1}$ q-region, as previously shown by Cammarata et al. [17]. TR-WAXS patterns have been collected at 35 different time delays between 3 ns and 100 ms and in figure 3.4 data after the heating contribution subtraction are shown.
To decouple the structural and the heating contributions, we have collected TR-WAXS data on cyanomet-hemoglobin (HbCN) in the same experimental conditions used for the other samples (0.5 mM in tetramer, 0.1 M phosphate buffer pH 7). HbCN has a molar extinction coefficient at 532 nm close to that of HbCO, whereas the bond between the CN- ion and the iron atom cannot be photolyzed. As the sample is photoexcited by the laser pulse, the delivered energy does not induce any conformational change on the protein. All the energy is delivered to the solvent inducing a temporary heating of the solution (associated to a structural rearrangement of the solvent molecules). Scattering difference patterns of a HbCN sample are thus a measure of the solvent heating contribution. In order to isolate the protein contribution in the TR-WAXS difference patterns, we have subtracted from the pattern measured at a given time-delay the pattern of the HbCN sample at the same time-delay (scaled for a factor taking into account possible differences in concentration). Figure 3.4 reports the result of such subtraction at some representative time-delays as blue curves.
Looking at the heating subtracted data it is possible to give a general description of what is happening to the HbA molecules after photolysis.

At 3 ns an intermediate in R-T transition is already detectable. The difference pattern measured at 3 ns after photolysis arises from the differences, mainly at the tertiary structural level, between the Hb transient structure (Hb^{**}) and the HbCO equilibrium structure.
The shape of difference patterns changes gradually to the 316 ns signal arising from the so called "clamshell motion" (Kachalova et al 1999 and Guallar et al. 2006 [99, 98]) as suggested by Cammarata et al. [17] (figure 3.5). Analyzing the crystal structures of myoglobin in the deoxy- and carbon monoxide-ligated states at a resolution of 1.15 $\mathring{A}$ Kachalova et al. in 1999 [98] pointed out that carbon monoxide binding requires concerted motions of the heme, the iron, and helices E and F for relief of steric inhibition. In view of the similarity of the active site of myoglobin and hemoglobin, Balakrishnan et al.

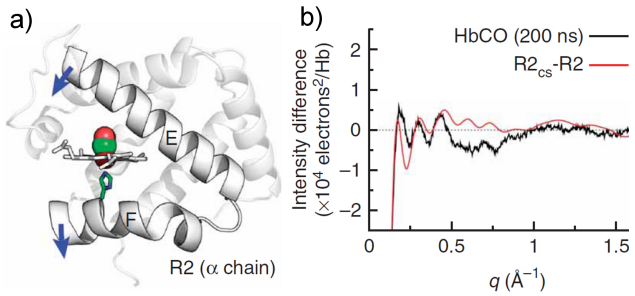

Figure 3.5: Snapshot of the CO-bound alpha subunit. The E and F helices form the "clamshell" that holds the heme in place. The blue arrows indicate the direction of the E and F motion during the "clamshell relaxation". Panel b) Comparison of the 200 ns time-resolved data with the difference pattern calculated from the R2 crystal structure and its modified unligated version mimicking the effect of the clamshell relaxation. The figure is taken from [17].

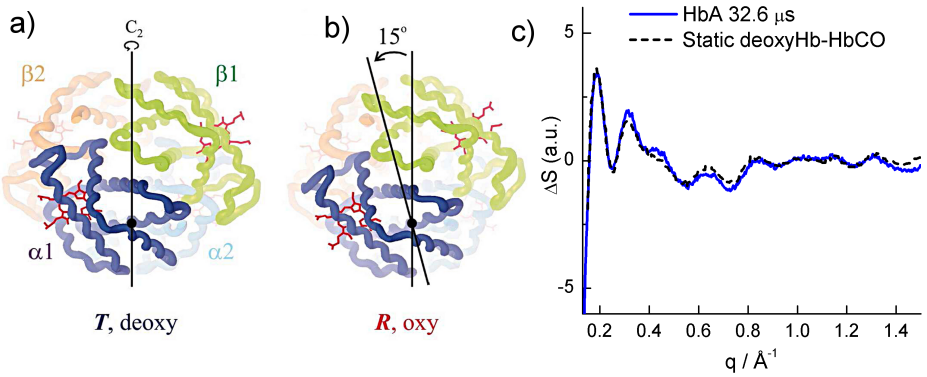

Figure 3.6: The solvent response-subtracted time resolved data at 32.6 μs after photolysis compared with the static equilibrium scattering difference between a deoxyHb equilibrium sample and an HbCO sample (static scattering difference are taken from Cammarata et al. 2008 [17]).

in 2004 [57] assigned the relaxation process revealed in carboxy-hemoglobin in the 100 ns range by the use of transient absorption and resonance Raman (RR) spectroscopy to the E-F helices "clamshell" motion. In 2006 V. Guallar et al. [99], combining quantum and molecular mechanics (QM/MM) methods and protein structure prediction algorithms, have shown how the principal effect of CO dissociation from myoglobin is a concerted rotation of the E and F helices, which hold the heme like a clamshell. As nonbonded contacts on the distal side are relieved, the F helix moves away from the heme because of the Fe spin conversion while the E helix collapses toward the heme.
Between 1 μs and 10 μs, the TR-WAXS signal changes in shape and grows in intensity. It is possible to demonstrate that Hb molecules undergo the R-T transition (tertiary and quaternary structural changes) in this timescale by comparing the 32 μs TR-WAXS pattern with the difference between the deoxygenated Hb (deoxyHb) static pattern and the HbCO static pattern [17]. At longer time delays quaternary transition dominates the scattering patterns difference as shown in figure 3.6. At 10 ms the Hb has already rebound CO (bimolecular rebinding) coming back to the initial HbCO configuration (R_4) and as a consequence the difference patterns tend to zero.

3.3 TR-WAXS data on HbYQ mutants

In this section TR-WAXS data obtained on HbA sample are compared with TR-WAXS data obtained on Hb$\alpha\beta$YQ mutant in the same experimental conditions.

Figure 3.7 reports a comparison of HbA and Hb$\alpha\beta$YQ difference patterns (after heating subtraction) at representative time-delays from photolysis. To compensate for the different protein concentration (0.5 mM as opposed to 1 mM) the Hb$\alpha\beta$YQ patterns have been multiplied by a factor two. Figure 3.7 shows that the overall shape of the Hb$\alpha\beta$YQ difference patterns is analogous to that of HbA, indicating that the structural intermediates involved in the R-T transition are similar in the two samples. Nevertheless, differences in both the amplitude and time evolution of the patterns is evident. TR-WAXS patterns measured at 3.16 ns from photolysis are expected to reflect tertiary structural changes and to be proportional to the number of deoxy-hemes in the scattering volume. TR-WAXS patterns measured 100 μs after photolysis are essentially due to the dimers rotation and are thus proportional to the number of Hb molecules that undergo the R-T transition. Finally, at time-delays as long as 100 ms, only bimolecular rebinding is expected to take place, causing a reduction of the TR-WAXS signal am-

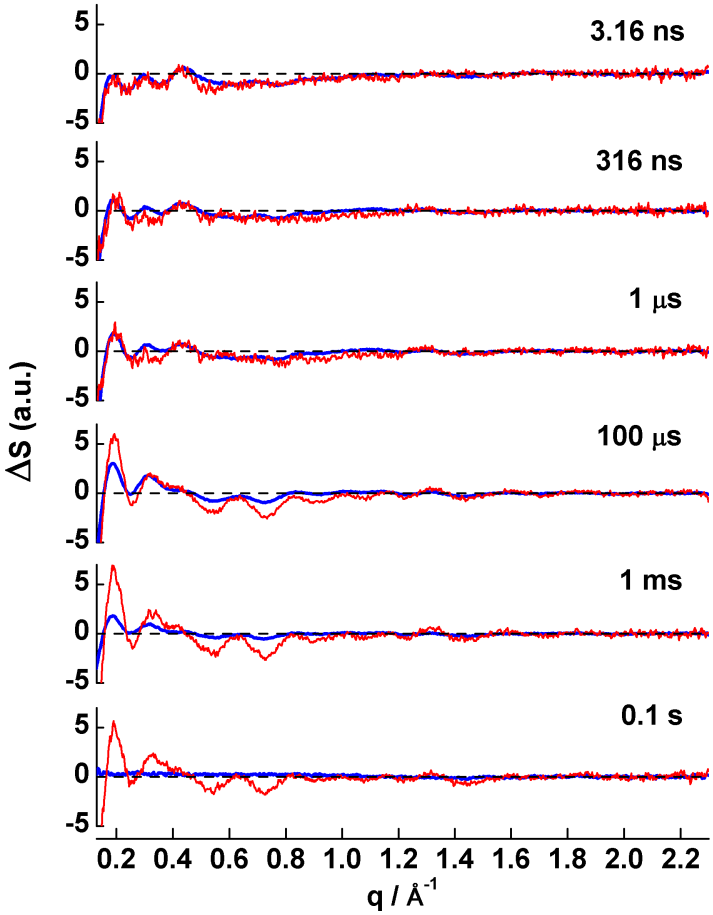

Figure 3.7: TR-WAXS difference patterns of HbA (blue curves) and Hb$\alpha\beta$YQ (red curves) at representative time delays from a 3 ns long photolysis pulse. A fast local (tertiary) structural change is detected at 3.16 ns in both HbA and Hb$\alpha\beta$YQ (first panel from top). At 100 μs the typical pattern associated to quaternary transition (Cammarata et al., 2008 [17]) is observed, its amplitude is larger for Hb$\alpha\beta$YQ than for HbA due to the large difference in the extent of geminate rebinding. At 100 ms, while HbA molecules have already rebound all their CO ligands, the Hb$\alpha\beta$YQ mutant is mostly in the deoxy form due to the small bimolecular rebinding rate of CO to Hb$\alpha\beta$YQ [Miele et al., 2001 [96]].

plitude without any significant change in shape. It is evident that, while at 3.16 ns the TR-WAXS patterns are very similar, both in amplitude and in shape, the 100 μs HbA signal is significantly smaller than the corresponding Hb$\alpha\beta$YQ one. This result is in good agreement with time-resolved optical spectroscopy data showing that geminate rebinding is essentially absent in Hb$\alpha\beta$YQ [Miele et al., 2001 [96]]; indeed, since 45% of hemes rebind CO geminately in HbA (using ns laser photolysis), the number of tetramers undergoing the R-T transition is expected to be significantly smaller in HbA with respect to Hb$\alpha\beta$YQ. At 100 ms, the HbA difference pattern is zero within the experimental error, while the Hb$\alpha\beta$YQ signal is slightly smaller than the one measured at 100 μs. This also agrees with previous data [Miele et al., 2001 [96]] showing that the bimolecular rebinding rate to Hb$\alpha\beta$YQ is much smaller than that to HbA.

Effect of point mutations on different Hb subunits

In the case of HbαYQ and HbβYQ samples, TR-WAXS difference patterns have been acquired between 10 ns and 10 ms from photolysis at 2 time-delays per decade. Difference patterns of HbαYQ and HbβYQ are similar to the Hb$\alpha\beta$YQ ones both at 10 ns and 100 μs (figure 3.8). Small differences in amplitude are observed at 100 μs (the significance of these difference will be commented on below). At 10 ms, the Hb$\alpha\beta$YQ difference pattern is approximately three times bigger than the HbαYQ and HbβYQ ones. This is a result of the slower bimolecular rebinding to Hb$\alpha\beta$YQ with respect to HbαYQ and HbβYQ observed with time-resolved optical spectroscopy [Miele et al., 2001 [96]].

Time course of structural changes observed by TR-WAXS

As reported by Cammarata et al. [25], the peak at $\sim$0.19 $\mathring{A}^{-1}$ in the TR-WAXS difference patterns can be used to monitor the kinetics of the structural changes occurring after photolysis. Figure 3.9 panel a) reports the time evolution of the amplitude of this peak: the signal initially increases due to both tertiary and quaternary structural changes, then reaches a maximum (at time delays that depend on the sample) that is mostly determined by the number of proteins that undergo the R-T transition, and finally decreases to zero due to bimolecular rebinding that brings the Hb molecules back to their initial HbCO structure. Figure 6 suggests that a higher number of Hb molecules undergoing the R-T transition (as judged by the maximum of the peak) and a longer time scale for both the R-T transition and the bimolecular rebinding process are observed for Hb$\alpha\beta$YQ when compared to HbA;

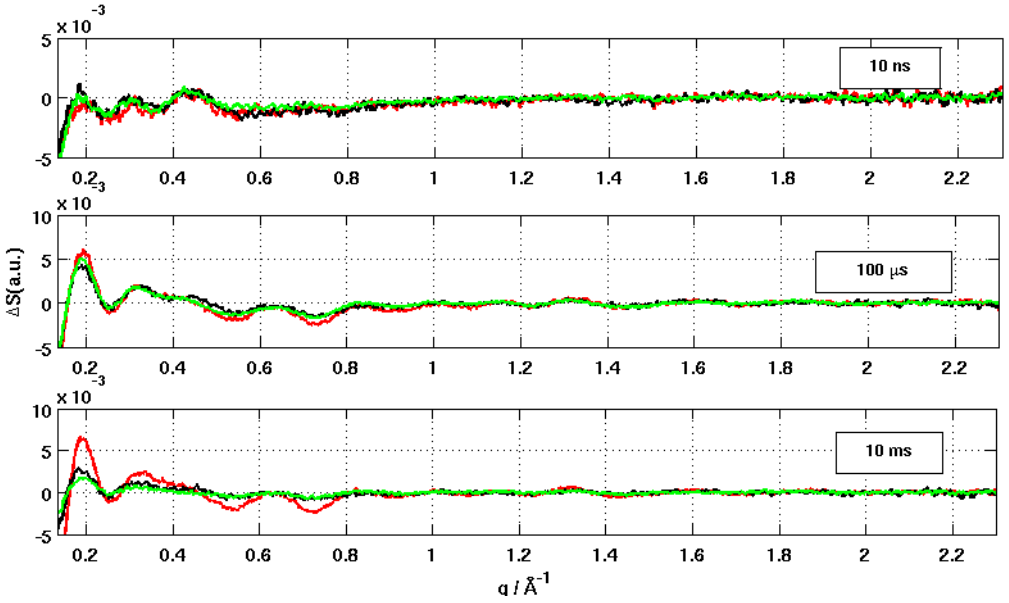

Figure 3.8: TR-WAXS difference patterns of Hb$\alpha\beta$YQ (red curves), HbαYQ (black curves), and HbβYQ (green curves) at representative time-delays.

intermediate values are observed for HbαYQ and HbβYQ as shown in figure 3.10.

It is interesting to compare the maximum value reached by the $\sim$0.19 $\mathring{A}^{-1}$ peak with the apparent yield of geminate rebinding. The latter quantity (as estimated from Miele et al. [96]) is equal to 45%, 30%, and 17% for HbA, HbβYQ, and HbαYQ respectively, and is essentially zero for Hb$\alpha\beta$YQ. The comparison with data in figure 3.9 shows that geminate rebinding reduces the number of Hb molecules performing the R-T transition. However, the relation between the two quantities is not trivial. Indeed, in spite of the difference in the yield of geminate rebinding between HbαYQ and HbβYQ, no significant difference is evident in the maximum reached by the $\sim$0.19 $\mathring{A}^{-1}$ peak. In fact the bimolecular recombination of CO to the Hb molecules in R quaternary state, stabilizing it, it is another factor limiting the number of molecules doing the quaternary transition: in the case of HbαYQ a lower geminate is partially compensated by an higher recombination rate from the R state in respect with HbβYQ [96]. In view of the various physical processes (geminate rebinding, tertiary relaxations, quaternary relaxations, and bimolecular rebinding) underlying the observed signal time evolution, it is not easy to estimate unequivocally the dependence of the R-T transition rate on the amino acids mutations. One of the complications involved is the pres-

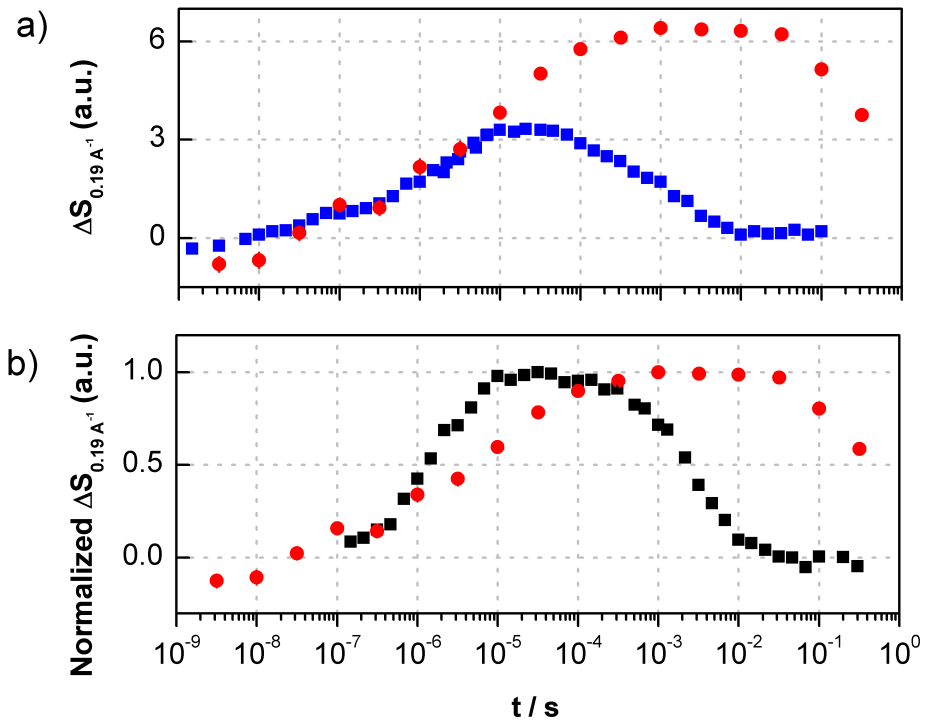

Figure 3.9: a) Time dependence of the amplitude of the 0.19 $\AA^{-1}$ peak for HbA data (blue) and Hb$\alpha\beta$YQ (red). The maximum reached by the different curves is a function of the different number of Hb molecules that undergo the R-T transition. b) Time dependence of the normalized amplitude of the 0.19 $\AA^{-1}$ peak. Hb$\alpha\beta$YQ data obtained with a 3 ns photolysis pulse (red circles) are compared with HbA data obtained with a 200 ns photolysis pulse (black squares, data taken from Cammarata et al. [25]). Errors on data points (represented as bars) have been calculated as standard deviations of the scattering intensities.

ence of Hb molecules with different ligation states: proteins in the quaternary R-state having different ligation states (Ri, where i=0...4 indicates the number of bound ligands) are indeed expected to have different rates for the R-T transition. A meaningful comparison that gives some clues on differences in the R-T transition between HbA and Hb$\alpha\beta$YQ is reported in figure 3.9 panel b) where Hb$\alpha\beta$YQ data obtained using a 3 ns long photolysis pulse are compared with HbA data obtained using a 200 ns long photolysis pulse. The use of long photolysis pulses ensures that the initial fraction of Hb molecules in different ligation states is very similar for the two sets of data (see figure 3.16 reported in the next sections). The result of such comparison suggests that Hb$\alpha\beta$YQ is characterized by a significant slower R-T transition than HbA. This result will be substantiated by a more rigorous analysis presented in the following paragraphs. Indeed, a kinetic model able to describe how the populations of different molecular species vary with time, and to relate such populations to the observed scattering signals, will be used to analyze our TR-WAXS data.

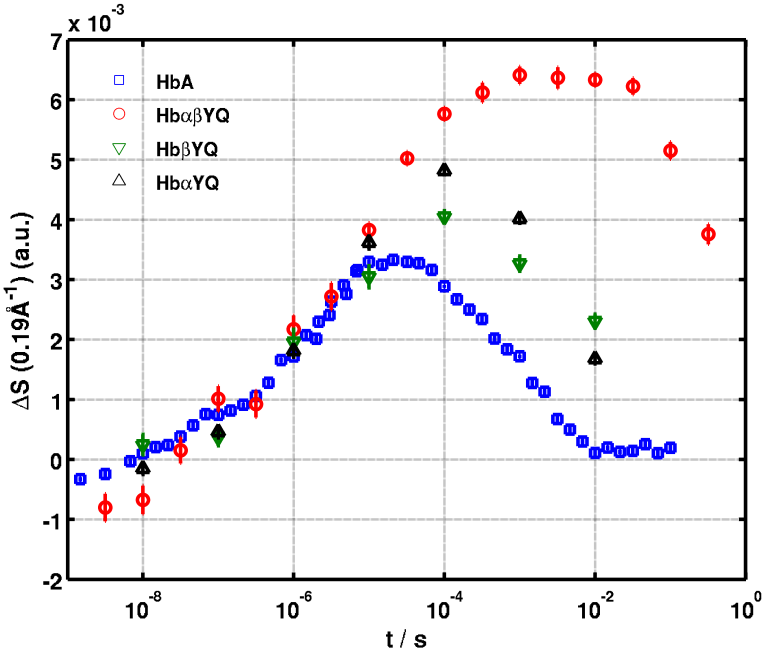

Figure 3.10: Time dependence of the amplitude of the 0.19 $\AA^{-1}$ peak. The maximum reached by the different curves is a function of the different number of Hb molecules that undergo the R-T transition. Errors on data points (represented as bars) have been calculated as standard deviations of the scattering intensities.

3.4 Kinetics of the R-T quaternary transition in HbA and Hb$\alpha\beta$YQ

As stated in the previous paragraph, it is necessary to introduce a kinetic model in order to properly take into account the various physical processes that occur after photolysis of HbCO. However, developing a kinetic model able to take into account both fast (geminate rebinding and tertiary relaxations) and slow (quaternary relaxations and bimolecular rebinding) processes requires the introduction of more than a thousand of different molecular species. Even if simplifying assumptions are introduced, such as those implemented by the so-called tertiary-two-state model (Henry et al., 1997 [102]), one typically obtains a system of 85 differential equations that is too complicated to be used for the analysis of TR-WAXS data reliably (at the present S/N ratio). A great simplification is obtained if only data at time-delays longer than approximately 250 ns are considered. Indeed, both geminate rebinding and fast tertiary relaxations are expected to take place within 250 ns [Jones et al., 1992 [103], Balakrishnan et al., 2004 [57]]. This enables the use of the same kinetic model that was applied to the study of time resolved absorption of HbCO in a typical flash-photolysis experiment by Sawicki and Gibson in 1976 [26] and that has been already applied to analyze the HbA data obtained with 200 ns long photolysis pulses [Cammarata et al., 2010 [25]]. Such model relates the observed TR-WAXS populations to the different Hb quaternary states populations and enables to extract kinetic parameters such as the R_0-T_0 rate, or the fraction of deoxy-hemes generated by the photolysis pulse, from a fitting of the experimental data.

Singular value decomposition analysis

In order to apply the above mentioned model, the number of structurally distinguishable signals contained in the TR-WAXS data has to be preliminarily determined. To this aim we have applied a singular value decomposition (SVD) analysis [101] (see also Appendix B) to the data at time delays longer than 250 ns for both HbA (316 ns - 0.1 s) and Hb$\alpha\beta$YQ (316 ns - 0.32 s) in the q-range 0.13-2.2 $\AA^{-1}$. SVD gives a series of q-patterns (singular vectors) and time-dependent amplitudes (singular vector amplitudes) that are able to reproduce the data with increasingly high fidelity as the number of singular vectors retained is increased. SVD analysis provides then a model-independent estimation of the number of structurally distinguishable species. Figure 3.11 shows the first four SVD singular vectors (together with their relative amplitudes) obtained for both samples. Judging from the magnitude of the singular values, the signal-to-noise ratios and the autocorrelations of

each SVD components, it is clear that only the first two components are significant in the case of the HbA data. It is less clear whether the third SVD component obtained for Hb$\alpha\beta$YQ should be retained or not. Indeed, the corresponding amplitude vector has an autocorrelation equal to 0.781 and the signal-to-noise ratio of the SVD basis pattern is ∼2. In view of the analogy between the SVD basis patterns of the two sets of data we judge that, also in the case of Hb$\alpha\beta$YQ, the time evolution of TR-WAXS patterns can be essentially described in terms of two basis components. A check of this assumption has been obtained by verifying, for both sets of data, that a good quality reconstruction of the experimental patterns is indeed obtained, at all time-delays, if only the first two SVD components are kept.

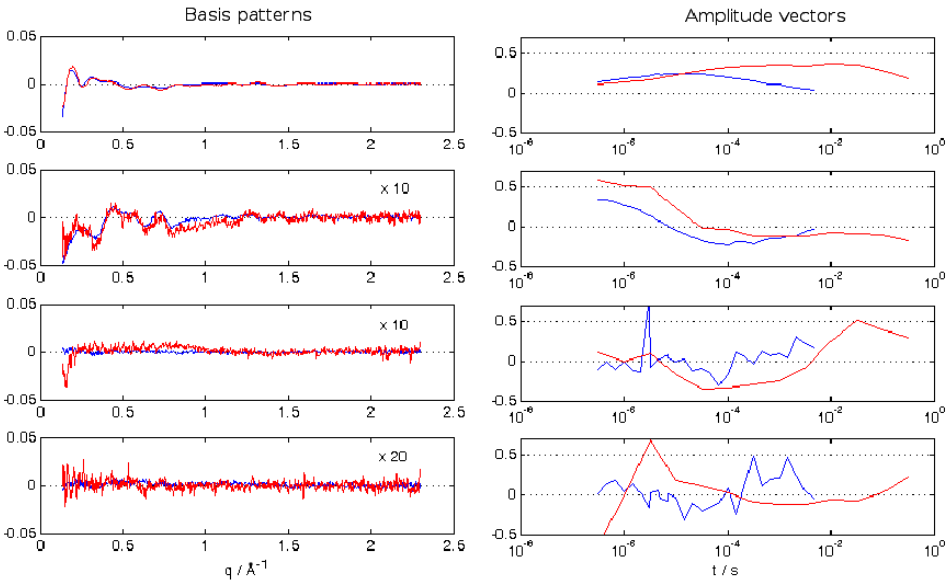

Figure 3.11: Singular value decomposition of HbA (blue) and Hb$\alpha\beta$YQ (red) data. The first four basis patterns are plotted on the left and the corresponding time-dependent amplitudes are plotted on the right. Singular values are: 0.1233, 0.0294, 0.0103, and 0.004 for HbA and 0.1295, 0.0314, 0.0182, and 0.0089 for Hb$\alpha\beta$YQ. Only the first two SVD components have large signal-to-noise ratios (≥10). The amplitude vectors autocorrelations are 0.986, 0.919, 0.748, and 0.196 for HbA and 0.965, 0.732, 0.781, and 0.135 for Hb$\alpha\beta$YQ. If the so-called rotation procedure described by Henry and Hofrichter, 1992 [101] is applied to the second and third SVD components of Hb$\alpha\beta$YQ, the following autocorrelations are obtained for the first three amplitude vectors: 0.965, 0.832, and 0.682.

SVD analysis suggests that in the time range of 316 ns-0.1 s for HbA and 316 ns-0.3 s for Hb$\alpha\beta$YQ the dataset can be reproduced as a linear combina-

tion of two independent signals. The relatively small number of independent components is surprising: with Hb being a tetramer, one would expect a large number of different tertiary substates and different ligation states in the R and T quaternary conformations to be present in solution, thus bringing about a high level of structural heterogeneity. This expectation is not supported by the data within the present signal-to-noise ratio. SVD analysis is very useful in providing a minimal description of the experimental data without any loss of information content [101]. However, the SVD components do not have, in the most general case, a direct physical meaning. For elucidation of the reaction pathway that leads to the quaternary R-T transition and a quantitative comparison of quaternary transition rates of HbA and Hb mutant, it is thus necessary to make a kinetic model of the reaction pathway in terms of interconversion between different molecular species. Furthermore, a mathematical relation between the molecular species actually existing in solution and the observed TR-WAXS patterns has to be established.

Kinetic model and fitting procedure

The above results and assumptions allow us to analyze the TR-WAXS patterns of HbA and Hb$\alpha\beta$YQ in terms of the same kinetic model that have been previously described [Cammarata et al.,2010 [25]]. The model (Figure 3.12), similar to the one originally introduced by Sawicki and Gibson, 1976 [26], assumes the presence of Hb molecules in two quaternary conformations, R and T, and five ligation states (Ri and Ti, where i=0..4). Transitions from one state to the other are accomplished by bimolecular rebinding or by interconversion between quaternary states (unimolecular ligand dissociation is neglected in view of the high CO-iron bond stability). A single bimolecular ligand rebinding rate (apart from statistical factors) is introduced in the model for each quaternary state (the microscopic bimolecular rates to R and T species are indicated as D_R and D_T, respectively). The complete set of R-T transition rates are assumed to be proportional to the R_0-T_0 transition rate and to scale down with the number of ligands bound through the parameter s (Eaton et al., 1991 [46]). The inverse T-R transition rate are linked to the direct R-T rates through thermodynamic equilibrium relations that make use of the allosteric constant L=[T0]/[R0] and the affinity ratio c=K_T/K_R, where K_T and K_R are the equilibrium association constants to T and R species, respectively. The kinetic model, schematically represented in figure 3.12, corresponds to a set of differential equations: one for each Hb microscopic state plus one that describes the time evolution of the unbound CO concentration. To solve this set of differential equations the following

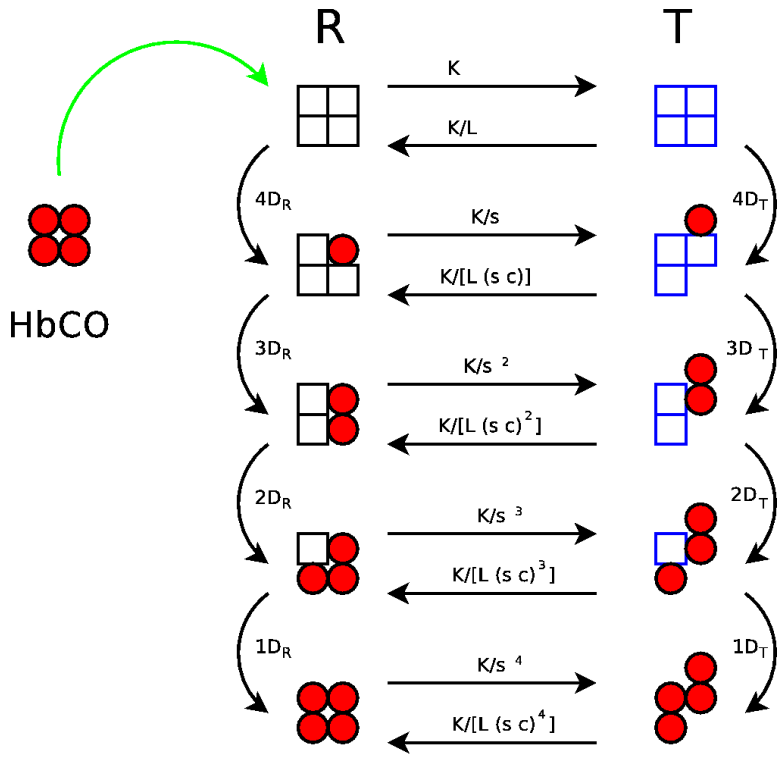

Figure 3.12: Scheme of the kinetic model used for the TR-WAXS data analysis. D_R and D_T are the microscopic bimolecular rebinding rates to the R and T species, respectively; K is the rate of the R0-T0 transition; L is the [T0]/[R0] ratio; c is the K_T/K_R ratio (K_T and K_R are the equilibrium association constants to T and R species, respectively); s is a factor that takes into account the slowing of the RT transition with increasing number of bound ligands.

initial conditions have been used:

$$T_i = 0 \quad i = 0, ..., 4 \tag{3.1}$$

$$R_i = \binom{4}{i} * N_0^i (1 - N_0)^{-1} \quad i = 0, ..., 4 \tag{3.2}$$

where N_0 is the fraction of deoxy-hemes at 250 ns from photolysis. The choice of the R_i initial populations is justified by the assumption that each photolysis event is uncorrelated with the previous photolysis of a heme-CO complex of the same Hb tetramer. In this hypothesis, the distribution of R_i ligated species is given by the above binomial distribution.
The kinetic model has seven independent parameters (N_0, K, s, L, c, D_R, and D_T). In order to reduce the number of fitting parameters D_R and D_T have been fixed to the values obtained from partial photolysis and rapid mixing measurements, respectively (Miele et al., 1999 [95] and Miele et al. 2002 [104]).
In view of the SVD results, the measured TR-WAXS patterns, ΔS(q,t), have been decomposed in terms of two basis patterns, $\Delta S_{R-like}(q)$ and $\Delta S_{T-like}(q)$, that represent, respectively, the effect of tertiary relaxations that have occurred in R_i states within 250 ns from photolysis, and that of the R-T quaternary transition:

$$\Delta S(q,t) = R - like(t)\Delta S_{R-like}(q) + T - like(t)\Delta S_{T-like}(q) \tag{3.3}$$

R-like(t) is a weighted sum of the R_i(t) populations and T-like(t) is a weighted sum of the T_i(t) populations:

$$R - like(t) = R_0(t) + \frac{3}{4}R_1(t) + \frac{2}{4}R_2(t) + \frac{1}{4}R_3(t) \tag{3.4}$$

$$T - like(t) = T_0(t) + T_1(t) + T_2(t) + T_3(t) + T_4(t) \tag{3.5}$$

where [Ri](t) and [Ti](t) denote the concentration of Hb molecules with i CO molecules bound either to R state or T state Hb and are the solutions of the set of differential equations discussed above. Note that tertiary differences are confined within individual subunits and therefore their weight is expected to scale according to the number of unbound subunits.
The kinetic parameters featuring in the model and the ΔS_{R-like}(q) and ΔS_{T-like}(q) basis patterns have been fitted against the experimental TR-WAXS patterns with an approach analogous to that used for analyzing time-resolved spectroscopic data (Henry et al., 1997 [102] & Henry et al 2002 [105]). The idea of this approach is to add a priori information on kinetics to obtain a minimal set of q-patterns (basis patterns) that are able to reproduce the data and, at the same time, have a clear physical meaning. We report below the results of such analysis

Results of kinetic analysis

Figure 3.13 reports a comparison between experimental patterns at selected time-delays and corresponding fitting curves, showing the good quality of the fitting for both HbA and Hb$\alpha\beta$YQ data. A comparison of the basis patterns obtained for the two sets of data is shown in figure 3.14. Figure 3.14 shows

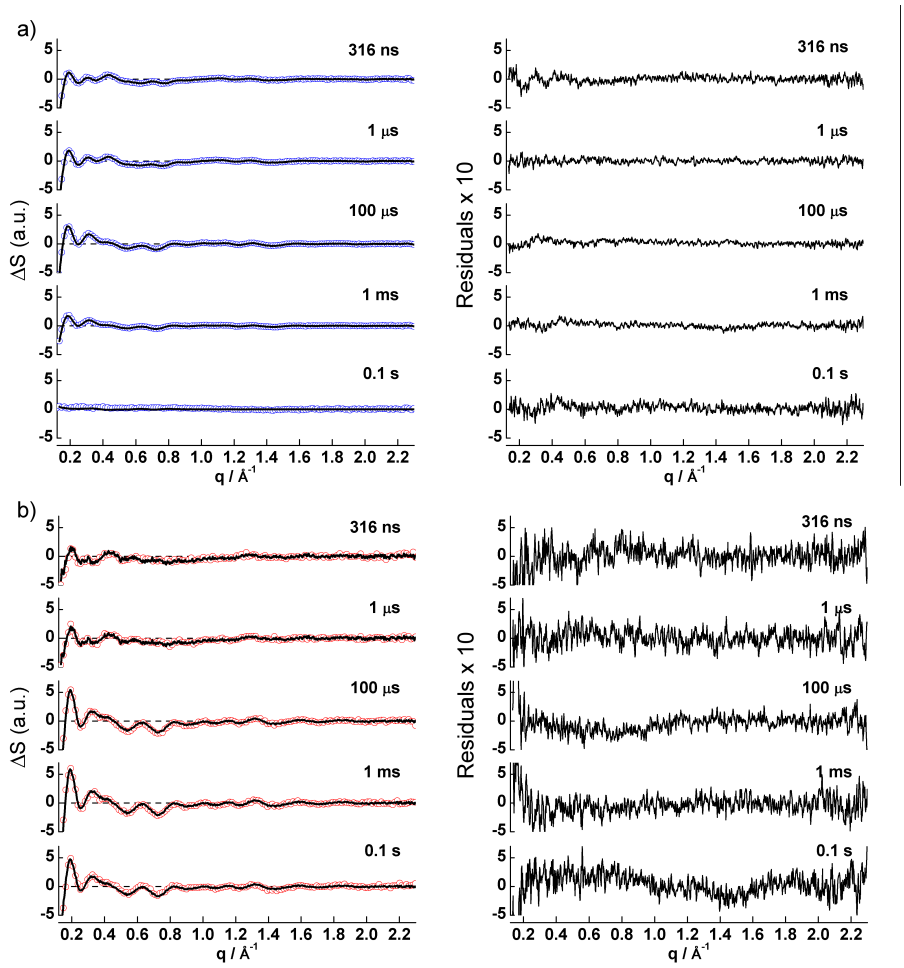

Figure 3.13: panel a): TR-WAXS patterns of HbA at selected time-delays from photolysis (open symbols) together with the corresponding fits (continuous lines) obtained with the kinetic model described in the text. Residuals are shown in an expanded scale. Panel b): same as panel a) for Hb$\alpha\beta$YQ.

that, in spite of the amino acids mutations and the corresponding effect on the geminate rebinding rate, the basis patterns obtained for HbA are very similar to those of Hb$\alpha\beta$YQ. This is a strong indication that the structural

intermediates involved in the R-T transition are essentially the same for the two Hb molecules. The kinetics of these intermediates have an overall sim-

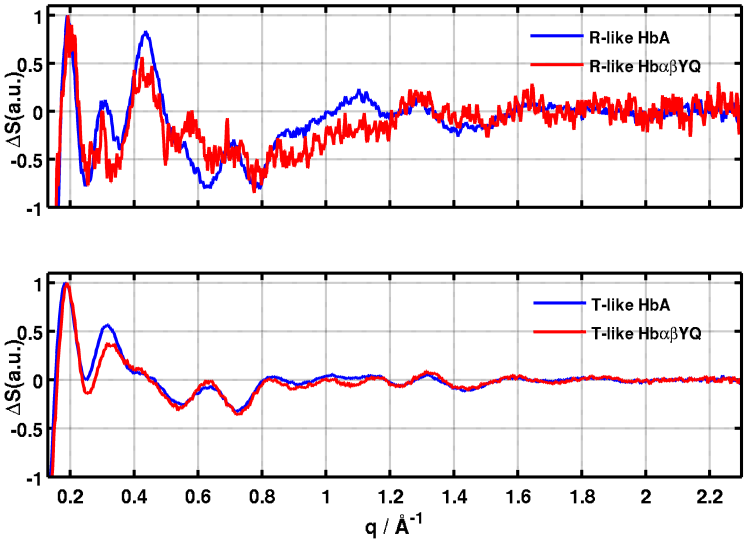

Figure 3.14: Normalized basis patterns obtained from the fitting of HbA (blue curves) and Hb$\alpha\beta$YQ (red curves) TR-WAXS patterns in terms of the kinetic model described in the text. Upper panel: normalized R-like basis patterns; lower panel: normalized T-like basis patterns.

ilar behavior as can be seen from figure 3.15: all tetramers are initially in R_i states, the R-like population decreases due to interconversion to T_i states (with the R-like population decrease being paralleled by the T-like population increase), finally the population of T_i states decreases due to bimolecular rebinding that eventually repopulates the R_4 state. The kinetic parameters obtained for HbA are in good agreement with those previously obtained using a 200 ns long photolysis pulse at three different protein concentrations (0.25, 0.5, and 1 mM) in the same buffer solution (0.1 M potassium phosphate at pH 7) [Cammarata et al., 2008 [17]]. A significant smaller fraction of deoxy-hemes at 250 ns from photolysis ($\sim$ 50% vs. 72-80 %) has been obtained as a consequence of the higher extent of geminate rebinding of the present experiment. The R_0-T_0 characteristic time (i.e., $\tau_0 = 1/K$) is close, although slightly shorter ($0.94\ \mu s$ vs. $1.2 - 1.9 \mu s$) than that obtained in previous experiments. The s value, which determines the R_i-T_i characteristic times (e.g. $\tau_1 = \tau_0 s$ in the case of the R_1-T_1 transition), is smaller than those previously obtained (9.5 vs. 14-26). Note that, in view of the much higher fraction of tetramers that undergo the R_1-T_1 transition in the present

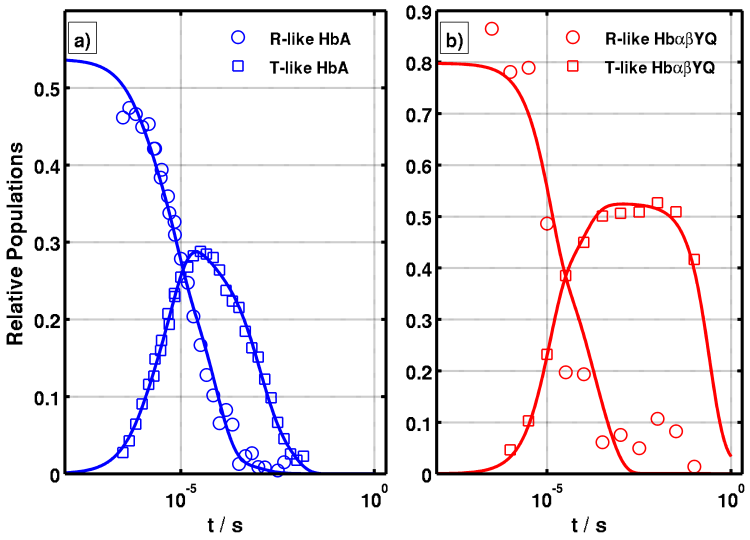

Figure 3.15: Populations obtained from the decomposition of experimental patterns as a linear combination of the R-like and T-like basis patterns reported in Figure 3.14. Left panel: R-like (open circles) and T-like (opens squares) relative populations obtained in the case of HbA. Right panel: same as left panel for Hb$\alpha\beta$YQ. In both panels, lines represent the behavior predicted by the kinetic model using the best fit parameters. The agreement between the lines and the circles is an indication of the quality of the fitting.

experiment, the new value obtained for the s parameter is better determined than the previous ones(figure 3.16 shows the distribution of R_i species after photolysis for Hb samples at different values of photolysis efficiency). Finally, the c value of 0.0026 is within the 0.0008-0.0061 range of values previously obtained; moreover it is close to the value derived from the equilibrium CO binding data of Perrella et al. 1990 [106].

The present analysis confirms that the largest structural rearrangement as-

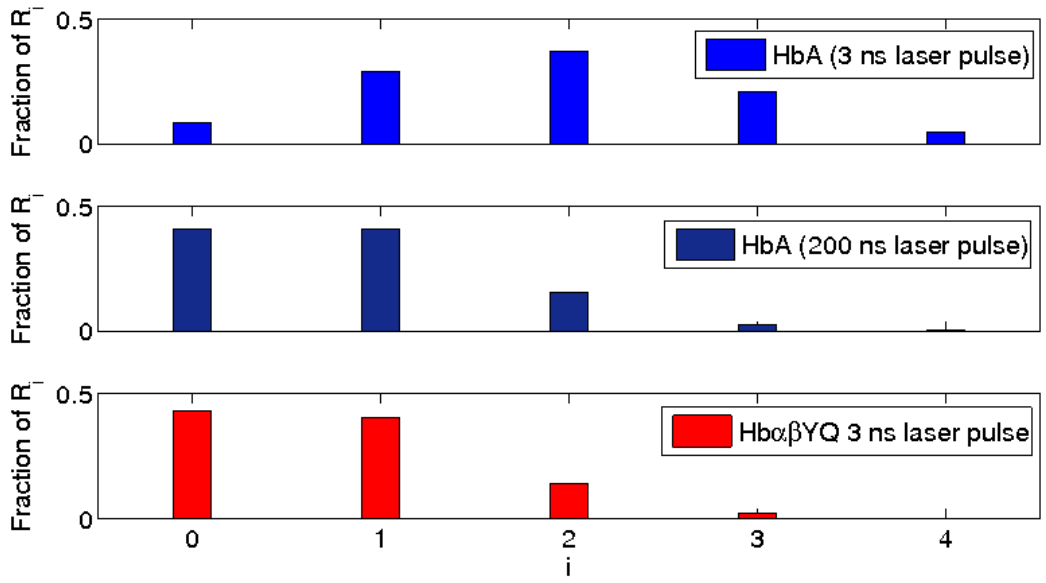

Figure 3.16: Populations of R_i states after photolysis for a) HbA sample with 54% photolysis of the total heme sites, b) HbA 78% of photolysis of the total heme sites (as obtained by Cammarata et al. 2008 [17] using a 200 ns long laser pulse) and c) Hb$\alpha\beta$YQ in 81% photolysis case.

sociated to the R-T transition of HbA (i.e. the relative dimers rotation) is much faster than those predicted on the basis of time-resolved optical spectroscopy data (Jones et al., 1992 [103]; Goldbeck et al., 1996 [107]). The use of a 3 ns long photolysis pulse in the present experiment allowed to obtain a better estimation of the R_1-T_1 time scale, which is equal to $\sim$9 μs. The kinetic parameters of Table 3.3 relative to Hb$\alpha\beta$YQ show significant differences with respect to HbA. The N_0 value is higher than that obtained for HbA (using 3 ns photolysis pulses) and falls within the range of values obtained with the 200 ns photolysis pulse in agreement with the small extent of geminate rebinding to Hb$\alpha\beta$YQ. The R_0-T_0 characteristic time of Hb$\alpha\beta$YQ is significantly longer than the HbA one. The s value is rather

high, although, as for the HbA experiments employing a 200 ns long photolysis pulse, this parameter is not well determined in view of the rather small R_1 population that goes into the T_1 state. Finally, a rather high c value of 0.049 has been obtained; unfortunately, no equilibrium CO binding data to Hb$\alpha\beta$YQ is available for comparison. We further note that, in principle, a higher value of N_0 (close to 1) would have been expected in view of the absence of geminate rebinding detected by Miele et al. 2002 [104]. The smaller value obtained could be due either to inefficiency in the photolysis of the sample (e.g. imperfect spatial superposition of photolysis and X-ray pulses, insufficient energy of photolysis pulses, or quantum yield of photolysis lower than 1) or to the presence of sub-nanosecond geminate rebinding. We note that, if the N_0 value is fixed to 1, the resulting best fit value for the R_0-T_0 characteristic time is 29 μs, i.e. even longer than the value obtained leaving N_0 as a free parameter.
A closer look at the results of the analysis can be obtained if the populations of the different states involved are plotted as a function of time (figure 3.17. Indeed, starting from the kinetic parameters of Table 3.3, it is possible to calculate the R_i and T_i concentrations at each time-delay from photolysis. Figure 3.17 (right panels) shows that, in the case of Hb$\alpha\beta$YQ, $\sim$ 36% of Hb molecules undergo the R_0-T_0 transition and $\sim$ 16% undergo the R_1-T_1 transition, while nearly 50% of Hb molecules return to the R_4 state without undergoing any quaternary conformational change. This behavior, as already pointed out, is very similar to what has be obtained for HbA using a 200 ns long photolysis pulse [Cammarata et al., 2008 [17] & 2010 [25]]. At difference, if HbA is excited with a 3 ns laser (figure 3.17, left panels) $\sim$ 8% of Hb molecules undergo the R_0-T_0 transition and $\sim$ 20% undergo the R1-T1 transition, while nearly 70% of Hb molecules return to the R_4 state without undergoing any quaternary conformational change. As we have seen, the kinetic model is able to quantitatively take into account the various processes occurring after photolysis of HbCO (although only at time-delays longer than approximately 250 ns). Our analysis shows that the R_0-T_0 transition (i.e. essentially the relative dimers rotation) in Hb$\alpha\beta$YQ is at least an order of magnitude slower than in HbA. We conclude that the active site mutations are able, not only to alter the extent of geminate rebinding and the rate of bimolecular rebinding, but also cause (as already suggested by inspection of the data) the slowing down of the large conformational change associated to the R-T transition. We would like to stress that TR-WAXS is the most suitably technique to reveal this type of effect in view of its direct sensitivity to large scale protein conformational changes.

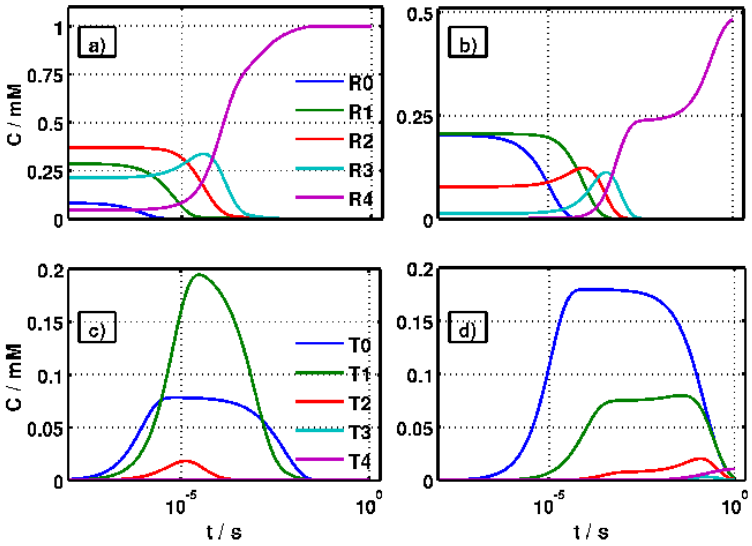

Figure 3.17: Concentrations of different ligation states in the R (upper panels) and T (lower panels) quaternary states as predicted by the kinetic model described in the text with the parameters reported in Table 1. Left panels report the results obtained in the case of HbA (1 mM in tetramer), while left panels those obtained for HbαβYQ (0.5 mM in tetramer).

Sample	N_0	τ_0 μs	s	L$\times 10^{-3}$	c$\times 10^{-3}$	D_R $\mu M^{-1}s^{-1}$	D_T $\mu M^{-1}s^{-1}$
HbA	0.52 ± 0.01	0.96 ± 0.04	9 ± 1	17 ± 1	1.4 ± 0.1	5	32.5
HbαβYQ	0.81 ± 0.01	12.4 ± 0.4	23 ± 1	20 ± 1	21 ± 2	1	0.75

Table 3.3: Kinetic parameters obtained by the fitting procedure described in the text.

3.5 Fast tertiary relaxations

In the following it is presented a preliminary analysis of the time course of structural changes observed with TR-WAXS at time delays shorter than 250 ns. The SVD analysis revealed that data at time delays longer than 250 ns can be well reproduced in terms of two SVD components. If also data at the earliest time delays (between 3 and 250 ns) are included in the analysis, a third SVD component has to be retained in order to reproduce the entire dataset both in the case of HbA and Hb$\alpha\beta$YQ (this result is evident from the shape of patterns recorded at 3.16 ns time delay that is very different from both $\Delta S_{R-like}(q)$ and $\Delta S_{T-like}(q)$ basis patterns). This implies that a structural change affecting the X-ray scattering patterns is occurring between 3 and 250 ns. As previously stated, both tertiary relaxation and geminate rebinding could in principle contribute to the observed changes in the X-ray signal. However, in view of the similarity of HbA and Hb$\alpha\beta$YQ patterns in the time range of 3-250 ns, in spite of the absence of geminate rebinding for Hb$\alpha\beta$YQ in ns time scale, we conclude that the small structural changes induced by geminate rebinding are not detectable within the current TR-WAXS resolution as distinguishable(s) structural intermediate(s). We tentatively assign this relaxation to a tertiary relaxation likely involving the relative movement of helices close to the heme pocket. In order to extract the time scale of such tertiary relaxation, we have analyzed the entire TR-WAXS dataset in terms of three patterns: the first experimental pattern (3 ns), the $\Delta S_{R-like}(q)$ and $\Delta S_{T-like}(q)$ patterns obtained using the kinetic model analysis. Note that, without a kinetic model, the choice of the decomposition basis is arbitrary (provided that it allows to reproduce experimental data within S/N). The temporal dependence of the 3 ns pattern coefficient obtained from the above mentioned decomposition has been fitted with a single exponential function imposing that it tends to zero at long time-delays. The time constants obtained are 86 ns and 48 ns for HbA and Hb$\alpha\beta$YQ respectively. The analysis of fast time delays presented is of course preliminary: as already stated in previous sections in order to extract quantitative informations a kinetic model taking into account the different tertiary species and the possible ligation states of the four sub-units has to be used. The number of time delays and their S/N ratio does not allow such kind of detailed analysis.

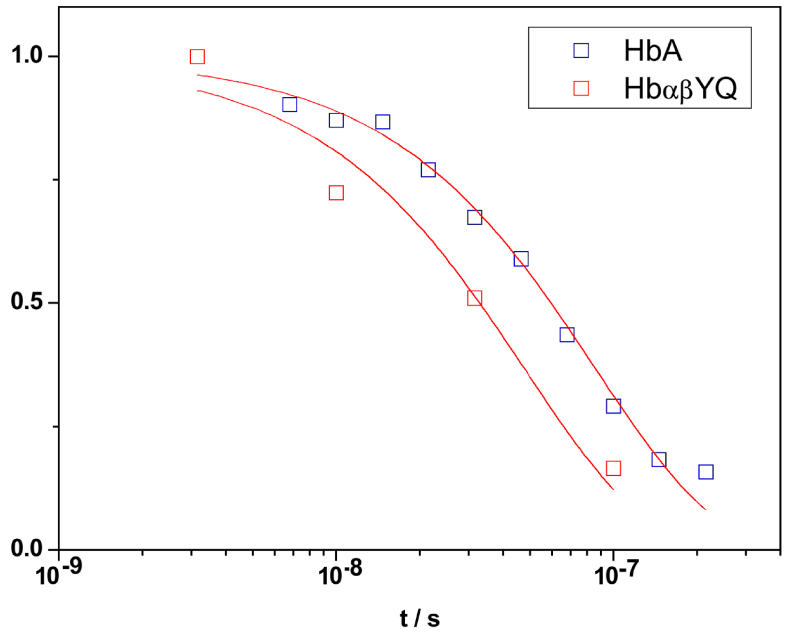

Figure 3.18: Time dependence of the 3 ns pattern coefficient. Continuous lines represent the exponential fit.

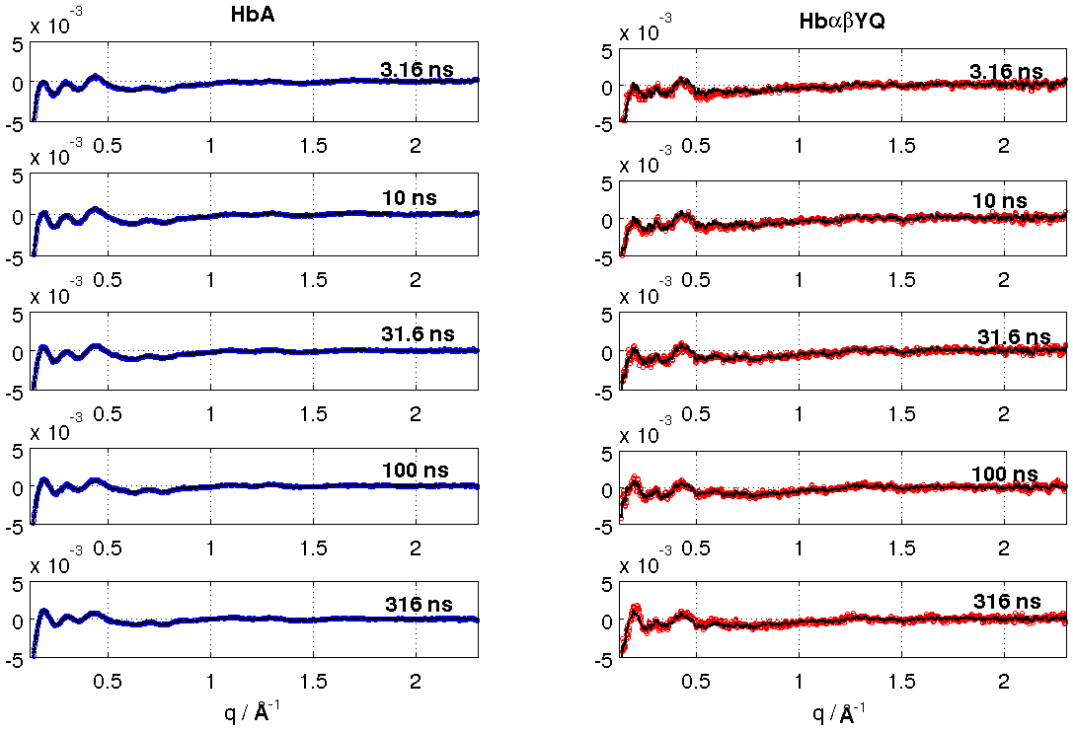

Figure 3.19: Representative time delays in 3-316 ns range for HbA (blue markers) and Hb$\alpha\beta$YQ (red markers) together with the reconstruction based on the 3.16 ns, ΔS_{R-like} and ΔS_{T-like} basis patterns (continous black lines).

3.6 Thermodynamics insights on the transition state

As early as 1991 W. A. Eaton and coworkers proposed that a linear free energy relation holds between the activation free energy of the $R_i \rightarrow T_i$ transition (ΔG_i^*) and the equilibrium free energy difference (ΔG_i) [46], i.e.:
$\Delta G_i^* = \alpha \Delta G_i + \beta$
In terms of the $R_i \rightarrow T_i$ transition rates (K_i) and of the $R_i \leftrightarrow T_i$ equilibrium constants L_i, the previous equation implies that:
$K_i = \gamma L_i^{\alpha}$
where $\gamma = A_i exp(-\beta/RT)$ and A_i is the pre-exponential of the $R_i \rightarrow T_i$ rate. By using a series of equilibrium and kinetic spectroscopic data on native human hemoglobin in different experimental conditions, Eaton and coworkers verified this relation and found $\alpha = 0.17$ and $log(\gamma) = 3.29$. It should be stressed that, within the frame of the MWC model, $L_i = L_0 c^i$ so that $K_i = K_0/s^i$, with $s = c^{\alpha}$. The linear free energy hypothesis therefore implies a linear dependence of both ΔG_i^* and ΔG_i upon the ligation index i. The MWC kinetic model used to analyze our TR-WAXS data explicitly assumes a linear dependence of ΔG_i^* and ΔG_i upon the ligation index i; its ability to fit the data relative to both HbA and Hb$\alpha\beta$YQ gives further support to the linear free energy hypothesis. A plot of ΔG_i^* and ΔG_i is reported in figure 3.20; the inset reports ΔG_i^* and ΔG_i vs. the ligation index i and shows that for the mutant Hb a switchover point (i.e. the number of bound ligands required to achieve $[R_i]=[T_i]$) $i^* = 3$ is obtained, in agreement with structural and functional data [95]. Values of $\alpha = 0.387$ and $log(\gamma) = 1.78$ are obtained for HbA, substantially different from Eaton's ones; values of the same parameters for Hb$\alpha\beta$YQ are 0.9781 and 0.61 respectively. Therefore, an apparent inconsistency seems to be present between spectroscopic (Eaton and coworkers) and TR-WAXS data relative to HbA, concerning both the timescale of the R_0-T_0 transition ($\sim 20\mu$s vs $\sim 1\mu$s) and the free energy linear relationship. A possible solution of this apparent contradiction may be traced to the recently proposed stepwise character of the R $\rightarrow$ T transition [107, 100], supported also by MD simulations [58]. According to this proposal, a first step involving the "hinge point" and the dimer rotation is followed by a second step involving the "switch point" and, likely, the ligand affinity change. Following this idea Cammarata et al. [25] proposed that the TR-WAXS signal monitors essentially the first step of the quaternary transition (namely, the dimer rotation, with time constant $\sim 1\mu$s), while time resolved optical spectroscopy monitors essentially the second, TR-WAXS silent, step likely responsible for the affinity change (time constant $\sim 20\mu$s). This proposal

finds a first confirmation in the computer simulation work of Fischer et al., 2011 that evidenced a stepwise R-T transition whereby a first large quaternary transition (Q2 in their terminology) is followed by a second much smaller quaternary step (Q1). Concerning the linear free energy hypothesis, the above argument implies that the activation free energies measured by TR-WAXS and time-resolved optical spectroscopy are not the same; in fact, the transition state involved in dimer rotation and monitored by TR-WAXS is not the same as that involved in the $\sim 20\mu$s relaxation probed by time-resolved optical spectroscopy. Given the above warnings, some interesting thermodynamic insights can be obtained from the analysis of figure 3.20. Indeed, the value of the parameter $\alpha = 0.81$ obtained for Hb$\alpha\beta$YQ suggests that, for this mutant, the activated state for the dimer rotation has thermodynamic properties much closer to those of the T conformation than to those of the R conformation.

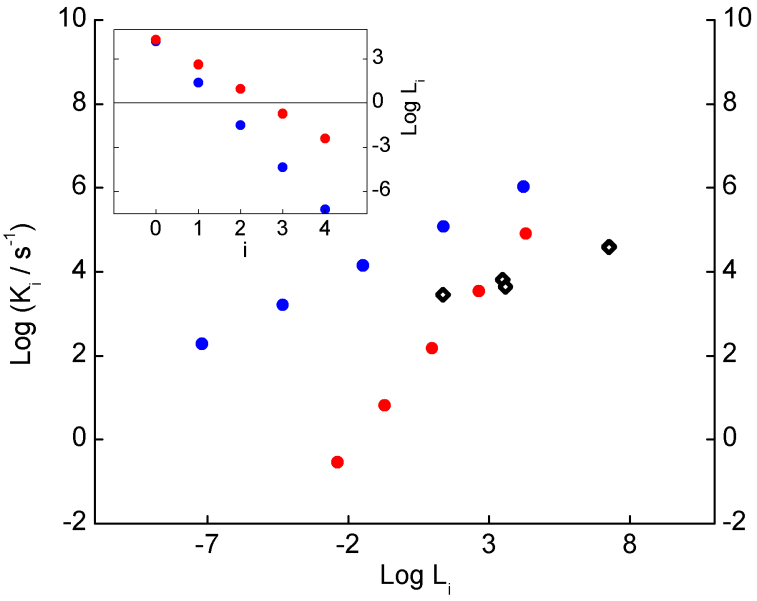

Figure 3.20: Correlation between R_i-T_i rates (K_i) and the allosteric equilibrium constants L_i for both HbA (blue symbols) and Hb$\alpha\beta$YQ (red symbols); spectroscopic data of Eaton and coworkers are also reported with black symbols. The inset shows the allosteric constant L_i as a function of the ligation index i.

Chapter 4

Probing the hemoglobin structural dynamics in red blood cells

Investigating protein structural dynamics inside the cell is a major goal of molecular biology and requires techniques apt to study structural changes in the sub-nanometer length scale with high time resolution. Time Resolved Wide Angle X-ray Scattering satisfies these requirements and here in this chapter is shown a first application to a cell system: structural changes at tertiary and quaternary level after photolysis of carboxy-hemoglobin were tracked in intact human erythrocytes with nanosecond time resolution. Human erythrocytes are also referred as red blood cells (RBC) because of the red colour given by the high concentration of Hb.

From the functional point of view, the sequestration of Hb inside specialized cells (rather than having it dissolved in plasma) allows for less viscous blood while ensuring high concentrations of oxygen. Mammalian erythrocytes are shaped as biconcave disk flattened in the center: a typical human erythrocyte has a disk diameter of 6-8 μm and a thickness of 2 μm and a volume of about 90 fL with a surface of about 136 μm^2 [108]. The specific shape of mammalian erythrocytes is due to the lack of nucleus during the maturation process (erythropoiesis) and allows more space available for Hb. Moreover, during erythropoiesis, erythrocytes also lose all other cellular organelles such as mitochondria, Golgi apparatus and endoplasmic reticulum. Their cytoplasm is rich in Hb (33% of the cell volume) which is responsible for the oxygen binding.

The membrane of the red blood cell regulates their surface deformations and flexibility: it is made up of a layer (glycocalyx) on the exterior which is rich in carbohydrates, of a lipid bilayer which contains many trans-membrane

proteins and a membrane skeleton which is a structural network of proteins in the inner surface of the lipid bilayer. In human erythrocytes the total membrane mass is due for 50% to proteins and for the other 50% to lipids (phospholipids and cholesterol). Previous studies on RBC were done with the

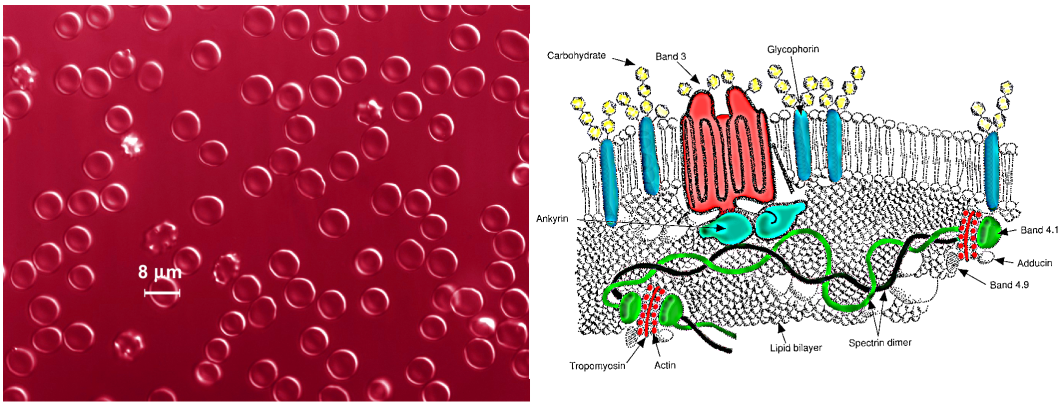

Figure 4.1: Left panel: images taken with microscope before the TR-WAXS experiment. Right panel: schematic sketch representing the complex structure of the membrane of RBC. The figure on the right panel is freely available on wikipedia.

technique of time resolved absorption coupled with flash photolysis on HbCO adduct to probe the Hb quaternary transition ([109] and references therein) or by rapid mixing experiments [111]. The distribution of Hb molecules inside RBC has been investigated by small angle neutron scattering [112]. The spectroscopic studies revealed mainly no differences in respect with HbCO experiments in solution: the results indicate that neither the rate constants nor the activation energies for the binding of CO to the fast reacting form of Hb in the RBC are significantly different from that measured in solution in spite of the different environments. A difference was observed more recently by Hoshino et al. [110] for oxygen rebinding that according to authors could be controlled by diffusion across the RBC membrane, while no effect is detectable in the case of CO. Neutron scattering, thanks to the application of variation contrast, allows to almost isolate the contribution to the scattering of the membrane cell, revealing the distribution of the Hb molecules inside the cells. A mean distance between the Hb molecule of $\sim 67\mathring{A}$ and a packing fraction of 0.24 in iso-osmolar solvent were detected. Perutz as early as 1948 using geometrical arguments calculated the volume occupied from a single Hb protein (approximated as an ellipsoid) and compared it to the mean volume of RBC. Taking into account the mean concentration of

Hb/cell he concluded that between Hb molecules in RBC there is a mean distance of about 60 $\mathring{A}$ [113]. In view of the previous results obtained on TR-WAXS studies of Hb in solution, the RBC represent the most natural choise for extending the technique to a cell system: once structural changes occurring after photolysis have been well characterized in solution, it is possible to test TR-WAXS sensitivity in tracking Hb dynamics in cell.

4.1 Experimental protocol

A fresh human blood sample was extracted and immediately diluted in a proportion 20/80 vol/vol with Ethylenediaminetetraacetic acid (EDTA) 0.1M to prevent coagulation. Plasma was removed by several cycles of dilution/centrifugation/supernatant removal in 0.9% NaCl isotonic solution. The sample was then equilibrated with humified CO for 20 min. by gentle bubbling. The solvent was substituted by several washing cycles with Na-phosphate CO-saturated buffer 150 mM pH 7.38 which guarantees isotonic condition. Suitable aliquots of the sample were pelleted by centrifugation [115] just before the measurements and deposited into a sealed sample holder. Figure 4.2 shows the experimental scheme used to apply TR-WAXS to accurately probe structural changes of Hb in intact red blood cells. The time scale investigated ranges from nanoseconds to milliseconds.
A few but important differences in the set-up were needed in respect with the solution case. In fact, when applying the same scheme used for dilute solutions to human RBC samples, several problems arise:
- RBC are microscopic objects able to scatter visible light from the laser reducing dramatically the efficiency of photolysis; moreover RBC, suspended in isotonic aqueous solutions, precipitate thus changing the local concentration and producing signal fluctuations.
- the observed scattering signal arises not only from Hb but also from other molecules in the sample, including membranes, membrane proteins etc. Moreover the low q region can be affected by the structure factor coming from the mean inter-molecules distance.
- the use of 18 keV x-ray pulses may cause the formation of free radicals [114] as a result of water radiolysis, thus producing pH jumps which compromise membranes integrity;
To overcome these experimental problems the following strategy has been adopted.
In flash photolysis experiment Q. H. Gibson et al. [115] faced a similar problem due to the visible light scattering. They observed how this effect is

minimized on a densely packed layer of RBC. To hold the sample in place they used two quartz microscope slide coverslips to regulate the optic path. The same sample holder is not recommended in X-ray scattering experiments, because of the parasitic signal from the cover slips (as we have verified in a separated experiment). Nevertheless we decided to retain the idea of using a deposit of densely packed RBC. We performed the experiment on a densely packed layer of RBC obtained by centrifugation, thus minimizing visible light scattering and avoiding RBC precipitation. In these conditions the laser penetration depth is limited to 100 μm at most due to the high local concentration obtained (about 4 mM in Hb). We then designed a suitable sample holder (figure 4.2 panel a), where the standard quartz sample holder is substituted by a cell made of mylar, which is almost transparent to both X-rays and visible light. In this way, we measured the scattering signal of the sample very close to the mylar cell surface, where laser penetration is guaranteed, without affecting the data with parasitic signals from quartz capillary vibrations and inhomogeneities. As suggested by Cammarata et al. [17, 25] a long laser pulse (200 ns) was used to improve photolysis efficiency (reducing the effect of geminate recombination).
The laser on - laser off approach (see legend of figure 4.2) was used in order to accurately subtract scattering contributions coming from sample components other than Hb while the heating contribution needed to be subtracted during data analysis.
Moreover, we used a suitable buffer concentration (buffer phosphate 130 mM) to preserve nearly isotonic conditions (290 mOsm) while minimizing the effect of free radicals and, as already done in the case of Hb in solution, we used a translation stage to move back and forth the sample holder during the measurement to dilute any radiation damage over a large volume: this approach led to a survival time of some hours under the irradiation.
The necessary check of RBC integrity was performed by inspection of RBC suspensions before and after each experiment, as shown in figure 4.2 (panels d, e and f). Even if a modest effect on cell volume is observed at the end of sample irradiation, our approach ensured that essentially no RBC lysis occurred during data acquisition. Moreover, the scattered intensity below 0.2 $\mathring{A}^{-1}$, which is sensitive to the intermolecular Hb distance [112], was monitored during the acquisition of TR-WAXS patterns in order to check sample integrity in real time (see figure 4.3).

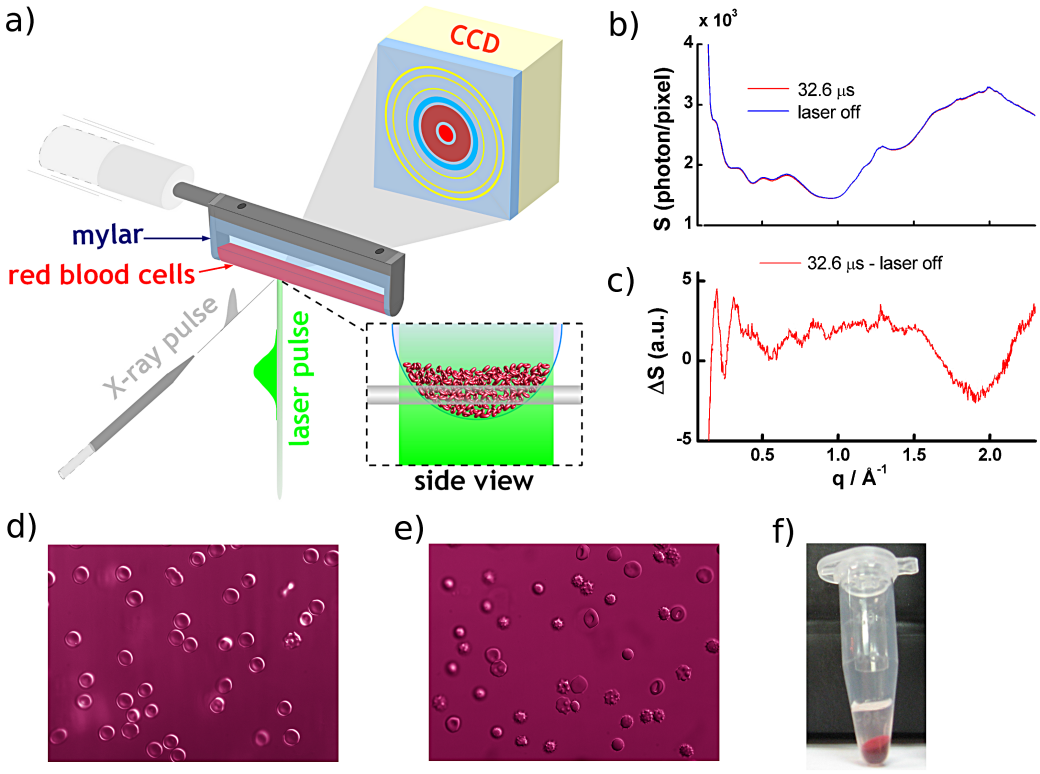

Figure 4.2: TR-WAXS methodology and data processing. a) Schematic representation of the experimental setup. Transient structures were generated by a laser pulse (green beam) that triggered the conformational change (through photolysis of the Hb-CO bond), which was followed by delayed quasi-monochromatic X-ray pulses (100 ps long) extracted from the synchrotron. Scattered X-rays were recorded in the forward direction by a sensitive CCD camera. b) Each image was azimuthally averaged and converted into a one-dimensional curve I(q). c) After normalization, a reference scattering pattern, which probed the unexcited sample (laser off), was subtracted from the scattering pattern at a given time delay (laser on). These difference patterns (laser on - laser off) are "fingerprints" of the transient protein structural changes. d) e) Comparison between microscope images taken before and after X-ray exposure to check RBC integrity. f) Sample after centrifugation. After X-ray exposure the sample was centrifuged checking that no detectable free Hb concentration was in the supernatant.

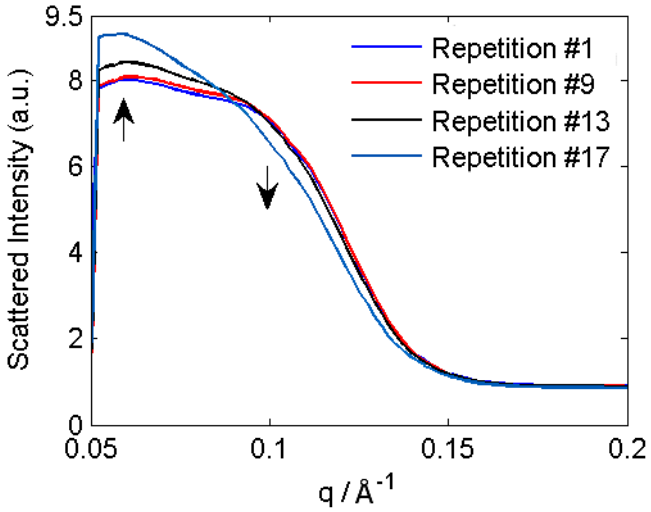

Figure 4.3: Effect of X-ray irradiation on packed RBCs. Absolute scattering patterns measured in the absence of the photolysis laser (laser off images) are reported in the 0.05-0.1 $\AA^{-1}$ region after normalization at 2.1 $\AA^{-1}$. The scattering signal in this region is sensitive to Hb intermolecular distance and to RBC membrane structure. A continuous monitoring of this region can be used as a real time check of radiation damage on RBCs. Only data showing less than 5% variation in the scattered intensity have been retained for data analysis.

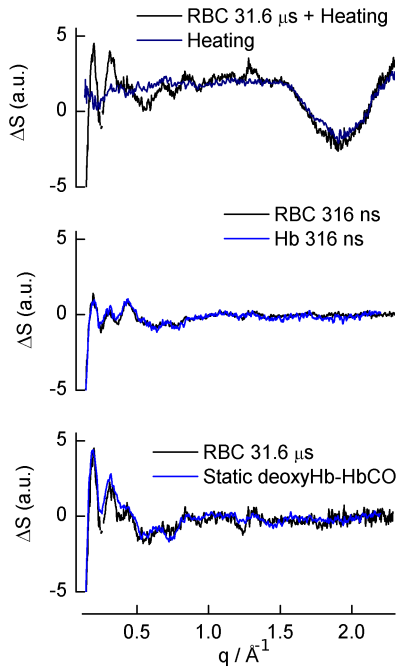

Figure 4.4: TR-WAXS data on RBC and the solvent heating contribution. a) TR-WAXS data at 31.6 μs after photolysis compared with that at 32 ms; 32 ms after photolysis, the unbound CO molecules have recombined to Hb and the scattering signal is due essentially to a temperature rise of the solvent. The 32 ms pattern was used to subtract the solvent response at any time delay after proper scaling. b) TR-WAXS signal on RBC at 31.6 μs after photolysis (heating-subtracted) compared with the static equilibrium scattering difference between a deoxyHb equilibrium sample and an HbCO sample in solution. The RBC pattern has been scaled onto the HbCO one. c) The TR-WAXS pattern obtained at 316 ns from photolysis of RBC and HbCO is shown to demonstrate the sensitivity of the technique to local tertiary structural changes. The RBC pattern has been scaled onto the HbCO one.

4.2 TR-WAXS on RBC

Laser on - laser off X-ray scattering difference signals contain not only fingerprints from protein structural changes but also solvent heating contributions arising from changes in solvent temperature, density and pressure induced by the energy transferred from the laser into the solvent via protein absorption. To decouple the two contributions and in view of the similarity of the shapes of difference patterns in high angle region with those measured on HbA in solution, we subtracted the heating contribution at each time delay using the same procedure described in chapter 3. Another possibility, as suggested by Cammarata et al. [17] is to subtract from each time delay the difference pattern recorded at 32 ms after photolysis when Hb recovered the initial state while heating has not yet diffused out of the voulme probed by X-rays. We tried both procedures obtaining the same results (see figure 4.4 a)).
In figure 4.4 we plotted the heat-removed time-resolved patterns at 316 ns, compared to analogous data in solution (panel b), and at 10 μs, compared with a difference between R and T static WAXS patterns (panel c). The data, scaled to take into account the differences in concentration and photolysis conditions, show that the procedure adopted allows to isolate the protein structural signal: the technique is sensitive to quaternary conformational changes occurring in cell, as revealed by comparing the shape of the transient pattern at 10 μs with a difference between R and T Hb static patterns. Moreover the tertiary relaxation pattern is very similar to that measured in solution. These results validate the heating subtraction procedure used on RBC samples.
In order to get more quantitative information on the kinetics of conformational changes, the whole dataset of TR-WAXS data was fitted with a MWC kinetic model already successfully used for analogous data in solution. Details on the kinetic model and the fitting procedure are reported in chapter 3 and appendix A. In figure 4.5 are shown fitting curves at different time delays, while in figure 4.6 time evolution of R-like and T-like populations is reported. In table 4.1 the main kinetic parameters obtained are reported: note that the time scale of the quaternary R-T transition inside RBC is the same as in the case of dilute solutions. Because of the low excitation fraction obtained (about 50%), R_0 state is poorly populated after photolysis in respect with R_1 and R_2 state. Moreover due to the high concentration of CO after photolysis ($\sim$ 10 mM), the bimolecular rebinding process from the R state competes efficiently with quaternary transition: R_i species have the possibility to recombine CO and coming back to R_4 state before having the time to switch to T_i state. If a $D_R = 7.9\ \mu M^{-1}s^{-1}$ is assumed, as in the solution case, the time scale of bimolecular rebinding is expected to be in the

3-13 μs range for R_i with i=0,..,3 i.e. in the same time scale of the expected quaternary transition (if not faster for R_1 R_2 as well as R_3. See table 4.1). These effects limit the fraction of molecules doing the quaternary transition and then reduce the reliability of fitting results.
In order to reduce the number of free parameters and compare the results of the fitting to the solution case, we decided to fix all the kinetic parameters to the values obtained for Hb in solution previous publicated by Cammarata et al. except for R_0-T_0 transition rate and the excitation fraction that were left as free parameters. In fact, how stated above, previous in vivo measurements of CO-binding to Hb have shown no effect on the bimolecular rebinding process in respect with what observed in solution. Moreover, imposing the same value of L we are assuming that T state and R state have the same stability in cell as they have in solution. During the sample preparation RBC were "washed" many times loosing most of 2,3 diphosphoglycerate that is an allosteric factor promoting the stability of T conformation. In principle other factors such as the confinement and/or inter-molecule interactions can affect the stability of T and R conformations but in view of the results obtained there is not such evidence. The results here reported demonstrate that the crowding and confinement conditions experienced by Hb in RBC do not influence significantly the tertiary and quaternary structural dynamics probed by TR-WAXS with respect with what observed in dilute solutions.
The TR-WAXS set-up here presented is the first application of this technique to a cell system and succeeded in tracking tertiary and quaternary conformational changes of Hb in intact human cells. The results obtained allow to extend our previous knowledge of Hb structural dynamics to the crowed and confined environment of the cell and can give a reference for future studies on Hb protein concentration effects and on matrix confinement effects in vitro [116, 117].
In 2008 Makowski et al. [19] used a combination of wide angle X-ray scattering (WAXS) and computational modeling to investigate the spatial scale of conformational fluctuations in solution of different proteins, including Hb. The authors observed concentration-dependent changes in the scattering intensities. The fluctuations observed increase with decreasing protein concentration or increasing temperature. The results have been interpreted by authors as due to increase in the scale of collective motion of the proteins as protein concentration decreases; moreover a change in the structure of the proteins or oligomerization and aggregation processes can not be ruled out. In particular in the case of bovine met-Hb the authors observed a change (startig from lower concentrations) at 50 mg/ml (corresponding to a molar concentration of $\sim$0.8 mM) in the WAXS pattern suggesting a modification of the protein structure. In the resolution limit of the TR-WAXS technique

there is no significant differences in both tertiary and quaternary structural intermediates between RBC sample and Cammarata et al. data (obtained on 0.5 mM Hb-solution). However a little concentration-dependent effect on R_0-T_0 time scale can be observed: the time scale of $\sim$1 μs obtained both in Hb 1mM solution (see chapter 3) and RBC sample is little shorter than 1.9 μ s reported by Cammarata et al. for Hb 0.5 mM solution. But an effect of the different heating amplitude (to a first approximation the heating grows with the concentration) could partially explain this difference.

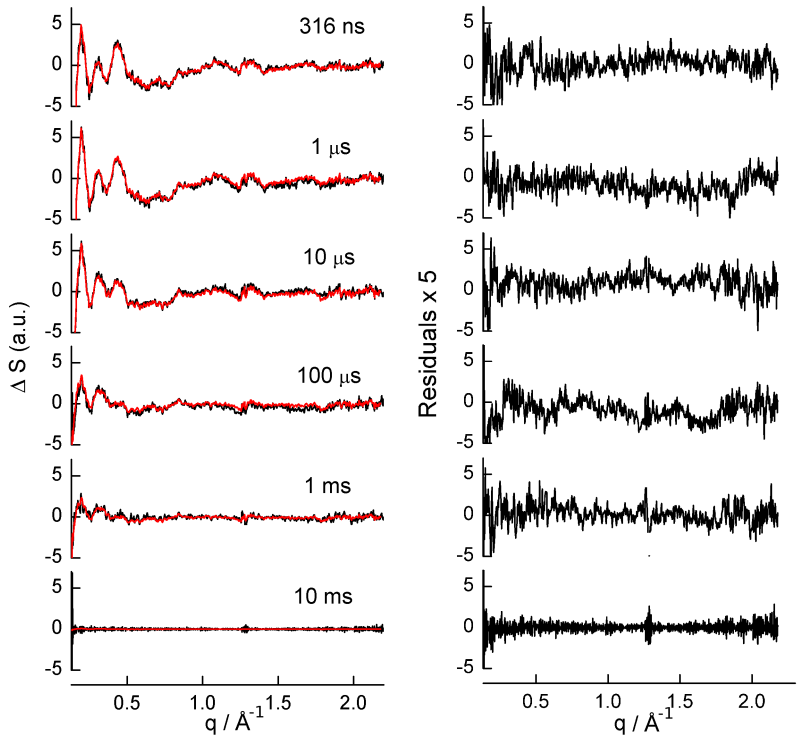

Figure 4.5: Laser-induced changes of the scattering patterns for several selected time delays (black, after solvent response subtraction). Data at all time delays have been fitted as a linear combination of the ΔS_{R-like} and ΔS_{T-like} patterns (red). The time evolution of the basis patterns is governed by the kinetic parameters reported in table 4.1

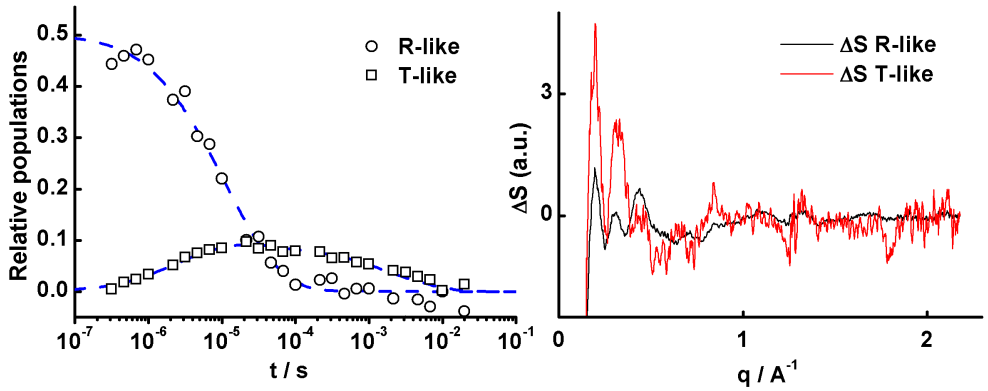

Figure 4.6: The population kinetics of R-like species and T-like species estimated from TR-WAXS data. The kinetic model used for fitting takes into account two basis patterns namely $\Delta S_R - like$ (representing the signal arising from excited proteins in quaternary R-state) and $\Delta S_T - like$ (arising from the proteins undergoing the quaternary transition). The presence of 5 possible ligation states Ri and Ti (i=0,...4 being the number of bound CO molecules per Hb) is explicitly taken into account constituting respectively the R-like and T-like populations. Given a set of kinetic parameters the model allows to calculate R-like and T-like population as a function of time and reconstruct experimental data as a linear combination of the two basis patterns. The whole procedure can be iterated to find the best fit values for the kinetic parameters.

Sample	N_0	τ_0 μs	s	L$\times 10^{-3}$	c$\times 10^{-3}$	D_R $\mu M^{-1}s^{-1}$	D_T $\mu M^{-1}s^{-1}$
Hb in RBC	0.50±0.01	1.13±0.04	14	8.85	2.9	7.9	31
Hb in solution	0.81±0.01	1.9 ± 0.2	14 ± 1	8.85	2.9 ± 0.3	7.9 ± 0.3	31 ± 1

Table 4.1: Kinetic parameters obtained by the fitting procedure. In RBC sample the concentration of Hb was 4.4 mM and the T-jump due to laser transferred energy was ΔT=6 K. Hb solution data (0.5 mM ΔT=1 K) are reported for comparison [25].

Chapter 5

Conclusions

The field of time resolved structural techniques on biological samples is a rapidly evolving field: the number of dedicated laboratories at synchrotron light sources is constantly growing as well as the number of proposals submitted by the scientific community. The high temporal resolution achieved, combined with the possibility of using different kinds of excitation (flash-photolysis, pH jump, T jump) allows the study of a variety of macromolecular machine systems. As it is clearly stated in this thesis, a major challenge of these studies is represented by the complexity of data analysis: in the case of complex proteins, such as multi-domain proteins, data analysis requires kinetic models of the reaction observed. Moreover, because of the directional average due to the solution disorder, the technique requires adequate modeling techniques in order to extract the structural information contained in experimental data. A coupled approach including experimental TR-WAXS data and computational methods is highly desiderable. Moreover the development of the free electron lasers (FEL) x-ray sources in Europe (XFEL in Hamburg) and in USA (LCLS in Stanford) contributed to the development of this technique allowing an even higher time resolution and photon flux. Thanks to this new light source single molecule structure from nanocrystals [118], as well as continuous diffraction pattern of non crystalline objects [119] are becoming accessible.

While both the dynamics and structure of proteins remain at the center of scientific debate, recently the interest of scientific community is focused on the in vivo studies of proteins function. In the final chapter of this thesis we have shown how it is possible to extend TR-WAXS to probe conformational changes of Hb inside intact red blood cells. Other in vivo processes such as light transduction by trans-membrane proteins like bacteriorhodopsin cuold be studied in the future: indeed large laser-induced conformational changes were already observed in solutions [120] while the gradient in salt concentra-

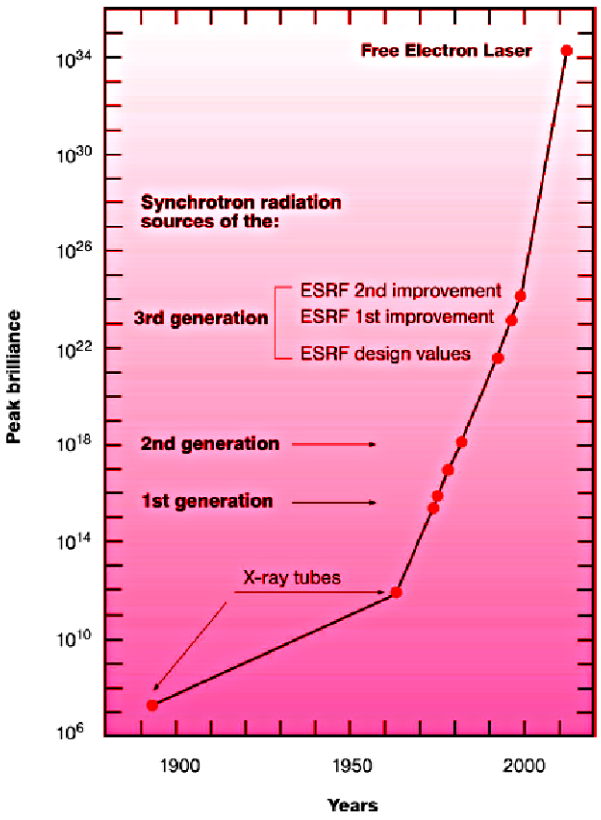
Free Electron Laser
Synchrotron radiation sources of the:
3rd generation
ESRF 2nd improvement
ESRF 1st improvement
ESRF design values
2nd generation
1st generation
X-ray tubes
Peak brilliance
10^{34}
10^{30}
10^{26}
10^{22}
10^{18}
10^{14}
10^{10}
10^{6}
1900
1950
2000
Years

tion across the membrane in vivo could affect bacteriorhodopsin functional dynamics. Moreover the protein local concentration per cell in Halobacterium salinarum is lower than in the RBC case allowing a large excitation fraction before the laser pulse is absorbed. Experiments on this system are currently under study. TR-WAXS, thanks to the high time and spatial resolution achieved, can be a useful tool to complement and extend results obtained with other time-resolved technique on in-vivo protein dynamics.

Chapter 6

Appendix A: fitting procedure of TR-WAXs data according to the kinetic model

Here some details about the analysis of experimental TR-WAXS data on the basis of the kinetic model shown in chapter 3 are given. The kinetic model corresponds to a set of differential equations describing the time evolution of the different species present in solution according to the model.

The above system has been solved numerically with the following initial parameters:

$$T_i = 0 \quad i = 0, ..., 4 \tag{6.1}$$

$$R_i = \binom{4}{i} * N_0^i (1 - N_0)^{-1} \quad i = 0, ..., 4 \tag{6.2}$$

where N_0 is the fraction of deoxyhemes after the pump pulse, using the explicit Jacobian and a requested absolute precision of 10^{-15}. The fitting program has been implemented in C++ and used the following libraries:
LSODE as provided by Octave 3.0 (to solve the system of differential equations)
Newmat 11 (for matrix calculation/inversion)
Minuit 1.7.9 (for χ^2 minimization)
The fitting program calculates all $R_i(t)$ and $T_i(t)$ and the concentration of CO in solution.These quantities are used to calculate the $R_likе(t)$ and $T_likе(t)$ as discussed in the chapter 3.

$$
\begin{aligned}
\partial[CO]/\partial t &= -\sum_{k=0}^{3} -k\, D_R[CO][R_i] \quad -\sum_{k=0}^{3} -k\, D_T[CO][T_i] \\
\partial[R_0]/\partial t &= -K_{R_0\to T_0}[R_0] \quad -4\, D_R[CO][R_0] \quad +\left(K_{R_0\to T_0}/L\right)[T_0] \\
\partial[R_1]/\partial t &= -\left(K_{R_0\to T_0}/s^1\right)[R_1] \quad +4\, D_R[CO][R_0] \quad -3\, D_R[CO][R_1] \quad +\left(K_{R_0\to T_0}/L\right)\cdot\left(1/(s\,c)^1\right)[T_1] \\
\partial[R_2]/\partial t &= -\left(K_{R_0\to T_0}/s^2\right)[R_2] \quad +3\, D_R[CO][R_1] \quad -2\, D_R[CO][R_2] \quad +\left(K_{R_0\to T_0}/L\right)\cdot\left(1/(s\,c)^2\right)[T_2] \\
\partial[R_3]/\partial t &= -\left(K_{R_0\to T_0}/s^3\right)[R_3] \quad +2\, D_R[CO][R_2] \quad -1\, D_R[CO][R_3] \quad +\left(K_{R_0\to T_0}/L\right)\cdot\left(1/(s\,c)^3\right)[T_3] \\
\partial[R_4]/\partial t &= -\left(K_{R_0\to T_0}/s^4\right)[R_4] \quad +1\, D_R[CO][R_3] \quad +\left(K_{R_0\to T_0}/L\right)\cdot\left(1/(s\,c)^4\right)[T_4] \\
\partial[T_0]/\partial t &= +K_{R_0\to T_0}[R_0] \quad -4\, D_T[CO][T_0] \quad -\left(K_{R_0\to T_0}/L\right)[T_0] \\
\partial[T_1]/\partial t &= +\left(K_{R_0\to T_0}/s^1\right)[R_1] \quad +4\, D_T[CO][T_0] \quad -3\, D_T[CO][T_1] \quad -\left(K_{R_0\to T_0}/L\right)\cdot\left(1/(s\,c)^1\right)[T_1] \\
\partial[T_2]/\partial t &= +\left(K_{R_0\to T_0}/s^2\right)[R_2] \quad +3\, D_T[CO][T_1] \quad -2\, D_T[CO][T_2] \quad -\left(K_{R_0\to T_0}/L\right)\cdot\left(1/(s\,c)^2\right)[T_2] \\
\partial[T_3]/\partial t &= +\left(K_{R_0\to T_0}/s^3\right)[R_3] \quad +2\, D_T[CO][T_2] \quad -1\, D_T[CO][T_3] \quad -\left(K_{R_0\to T_0}/L\right)\cdot\left(1/(s\,c)^3\right)[T_3] \\
\partial[T_4]/\partial t &= +\left(K_{R_0\to T_0}/s^4\right)[R_4] \quad +1\, D_T[CO][T_3] \quad -\left(K_{R_0\to T_0}/L\right)\cdot\left(1/(s\,c)^4\right)[T_4]
\end{aligned}
$$

Figure 6.1: This kinetic model reported in figure 3.12 is described by the equations reported above.

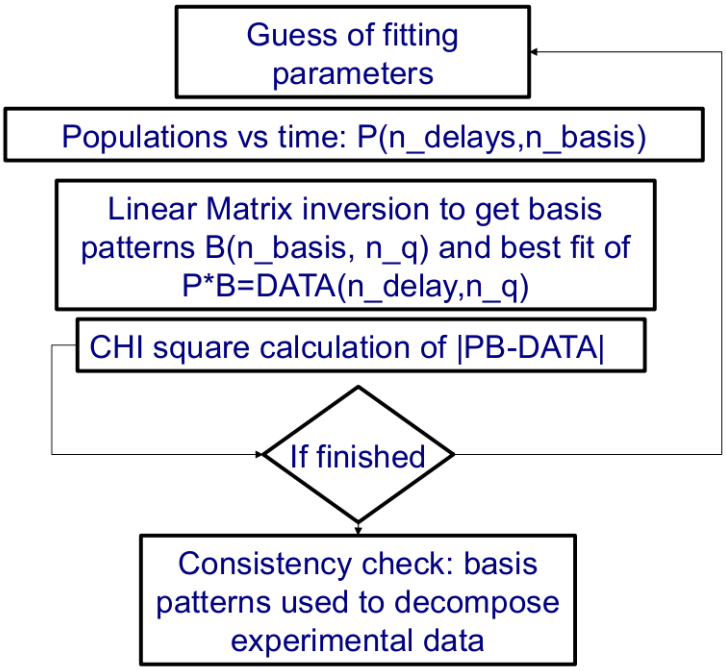

Figure 6.2: Scheme of the fitting procedure.

Chapter 7

Appendix B: a short introduction to SVD analysis

Singular Value Decomposition (SVD) is a factorization of a real or complex n_q x n_t matrix M as M = USV' where:
- U is n_q x n_t with U'U equaling the identity
- S is an n_t x n_t diagonal matrix
- V is an n_t x n_t orthogonal matrix. Here (') indicates matrix transposition.

In the case of TR-WAXS data, SVD analysis starts by organizing a dataset in a n_q x n_t matrix M with n_q q-points and n_t time delays. U contains n_t q-patterns that are orthonormal. The diagonal matrix S contains the n_t singular values that express the weight of each q-pattern found in U. The columns of the US matrix are named "singular vectors" and they are ordered with decreasing norm. The matrix V contains the amplitudes of the singular vectors for each time delays.

In the case of large experimental datasets, SVD analysis helps in finding the minimal set of basis patterns able to reconstruct the experimental data with high fidelity. When a certain physical property of the sample is measured as a function of time, the estimation of independent signals evolving with time gives the number of species distinguishable according to the specific property measured. In the case of TR-WAXS data, SVD analysis provides then a model-independent estimation of the number of structurally distinguishable species. Referring to the HbA data reported in chapter 3 for example, the two SVD components identified in the 300 ns 0.1 s range were interpreted as a tertiary relaxation and a quaternary one. This was the starting point for the application of the simple kinetic model shown in the same chapter. The number of distinguishable species in general does not correspond to the actual number of species present in solution and evolving in time. For example the quaternary signal associated with R_i-T_i transitions is the same, in the

resolution limit of the technique, but the time evolution of the this signal is affected by the heterogeneity of species contributing to it: in order to properly reconstruct the time evolution of the quaternary signal we had to take into account the presence of i=0,..,4 different species each one with a different time constant for R_i-T_i relaxation and the thermodynamic equilibrium between them. For a complete introduction to the SVD analysis the interested reader can refer to the review of E. R. Henry and J. Hofrichter [101].

Chapter 8

Appendix C: HbCN experiment and heating subtraction

As reported in chapter 3 and 4, the difference patterns measured at fixed time delays after photolysis of HbCO adducts contain not only contributions related to structural changes of the protein but also contributions arising from the heating of the solvent as a consequence of energy transferred via protein absorption. In previous works Cammarata et al. [17, 25] faced the same problem suggesting two possible approaches. The first one is to estimate the heating contribution from time delays at which the Hb has recovered the initial configuration while the heating has not yet diffused out of the volume probed by X-rays. The second consists in including the heating signal in the fitting procedure, with a temporal dependence obtained from the solution of hydrodynamics equations. We decided to follow the first approach and to improve it, measuring directly the contribution arising from solvent heating at different time delays. To this purpose we measured TR-WAXS difference patterns on a 0.5 mM HbCN sample in 0.1 M phosphate buffer solution pH 7, excited with 532 nm laser pulse (circular polarization) and $\sim$ 1 mJ/mm^2 energy density. In these conditions the laser is absorbed by HbCN molecules (with an extinction coefficient very similar to the HbCO one) while the Fe-CN bond is not photolyzed. Only the effect of solvent heating as resulting from energy transfer via protein absorption is then measured. After this, we used the HbCN dataset to estimate the heating contribution for HbCO dataset at the corresponding time delays (searching for the best coefficient to scale the HbCN data onto the HbCO ones). The same procedure was used also in the case of RBC experiment in view of the similar shape of TR-WAXS patterns in the high angle region in respect with solution data on HbCO.

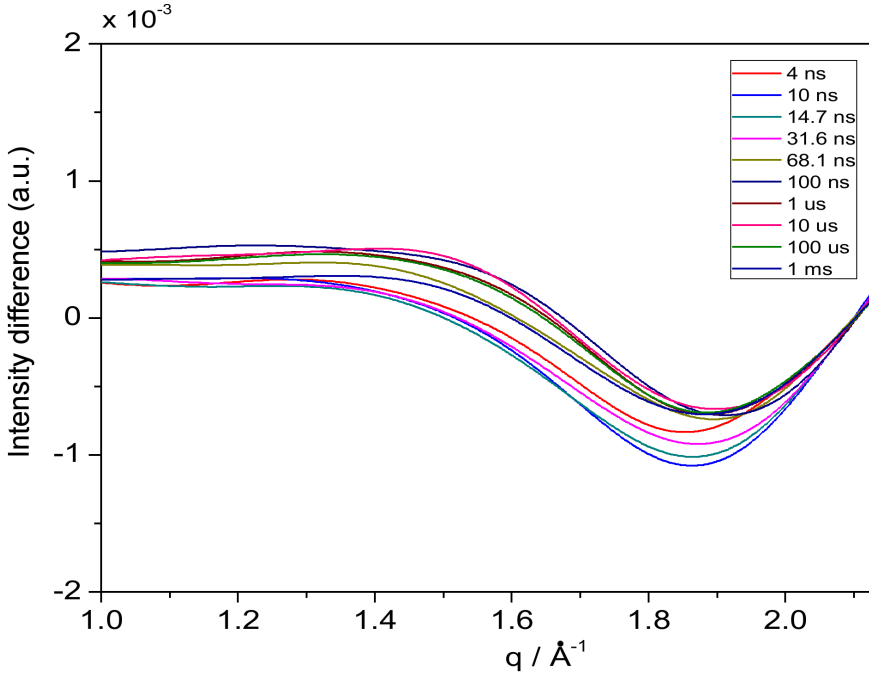

Figure 8.1: TR-WAXS data on HbCN sample at representative time delays after the laser pulse. The data are reported after smoothing with spline method.

Bibliography

[1] C. Kendrew, G. Bodo, H. M. Dintzis, R. G. Parrish, H. Wyckoff & D. C. Phillips. Nature 181, 662-666 (1958).

[2] W. Bolton, M. Perutz. Nature 228, 551-552 (1970).

[3] C. C. F. Blake, D. F. Koenig, G. A. Mair, A. C. T. North, D. C. Phillips & V. R. Sarma. Nature 206, 757-761 (1965).

[4] Protein data bank site: http://www.pdb.org/.

[5] K.B. Zeldovich, P. Chen, E.I. Shakhnovich. Proc. Natl. Acad. Sci. USA 104, 16152-16157 (2007).

[6] R. H. Austin, K. W. Beeson, L. Eisenstein, H. Frauenfelder, I. C. Gunsalus. Biochemistry 14, 5355-5373 (1975).

[7] J. R. Lakowicz, G. Weber. Biochemistry 12, 4171-4179 (1973).

[8] H. X. Zhou, J. A. McCammon. Trends in Biochemical Sciences 35, 179-185 (2010).

[9] H. Y. Wang, S. Lin, J. P. Allen, J. C. Williams, S. Blankert, C. Laser, N. W. Woodbury. Science 316, 747-750 (2007).

[10] D. N. Beratan, S. S. Skourtis, I. A. Balabin, A. Balaeff, S. Keinan, R. Venkatramani, D. Xiao. Accounts of Chemical Research 42, 1669-1678 (2009).

[11] V. J. Hilser, E. B. Thompson. Proc. Natl Acad. Sci. USA 104, 8311-8315 (2007).

[12] M. Brunori. Trends Biochem. Sci. 24, 158-161 (1999).

[13] E. Antonini & M. Brunori. *Hemoglobin and Myoglobin in Their Reactions with Ligands*. North Holland, Amsterdam, The Netherlands (1971).

[14] J. Monod, J. Wyman & J. P. Changeux. J. Mol. Biol. 12, 88-118 (1965).

[15] M. F. Perutz. Nature 228, 726-734 (1970).

[16] M. F. Perutz. Annu. Rev. Physiol. 52, 1-25 (1990).

[17] M. Cammarata, M. Levantino, F. Schotte, P. Anfinrud, F. Ewald, J. Choi, A. Cupane, M. Wulff, H. Ihee. Nature Methods 5, 881-886 (2008).

[18] D. I. Svergun et al. J. Appl. Crystallogr. 30, 798-802 (1997).

[19] L. Makowski, D. J. Rodi, S. Mandava, D. D. L. Minh, D. B. Gore and R. F. Fischetti. J. Mol. Biol. 375, 529-546 (2008).

[20] K. Moffat. Nat. Struct. Biol. 5, 641-643 (1998).

[21] F. Schotte, M. Lim, T. A. Jackson, A. V. Smirnov, J. Soman, J. S. Olson, G. N. Phillips, M. Wulff and P. A. Anfinrud. Science 300, 1944-1947 (2003).

[22] H. Ihee, S. Rajagopal, V. Srajer, R. Pahl, S. Anderson, M. Schmidt, F. Schotte, P. A. Anfinrud, M. Wulff and K. Moffat. Proc. Natl. Acad. Sci. USA 102, 7145-7150 (2005).

[23] M. Kainosho, M. Kainosho, T. Torizawa, Y. Iwashita, T. Terauchi, A. Mei Ono and P. Güntert. Nature 440, 52-57 (2006).

[24] S. Westenhoff, E. Nazarenko, E. Malmerberg, J. Davidsson, G. Katonaa and R. Neutze. Acta Cryst A66, 207-219 (2010).

[25] M. Cammarata, M. Levantino, M. Wulff, A. Cupane. Journal of Molecular Biology, 400, 951-962 (2010).

[26] C. Sawicki & Q. Gibson. J. Biol. Chem. 251, 1533-1542 (1976).

[27] J. Hofrichter, J. H. Sommer, E. R. Henry, & W. A. Eaton. Proc. Natl Acad. Sci. USA 80, 2235-2239 (1983).

[28] L. P. Murray, J. Hofricter, E. R. Henry, M. Ikeida-Saito, K. Kitagishi, T.Yonetani & W. A. Eaton. Proc. Natl Acad. Sci. USA 85, 2151-2155 (1988).

[29] D. A. Duddell. R. J. Morris & J. T. Richards. J. Chem. Soc., Chem. Commun. 2, 75-76 (1979)

[30] J. M. Friedman, & K. B. Lyons. Nature 284, 570-572 (1980).

[31] M. S. Cheung, D. Klimov & D. Thirumalai. Proc. Natl. Acad. Sci. USA 102, 4753-4758 (2005).

[32] Ignatova, Z. et al. Biopolymers 88, 157-163 (2007).

[33] H. Frauenfelder, P. W. Fenimore, G. Chen & B. H. McMahon. Proc. Natl. Acad. Sci. USA 103, 15469-15472 (2006).

[34] J. L. Johnson & E. A. Craig. Cell 90, 201-204 (1997).

[35] F. U. Hartl & M. Hayer-Hartl. Nat. Struct. Mol. Biol. 16, 574-581 (2009).

[36] C. L. Evans & X. S. Xie. Annu. Rev. Anal. Chem. 1, 883-909 (2008).

[37] Z. Ignatova & L. M. Gierasch. Proc. Natl. Acad. Sci. USA 101, 523-528 (2004).

[38] C. Kural et al. Science 308, 1469-1472 (2005).

[39] J. Lippincott-Schwartz,E. Snapp & A. Kenworthy. Nat. Rev. Mol. Cell Biol. 2, 444-456 (2001).

[40] S. Ebbinghaus, A. Dhar, J. D. McDonald & Martin Gruebele Nature Methods 7, 319-323 (2010).

[41] Z. Serber et al. J. Am. Chem. Soc. 123, 2446-2447 (2001).

[42] K. Inomata et al. Nature 458, 106-109 (2009).

[43] R. E. Dickerson and I. Geis. Acta Cryst. B41, 375 (1985). emphHemoglobin.

[44] Garret & Grisham. Saunders College Publishing (2008). *Biochemistry*.

[45] M. M. Rubin, J. P. Changeux. J. Mol. Biol. 21, 265-274 (1966).

[46] W. A. Eaton, E. R. Henry, and J. Hofrichter. Proc. Natl. Acad. Sci. U S A. 88(10), 4472-4475 (1991).

[47] Q. H. Gibson. Biochem. J. 71, 293-303 (1959).

[48] J. Baldwin, C. Chothia. J. Mol. Biol. 129, 175-220 (1979).

[49] B. Vallone, A. Bellelli, A. E. Miele, M. Brunori and G. Fermi. The Journal of Biological Chemistry 271, 12472-12480 (1996).

[50] R. M. Esquerra, R. A. Goldbeck, S. H. Reaney, A. M. Batchelder, Y. X. Wen, J. W. Lewis, & D. S. Kliger. Biophys. J. 78, 3227-3239 (2000).

[51] J. L. Soret. Comptes rendus de l'AcadÃ©mie des sciences 97, 1269-1270 (1883).

[52] J. M. Friedman, T. W. Scott, G. J. Fisanick, S. R. Simon, E. W. Findsen, M. R. Ondrias & V. W. Macdonald. Science 229, 187-190 (1985).

[53] E. W. Findsen, J. M. Friedman, M. R. Ondrias & S. R. Simon. Science 229, 661-665 (1985).

[54] V. Jayaraman, K. R. Rodgers, I. Mukerji & T. G. Spiro. Science 269, 1843-1848 (1995).

[55] S. C. Bjorling, R. A. Goldbeck, S. J. Paquette, S. J. Milder & D. S. Kliger. Biochemistry 35, 8619-8627 (1996).

[56] R. A. Goldbeck, R. M. Esquerra & D. S. Kliger. J. Am. Chem. Soc. 124, 7646-7647 (2002).

[57] G. Balakrishnan, C. H. Tsai, Q. Wu, M. A. Case, A. Pevsner, G. L. McLendon et al. J. Mol. Biol. 340, 857-868 (2004).

[58] S. Fischer, K. W. Olsen, K. Namc and M. Karplus. Proc. Natl. Acad. Sci. USA 108, 5608-5613 (2011).

[59] Jens-Als Nielsen, Des McMorrow. Wiley New York (2001). *Elements of Modern X-ray Physics.*

[60] Jackson, J.D. Wiley New York (1999) *Classical Elettrondynamics, 3rd edition.*

[61] J. Baruchel, J.L. Hodeau, M.S. Lehmann, J.R. Regnard, C. Schlenker. EDP Sciences-Springer-Verlag(1993) *Neutron and synchrotron radiation for condensed matter studies*

[62] Svergun D., Kock M. Rep. Prog. Phys., 80, 1735-1782 (2003). *Small-angle scattering studies of biological macromolecules in solution.*

[63] Hirai M., Iwase H., Hayakawa T., Miurab K., Inoueb K. J. Synchrotron Rad., 9, 202-205 (2002). *Structural hierarchy of several proteins observed by wide-angle solution scattering.*

[64] Grossman A., Abraham Z.H.L., Adman E.T., Neu M., Heady R., Smith B., Hasnain S. Biochemistry, 32, 7360-7366 (1993).

[65] Svergun D.I., Barberato C. and Koch M.H.J. J. Appl. Cryst., 28, 768-773 (1995). *CRYSOL - a Program to Evaluate X-ray Solution Scattering of Biological Macromolecules from Atomic Coordinates*

[66] Langridge R., Marvin D.A., Seeds W.E., Wilson H.R., Hooper C.W., Wilkins M.H.F., Hamilton L.D., J. Mol. Biol. 2, 38-64 (1960).

[67] Lattman E.E., Proteins, 5, 149-155 (1989).

[68] Koch M.H., Vachette P., Svergun D.I. Q. Rev. Biophys. 36, 147-227 (2003). *"Small-angle scattering: a view on the properties, structures and structural changes of biological macromolecules in solution"*

[69] F. Schotte, S. Techert, P. Anfnrud, V. Srajer, K. Moffat, M. Wulff. Edited by Dennis M. Mills. (2002) *"Third generation Hard X-ray Synchrotron Radiation Sources : Source Properties, Optics and Experimental Techniques"*

[70] A. Plech, R. Randler, A. Geis, M. Wulff, J. Synchrotron Rad. 9, 287 (2002).

[71] M. Wulff, A. Plech, L. Eybert, R. Randler, F. Schotte, P.A. Anfinrud, Faraday Discussion 122, 13 (2003).

[72] J. Labiche, O. Mathon, S. Pascarelli, M. A. Newton, G. Guilera Ferre, C. Curfs, G. Vaughan and A. Homs. REVIEW OF SCIENTIFIC INSTRUMENTS 78, 091301 (2007)

[73] http://www.esrf.eu

[74] M. Cammarata, L. Eybert, F. Ewald, W. Reichenbach, M. Wulff, P. Anfinrud, F. Schotte, A. Plech, Q. Kong, M. Lorenc, B. Lindenau, J. Räbiger, and Stephan Polachowski. Review of scientific instruments 80, 015101 (2009).

[75] S. E. Harris, Proc. IEEE, 57, 2096 (1969).

[76] H. Haken, North Holland Physics Publishing USA (1985). *Light. Volume II - Laser light dynamics*

[77] B. E. A. Saleh and M. C. Teich, John Wiley & Sons USA (1991). *Fundamentals of Photonics*

[78] Experimental report SC-2676 ESRF.

[79] M. F. Perutz. Trends Biochem. Sci. 14, 42-44 (1989)

[80] M. F. Perutz, A. J. Wilkinson, M. Paoli, & G. G. Dodson. Annu. Rev. Biophys. Biomol. Struct. 27, 1-34 (1998).

[81] B. A. Springer, S. G. Sligar, J. S. Olson, & G. N. Philips. Chem. Rev. 94, 699-714 (1994).

[82] T. Yonetani, H. Yamamoto, & T. Iizuka. J. Biol. Chem. 249, 2168-2174 (1974).

[83] S. E. V. Philips & B. P. Schoenborn. Nature 292, 81-82 (1981).

[84] J. S. Olson, A. J. Mathews, R. J. Rohlf, B. A. Springer, K. D. Egeberg, S. G. Sligar, J. Tame, J. P. Renaud. & K. Nagai. Nature 365, 265-266 (1988).

[85] N. T. Yu, G. N. La Mar, and H. Mizukami. Biochemistry 29, 2578-2585 (1990).

[86] E. A. Kerr, N. T. Yu, D. E. Bartniki, and H. Mizukami. J. Biol. Chem. 260, 8360-8365 (1985).

[87] C. Travaglini-Allocatelli, F. Cutruzzol, A. Brancaccio, B. Vallone & M. Brunori. FEBS Letters, 352, 63-66 (1994).

[88] W. Zhang, F. Cutruzzol, C. Travaglini-Allocatelli, M. Brunori, & G. La Mar. Biophys. J. 73, 1019-1030 (1997).

[89] M. Brunori, F. Cutruzzol, C. Savino, C. Travaglini- Allocatelli, B. Vallone & Q. H. Gibson. Biophys. J. 76, 1259-1269 (1999).

[90] K. D. Vandegriff & R. M. Winslow. *A theoretical analysis of oxygen transport: a new strategy for the design of hemoglobin-based red cell substitutes.* In *Blood Substitutes: Physiological Basis of Efficacy* (Winslow, R. M., Vandegriff, K. D. & Intaglietta, M., eds, pp. 134-154 (1995)) Birkhauser, Boston, MA.

[91] R. F. Eich, T. Li, D. D. Lemon, D. H. Doherty, S. R. Curry, J. F. Aitken, A. J. Mathews, K. A. Johnson, R. D. Smith, G. J. Phillips & J. S. Olson. Biochemistry, 35, 6976-6983 (1996).

[92] D. H. Doherty, M. P. Doyle, S. R. Curry, R. Vali, T. J. Fattor, J. S. Olson & D. D. Lemon. Nature Biotechnol. 16, 672-676 (1998).

[93] J. R. Squires et al. Science 295, 1002-1005 (2002).

[94] T. J. Reid. Transfusion, 43, 280-287 (2003).

[95] A. E. Miele, S. Santanch , C. Travaglini-Allocatelli B. Vallone, M. Brunori* and A. Bellelli. J. Mol. Biol. 290, 515-524 (1999).

[96] A. E. Miele, F. Draghi, A. Arcovito, A. Bellelli, M. Brunori, C. Travaglini-Allocatelli, and B. Vallone. Biochemistry 40, 14449-14458 (2001).

[97] B. Vallone, P. Vecchini, V. Cavalli and M. Brunori. FEBS Letters, 324, 117-122 (1993).

[98] G. S.Kachalova, A. N. Popov and H. D. Bartunik. Science, 284, 473-476 (1999).

[99] V. Guallar ,A. A. Jarzecki, R. A. Friesner, T.G. Spiro, J. Am. Chem. Soc. 128, 5427-5435 (2006).

[100] G. Balakrishnan, M. A. Case, A. Pevsner, X. Zhao, C. Tengroth, G. L. McLendon and T. G. Spiro. J. Mol. Biol., 340, 843-856 (2004).

[101] E. R. Henry and J. Hofrichter. Methods Enzymol. 210, 129-192 (1992).

[102] E. R. Henry, C. M. Jones, J. Hofrichter, and W. A. Eaton. Biochemistry, 36, 6511-6528 (1997).

[103] C. M. Jones, A. Ansari, E. R. Henry, G. W. Christoph, J. Hofrichter, and W. A. Eaton. Biochemistry, 31, 6692-6702 (1992).

[104] A. E.Miele, F. Draghi, B. Vallone, and A. Boffi Archives of Biochemistry and Biophysics 402, 5964 (2002).

[105] E. R. Henry, S. Bettati, J. Hofrichter, W. A. Eaton. Biophysical Chemistry 98, 149164 (2002).

[106] M. Perrella, L. Benazzi, M. A. Shea, and G. K. Ackers. Biophys. Chem. 35, 97-103 (1990).

[107] R. A. Goldbeck, S. J. Paquette, S. C. Bjorling, and D. S. Kliger. Biochemistry 35, 8628-8639 (1996).

[108] E. Sackmann. R. Lipowsky and E. Sackmann, vol.1, Elsevier (1995). *Biological Membranes Architecture and Function., Handbook of Biological Physics.*

[109] B. B. Hasinoff. Biophysical Chemistry 13, 173-179 (1981).

[110] M. Hoshino, H. Sonoki, H. Suzuki, H. Adachi, Y. Miyazaki and K. Yamanaka. J. Phys. Chem. B 105, 10976-10982 (2001).

[111] Q. H. Gibson F. J. W. Roughton. Proceedings of the Royal Society of London 147, 44-56 (1957).

[112] S. Krueger and R. Nossalt. Biophys. J. 53, 97-105 (1988).

[113] M. F. Perutz. Nature 161, 204-205 (1948).

[114] S. Remita, P. Fontaine, E. Lacaze, Y. Borensztein, H. Sellame, R. Farha, C. Rochas, M. Goldmann. Nuclear Instruments and Methods in Physics Research B 263, 436-440 (2007).

[115] L. J. Parkhurst and Q. H. Gibson. J Biol Chem. 242, 5762-5770 (1967).

[116] G. Schirò and A. Cupane. Biochemistry 46, 11568-11576 (2007).

[117] U. Samuni, C. J. Roche, D. Dantsker and J. M. Friedman. Protein Reviews 9, 133-159 (2008).

[118] H. N. Chapman et al. Nature under revision.

[119] M. M. Seibert et al. Nature in press.

[120] M. Andersson, E. Malmerberg, S. Westenhoff, G. Katona, M. Cammarata, A. B. Wohri, L. C. Johansson, F. Ewald, M. Eklund, M. Wulff, J. Davidsson, & R. Neutze. Structure 17, 1265-1275 (2009).

Acknowledgments

I would like to start my acknowledgments thanking first of all my supervisor, Antonio Cupane, for the opportunity of working on such an interesting and challenging project. His striking enthusiasm for his work is something that I will keep as an example.
Thanks to Michael Wulff that I had the pleasure to know in Grenoble. I greatly acknowledge all his efforts to teach me X-ray physics and for being an excellent supervisor during the time I spent at ESRF working at the ID09 beamline. I am really grateful to him for having shared with me his enormous experience.
A special acknowledgement goes to Matteo Levantino Giorgio Schiró and Marco Cammarata for the time, the discussions, the help, and the friendly way in which they gave their contribution to this work. I should really thank many people from the ESRF, who helped me with their professional competences. Thanks to Laurent Eybert, Ernesto Paiser, Wolfgang Reichenbach.
A sincere thanks to Laurent Guerin not only for his support, in particular during the first beamtimes, and the generosity in spending his time helping me, but especially because I had the pleasure to learn his philosophy of life.
This work is the result also of the fruitful collaboration with prof. Maurizio Brunori, prof. Beatrice Vallone and Chiara Ardiccioni. I want to thank them for the collaboration, their contribution to the experiments and useful discussion of the data.
I wish to thank prof. Marco Cannas for reading this thesis and for his advices.
None of this work could have been realized without the support of my friends: thanks to Lorenzo, Michele S. and Dario for their calls just in time, for sharing with me the opinions about life, PhD and how huge is the difference between good scientists and good people. Thanks to Michele M., Diego, Valeria, Michelle, Carmela and Angelo for one of the best periods of my life and for repeating with me my first sentence in the morning during HERCULES.
Thanks to Sergio for the encouragement and for pushing me to accept the idea that there is not always just one right answer to the questions and some-

times there is not at all. Thanks to Sebastian for the song he wrote to help me in certain situations and to Valentina because probably she is the only one who knows what I'm talking about. I owe a special thanks to my family for being always by my side and supporting me with their love.